UNIVERSIDAD DE GUANAJUATO

CAMPUS IRAPUATO - SALAMANCA
DIVISIÓN DE INGENIERÍAS

PRECISE MANUFACTURING OF TAPERED OPTICAL FIBER STRUCTURES THROUGH PLASMA-BASED TECHNIQUE

TESIS

QUE PARA OBTENER EL GRADO DE:
MAESTRO EN INGENIERÍA ELÉCTRICA

PRESENTA:
LUIS FERNANDO GRANADOS ZAMBRANO

DIRECTORES:

DR. JULIÁN MOISÉS ESTUDILLO AYALA
DR. JOSÉ ALFREDO ÁLVAREZ CHÁVEZ

SALAMANCA, GUANAJUATO   AGOSTO 2024

Salamanca, Gto., a 05 de agosto del 2024.

M. en I. HERIBERTO GUTIÉRREZ MARTIN
COORDINADOR DE ASUNTOS ESCOLARES
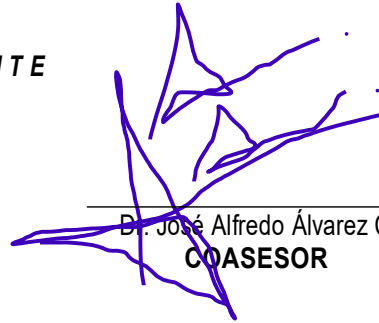**P R E S E N T E.-**

Por medio de la presente, se otorga autorización para proceder a los trámites de impresión, empastado de tesis y titulación al alumno(a) Luis Fernando Granados Zambrano del ***Programa de Maestría en Ingeniería Eléctrica*** y cuyo número de ***NUA*** es: 280509 del cual soy director. El título de la tesis es: Precise Manufacturing of Tapered Optical Fiber Structures Through Plasma-Based Technique

Hago constar que he revisado dicho trabajo y he tenido comunicación con los sinodales asignados para la revisión de la tesis, por lo que no hay impedimento alguno para fijar la fecha de examen de titulación.

A T E N T A M E N T E

_____
Dr. Julián Moisés Estudillo Ayala
DIRECTOR DE TESIS
SECRETARIO

_____
Dr. José Alfredo Álvarez Chávez
COASESOR

_____
Dr. Roberto Rojas Laguna
PRESIDENTE

_____
Dr. Juan Manuel Sierra Hernández
VOCAL

Abstract

The optical fiber structures, known as tapers, have been widely proposed and demonstrated as reliable devices for sensing applications [1], supercontinuum generation [2], and lasers [3]. In this thesis work, the fabrication of these devices is proposed using a high-precision and easy-to-operate electromechanical rig to manufacture tapered optical fiber, specifically using a standard single-mode fiber (SMF). The fabrication technique involves stretching and moving the fiber through plasma, produced by high-voltage discharge (>10 kV) between two tungsten electrodes. To the best of our knowledge, this is the first tapering rig to implement plasma as an effective heating source for soften the fiber.

The fabrication of these structures is evaluated by measuring their dimensions in the taper profile and their spectral transmission response. The system shows a high level of reproducibility, while obtaining non-adiabatic tapers with low insertion losses and mechanically robust. Waist dimensions of up to 6 µm and a total length of up to 15 mm are achieved, maintaining biconical symmetry in their transitions and a constant waist length.

Additionally, a comparison of existing taper fabrication techniques is presented with the main objective of positioning and highlighting the advantages offered by the plasma-based technique. The implementation of one of the fabricated tapers as an intrinsic temperature sensor is presented, showing a sensitivity of up to 100 picometers/degree Celsius (pm/°C) between temperatures of 30 to 140 °C, which allows us to validate the applicability of the proposed electromechanical rig, as well as the potential of these devices to be implemented in optical detection technology.

Finally, the improvements that can be adapted to the tapering rig and plasma production are explained. In this way, the fabrication of tapers using different types of optical fiber can be explored to study their great capacity to be implemented in various applications mentioned before, leveraging all the advantages that optical fiber offers.

Resumen

Las estructuras adelgazadas de fibra óptica, conocidas como tapers, se han propuesto y demostrado ampliamente como dispositivos fiables para aplicaciones de sensado [1], generación de supercontinuo [2] y láseres [3]. En este trabajo de tesis se propone la fabricación de estos dispositivos utilizando un sistema electromecánico de alta precisión y fácil operación para adelgazar la fibra óptica, específicamente la fibra estándar monomodo SMF. El método de fabricación consiste en estirar y trasladar la fibra a través de plasma producido por la descarga de alto voltaje ($>$10 kV) entre dos electrodos de tungsteno. Según nuestro conocimiento, este es el primer sistema que utiliza plasma como fuente efectiva de calentamiento de la fibra.

La fabricación de estas estructuras se evalúa mediante la medición de sus dimensiones en el perfil de taper y su respuesta de transmisión espectral. El sistema presenta un alto nivel de reproducibilidad, obteniendo tapers no adiabáticos, con bajas pérdidas de inserción y mecánicamente robustos. Se consiguen dimensiones de cintura de hasta $\tilde{6}$ μm y una longitud total de hasta 15 mm, manteniendo una simetría bicónica en sus transiciones y un cuello de cintura constante. Además, se presenta una comparación de las técnicas existentes para la fabricación de tapers, con el objetivo principal de posicionar y destacar las ventajas que ofrece la técnica que implementa plasma.

Se presenta la implementación de uno de los tapers fabricados como un sensor de temperatura intrínseco que presenta una sensibilidad de hasta 100 picómetros/grado centígrado (pm/°C) entre temperaturas de 30 a 140 grados, lo cual nos permite validar la eficacia del sistema electromecánico propuesto, además del potencial que tienen estos dispositivos de ser implementados en las diversas aplicaciones mencionadas.

Finalmente, se explican las mejoras que se pueden adaptar al sistema electromecánico así como a la producción de plasma. De esta manera, se puede explorar la fabricación de tapers utilizando distintos tipos de fibra óptica para estudiar su gran capacidad de ser implementados en diversas aplicaciones mencionadas, aprovechando todas las ventajas que presenta el uso de la fibra óptica.

Acknowledgements

I would like to extend my gratitude, in no particular order, to the following organizations and individuals:

* Universidad de Guanajuato and University of Twente

For their unwavering support in creating an enriching academic environment that has been instrumental in my pursuit of this research. The opportunities provided, coupled with access to their extensive on-campus resources and facilities.

* To Yashiro Cisneros, Daniel Jauregui, Juan M. Sierra, and all members of the C.A. de Telecomunicaciones y Fótonica, IEEE-UG Photonics Student Chapter at the Universidad de Guanajuato, as well as Jeroen Korterik, Frans Segerink, and all members of Optical Sciences group and Twente Optics and Photonics Society at the University of Twente

Their exceptional social and academic environment, memorable celebrations, and collaborative teamwork have left an indelible mark on my academic journey. Our shared experiences, including engaging conferences, joyful celebrations, and memorable moments, have made our time together truly exceptional.

* Consejo Nacional de Humanidades, Ciencia y Tecnología (CONAH-CYT), Campus Irapuato - Salamanca and Dirección de Apoyo a la Investigación y al Posgrado (DAIP) at Universidad de Guanajuato

4. **My thesis supervisors:** To Julián Moisés Estudillo Ayala and Roberto Rojas Laguna at Universidad de Guanajuato and José Alfredo Álvarez Chávez and Herman Offerhaus at the University of Twente. For their unwavering guidance, mentorship, and continuous support throughout this research project. Their experience, patience, and encouragement made the successful completion of the thesis possible.

5. My family: To my parents Ma. Guadalupe Zambrano Castillo and Antonio Granados Gonzales and my brothers Cesar Adrián Granados Zambrano and Iván Antonio Granados Zambrano for giving me the emotional support and believing in me.

6. **To my friends:** Jonathan Duarte, Alfredo Medina, Madglenis Beato, Rodrigo Paredes, Oscar Reyes, Alejandro Montenegro, David Guevara, Carlos Osornio, Theodorous Grob, Gredy Hagels, Bjorn Jongebloed, Nadia Chair, and Hessel Van der Vegt. I really appreciate your support and all the great moments we have had together.

* Special mention

To Luis

Best wishes for your studies

David N. Payne

Thesis autographed by Professor Sir David N. Payne, the renowned inventor of the Erbium-Doped Optical Amplifier (EDFA), during my technical visit to the University of Southampton, UK

Thesis structure

The organization of this report is divided into 6 chapters and an appendix to focus on the main idea of each stage of the project development to achieve the proposed objective. The following summary of each chapter facilitates navigation for the reader to locate specific information:

Chapter 1: Introduction

- The history and theoretical analysis of the tapered optical fiber are discussed.

- The main objective is detailed, along with a discussion of the specific objectives, goals, and challenges presented by the project.

- The organization of the report

Chapter 2: Tapered optical fiber

- Fundamental theory about optical fibers

- The Briks model is mentioned to study the reduction of fiber dimensions assuming mass conservation.

- Theoretical analysis of the optical properties of the tapered fiber is provided.

Chapter 3: Taper fabrication techniques

- A review of current heat and pull techniques is provided to compare them with the plasma technique.

- The plasma-based technique, along with its advantages and disadvantages, is explained.

Chapter 4: Optical fiber tapering rig

- The operation of the plasma pulling rig is extensively explained, detailing both the operating principle and its integration as a computer-controlled electromechanical system.

- The principal recommendations for optimal operation of the rig are thoroughly discussed.

- Future improvements and modifications are proposed, highlighting the potential of the rig for manufacturing optical fiber devices such as couplers, long-period gratings, concatenated tapers, and others.

Chapter 5: Characterizing the taper

- The fabricated taper specifications achieved using the plasma technique are described.

- Analysis of the experimental results.

- A statistical study of the fabrication features is conducted to determine the capabilities of the plasma pulling rig.

Chapter 6: Results

- The theoretical analysis and experimental setup of a temperature sensor using a tapered fiber are described.

Chapter 7: Conclusion

- The results are discussed in conjunction with an assessment of the achievement of the objectives.

Appendix A: Building Instructions

- The appendix attached to this report describes the detailed procedure for building the plasma pulling rig and provides all the necessary files for its proper operation.

Contents

Chapter 1

Introduction

Since the 1960s, the study of optical fibers in optical communication and sensing technology has demonstrated remarkable advantages, attributed to properties such as low dispersion over long distances, immunity to electromagnetic noise, and the cost-effectiveness of silica used for its fabrication. Kao and Hockham in the United Kingdom UK proposed cylindrical glass waveguide for light propagation [4], and have been implemented for data transmission in optical communications.

Optical fiber-based devices have been extensively studied for decades, leading to the development of innovations such as optical fiber lasers and optical fiber amplifiers. Notable examples include the erbium-doped fiber amplifier (EDFA) [5] and amplified spontaneous emission (ASE) [6] devices. These amplifiers use rare earth dopants as the active medium in the fiber to enhance light intensity. Furthermore, optical fibers are utilized in optical sensing as Light Detection and Ranging (LiDAR) which is used to estimate the range between two objects [7], biosensing [8] and military security systems [9], where the high sensitivity of silica to external conditions allows for changes in light propagation properties to be measured with nanometer or picometer resolution in real-time parameter monitoring.

Tapered optical fibers capitalize on these properties and further enhance the advantages by offering high sensitivity by increasing the evanescent wave (EW) in the tapered region, small size as micro or nano wires, and resistance to extreme environmental conditions. This reduced section of the fiber can be implemented in optical detection by guiding light through the optical fiber and collecting to measure the transmitted signal, a process known as extrinsic sensing, or by using the tapered fiber directly as a transducer, a process known as intrinsic sensing.[10].

The implementation of these optical devices has become increasingly attractive due to their capacity to enhance even more the EW in the tapered region to measure specific chemical substances by covering a thin metal layer (e.g., gold) and a dielectric medium (e.g., receptor layers) as surface plasmon resonance (SPR)-based sensors[11].

Recently, the fabrication of abrupt shape tapered transition are used as light probes to evaluate characteristics of interest with micrometer-scale spatial precision. This allows for the direct examination of biological samples at the cellular level. Furthermore, the use of tapered tip as optical tweezers represents one of the most novel applications in the field to manipulate the orientation of the trapped particle [12].

In addition, various types of optical fibers such as Photonic-crystal fiber (PCF), fiber Bragg grating (FBG), and multi-core fiber (MCF) are suitable for tapering and exploring novel applications. These devices can be manufactured using several techniques, as reported in this study. The optical classification of these structures determines their potential applications and uses in optical fiber sensors.

1.1   Objective

The design, construction, and implementation of a novel optical fiber tapering rig using the heat and pull method, incorporating plasma as a heater in order to propose the first open-access, cost-effective, and user-friendly plasma pulling rig for manufacturing highly symmetrical taper structures.

1.1.1   Specific objectives

To achieve the main objective of this research, we aim to accomplish the following specific objectives:

1.- Theoretical analysis of the properties of the tapered fiber and modal propagation within these devices

2.- Describe and highlight the advantages of the plasma pulling rig fabricated with the respect of the heat and pull existing techniques

3.- Exploration of the different fabrication parameters using the plasma tapering rig to produce highly symmetrical bi-conical structures

4.- Optical Characterization by evaluating the light transmission spectrum as the optical response of the tapered fiber

Chapter 2

Tapered optical fiber

This chapter approaches the description of the geometrical characteristics and optical properties of tapered optical fibers. The description of single-mode optical fibers and mode propagation is addressed to understand the phenomena that occur when a section of a standard fiber is reduced in dimensions and how its optical properties change within the tapered fiber section. Additionally, it provides an analysis of the theoretical taper profile and adiabaticity criteria employed.

FIGURE 2.1: Illustration of an optical fiber taper

2.1 Electromagnetic waves

The solution of Maxwell's equations allows us to know the characteristics of electromagnetic waves in cylindrical coordinates for the case of an optical fiber. This involves solving complex equations that have been extensively addressed in several textbooks [13]. The detailed procedure of solving Maxwell's equations is not the main focus of this project; however, approximate solutions are discussed to explain mode propagation in a standard optical fiber. For a linear medium the Maxwell's equations are described as:

$$\nabla \times \mathbf{E} = -\frac{\partial \mathbf{B}}{\partial t} \tag{2.1}$$

$$\nabla \times \mathbf{H} = \mathbf{J} + \frac{\partial \mathbf{D}}{\partial t} \tag{2.2}$$

$$\nabla \cdot \mathbf{D} = 0 \tag{2.3}$$

$$\nabla \cdot \mathbf{B} = 0 \tag{2.4}$$

These equations are known as Faraday's Law of Induction (2.1), Ampere's circuital law (2.2), Gauss's law for the electric field (2.3), and Gauss's law for the magnetic field (2.4). Considering a linear medium, they can be expressed in terms of the electric field $\mathbf{E}$ in volts/meter (V/m), magnetic field $\mathbf{H}$ in amperes/meter (A/m), electric flux density $\mathbf{D}$ in Coulombs/meter^2 (C/m^2), and magnetic flux density $\mathbf{B}$ in Webers/meter^2 (Wb/m^2).

In the four equations, ∇ is a vector operator, here the magnetic induction $\mathbf{B}$ is related to the magnetic field strength $\mathbf{H}$ by:

$$\mathbf{B} = \mu \mathbf{H} \tag{2.5}$$

$$\mathbf{D} = \varepsilon \mathbf{E} \tag{2.6}$$

where μ is the permeability of the medium and ε is the electric permittivity. Finally, the volume current density $\mathbf{J}$ is related to the electric field strength through conductivity σ: $\mathbf{J} = \sigma \mathbf{E}$, where the conductivity σ and the free charges are zero.

Substituting for $\mathbf{D}$ and $\mathbf{B}$ by first taking the curl of Equation 2.1, and then substituting Equation 2.2 with $\mathbf{J} = 0$ into the result, to obtain:

$$\nabla \times \nabla \times \mathbf{E} = -\mu \frac{\partial}{\partial t} \nabla \times \mathbf{H} = -\mu\varepsilon \frac{\partial^2 \mathbf{E}}{\partial t^2} \tag{2.7}$$

Then, using the vector identity $\nabla \times \nabla \mathbf{E} = \nabla(\nabla \cdot \mathbf{E}) - \nabla^2 \mathbf{E}$. As mentioned previously, we considered the linear medium, which means that ε and μ do not vary with position. Therefore, because Equations 2.3 and 2.4 imply no free charges and no

free magnetic poles, respectively, by the divergence conditions, Equation 2.14 results in the wave equation for the electric field:

$$\nabla^2 \mathbf{E} - \mu\varepsilon \frac{\partial^2 \mathbf{E}}{\partial t^2} = 0 \tag{2.8}$$

By following the same procedure as before, we obtain the wave equation for the magnetic field, expressed as:

$$\nabla^2 \mathbf{H} - \mu\varepsilon \frac{\partial^2 \mathbf{H}}{\partial t^2} = 0 \tag{2.9}$$

where ∇^2 is the Laplacian operator. For cylindrical polar coordinates, the wave equations given above apply to each component of the field vector. Each component satisfies the scalar wave equation:

$$\nabla^2 \psi = \frac{1}{v_p^2} \frac{\partial^2 \psi}{\partial t^2} \tag{2.10}$$

where ψ represents any components of the $\mathbf{H}$ and $\mathbf{B}$ vectors and v_p is the phase velocity in the dielectric medium. Consequently:

$$v_p = \frac{1}{(\mu\varepsilon)^{\frac{1}{2}}} = \frac{1}{(\mu_r \mu_0 \varepsilon_r \varepsilon_0)^{\frac{1}{2}}} \tag{2.11}$$

Hence, μ_r and ε_r are the relative permeability and permittivity a dielectric medium and μ_0 and ε_0 are the permeability and permittivity of free space. Then, the velocity of light in free space c is given by:

$$c = \frac{1}{(\mu_0 \varepsilon_0)^{\frac{1}{2}}} \tag{2.12}$$

In the case of optical fibers the waveguides are described by cylindrical polar coordinates (r, ϕ, z), then the Laplacian operator is expressed as:

$$\nabla^2 \psi = \frac{\partial^2}{\partial r^2 \psi} + \frac{1}{r} \frac{\partial \psi}{\partial r} + \frac{1}{r^2} \frac{\partial^2 \psi}{\partial \phi^2} + \frac{\partial^2 \psi}{\partial z^2} \tag{2.13}$$

Using Equation 2.13 for the cylindrical homogeneous core waveguide under the weak guidance conditions outlined above, the scalar wave equation can be written in the form:

$$\frac{d^2\psi}{dr^2} + \frac{1}{r} \frac{d\psi}{dr} + \frac{1}{r^2} \frac{d^2\psi}{d\phi^2} + (n_1^2 k^2 - \beta^2)\psi = 0 \tag{2.14}$$

where n_1 is the refractive index of the fiber core, k is the propagation constant for light in vacuum. The propagation constants of the guided modes β. Here, n_2 is the refractive index of the fiber cladding. The solution of the wave equation for the cylindrical fiber as the dominant traverse electric field ψ are separable, having the form:

$$\psi = \mathbf{E}(r) \left[\frac{cos\ 1\phi}{sin\ 1\phi} exp(\omega t - \beta z) \right] \tag{2.15}$$

Substituting the Equation 2.15 in the general wave equation 2.14 results in a differential equation of the form:

$$\frac{d^2\mathbf{E}}{dr^2} + \frac{1}{r} \frac{d\mathbf{E}}{dr} + \left[(n_1 k^2 - \beta^2) - \frac{1^2}{r^2} \right] \mathbf{E} = 0 \tag{2.16}$$

2.2   Single-mode step index fiber

The Standard Single Mode Optical fiber (SMF) consists of a glass wire composed of two concentric silica (silicon dioxide SiO_2) cylinders. The inner cylinder, known as the core, is slightly doped with germanium (Ge) to increase the refractive index, denoted n_1, compared to the surrounding cylinder, called the cladding, with a refractive index n_2. The fiber with this difference in refractive index between the core and the cladding is known as a step index fiber, because the index profile of the fiber is plotted as a step between the core-cladding interface and n_0 corresponds to the refractive index of the air as the cladding-air interface, as depicted in Figure 2.2.
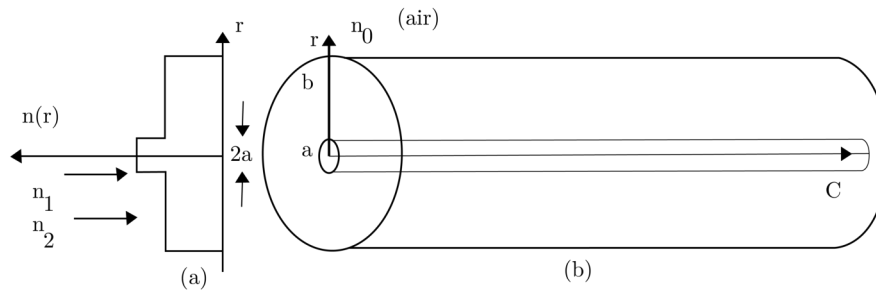
FIGURE 2.2: a) Refractive index profile, and b) Single-mode step index fiber

Therefore, n(r) as function of the radius of the fiber is defined as:

$$n(r) = \begin{cases} n_1 & for \quad r < a, \\ n_2 & for \quad a < r < b, \\ n_0 & for \quad r > b. \end{cases} \tag{2.17}$$

The light is confined to the core of the fiber due to the principle of total internal reflection TIR, where:

$$n_0 < n_2 < n_1 \tag{2.18}$$

2.2.1   Mode propagation in optical fiber

For a step-index fiber with a uniform refractive index core, Equation (2.16) corresponds to a Bessel differential equation, with solutions that are cylindrical functions. In the core region, these solutions are represented by Bessel functions, denoted J_1. In this case, the field remains finite at $r = 0$ and can be expressed using the zero-order Bessel function J_0. In contrast, as r approaches infinity, the field diminishes and the solutions in the cladding are described by modified Bessel functions K_1 [14]. Therefore, the electric field in the core for R<1 is given by:

$$\mathbf{E}(r) = GJ_1(UR) \tag{2.19}$$

where U is the eigenvalue $U = a(n_1^2 k^2 - \beta^2)^{\frac{1}{2}}$. Then for R>1, the electric field in the cladding is:

$$\mathbf{E}(r) = GJ_1(U)\frac{K_i(WR)}{K_i(W)} \tag{2.20}$$

where G corresponds to the amplitude coefficient R=r/a and W the eigenvalue $W = a(\beta^2 - n_2^2 k^2)^{\frac{1}{2}}$

For single mode operation of the fiber, only the fundamental mode LP_{01} exists. This is achieved by selecting an appropriate normalized frequency (V) for the fiber. The generation of additional modes in the SMF depends on the normalized frequency. Therefore, to maintain single mode operation, the cutoff normalized frequency (Vc) must be lower than 2.405.

Thus, the condition for propagation of only the LP_{01} mode is governed by the following relation:

$$0 \leq V < 2.405 \tag{2.21}$$

The normalized frequency is defined by:

$$V = \frac{2\pi a n_1}{\lambda}(2\Delta)^{\frac{1}{2}} \tag{2.22}$$

where: Δ is the relative refractive index difference $n_1^2 - n_2^2$, a is the core radius and λ the operating wavelength.

Figure 2.3 shows the mode intensity profile of the LP_{01} in a single-mode fiber, whereas in a) the intensity mode is concentrated in the center of the fiber core in the transverse section, while in (b), the intensity distribution is represented in a three-dimensional profile, demonstrating the Gaussian distribution of the fundamental mode.
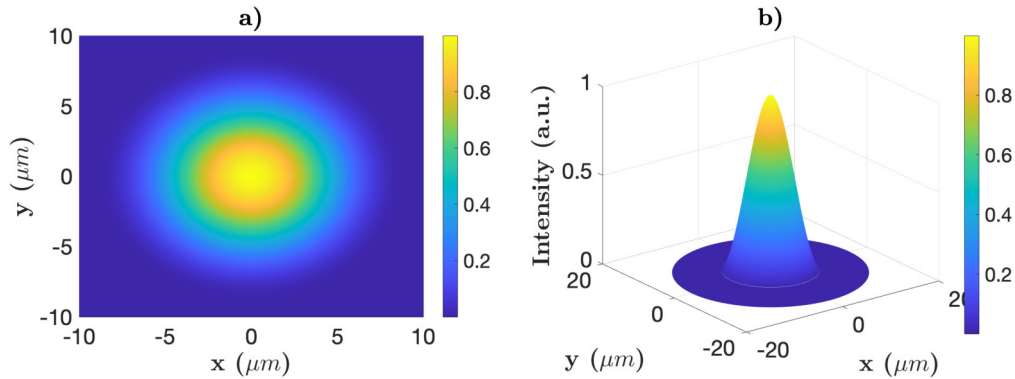

FIGURE 2.3: a) LP_{01} intensity distribution and b)LP_{01} three-dimensional intensity distribution for a step-index SMF with 2a = 8.2 μm, $\lambda = 1550$ nm, $n_1 = 1.4650$, and $n_2 = 1.4573$.[15]

When the value is equal to 2.405, the LP_{11} mode emerges, and the fiber will behave as a multi-mode fiber, supporting multiple modes. Figure 2.4 shows the normalized propagation constant b, as a function of the normalized frequency in terms of the propagation constant of the mode propagation constant β, so that:

$$b = \frac{(\beta/k)^2 - n_2^2}{2n_1^2\Delta} \tag{2.23}$$

Note that the values of b lie between 0 and 1 due to the limits imposed by β limits, where $n_2 k < \beta < n_1 k$ in a SMF, with k representing the propagation constant in a vacuum:

$$k = \frac{2\pi}{\lambda} \tag{2.24}$$

As the relation of β/k is the effective refractive index $n_e ff$, the equation 2.5 can be approximated as:

$$b \approx \frac{n_{eff} - n_2}{n_1 - n_2} \tag{2.25}$$

This approximation is because in a SMF the relative refractive index is very small, leading to a narrow range for β
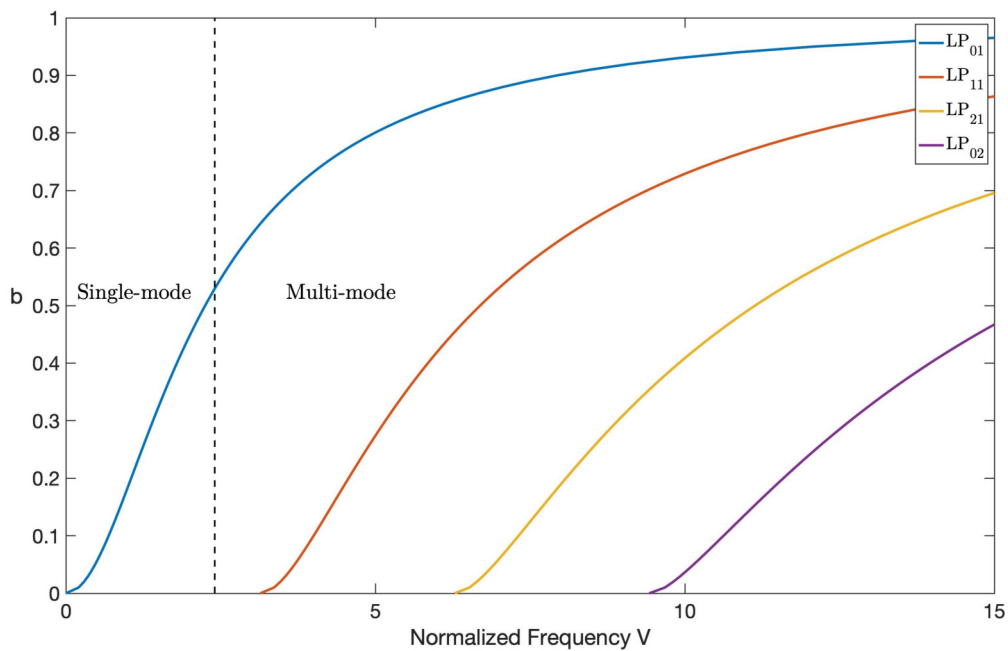
FIGURE 2.4: Normalized propagation constant b as function of the normalized frequency V, for step-index core profiles.

The mode intensity distribution in a transverse view of the optical fiber for the four lowest-order LP_{lm} modes is shown in Figure 2.5.
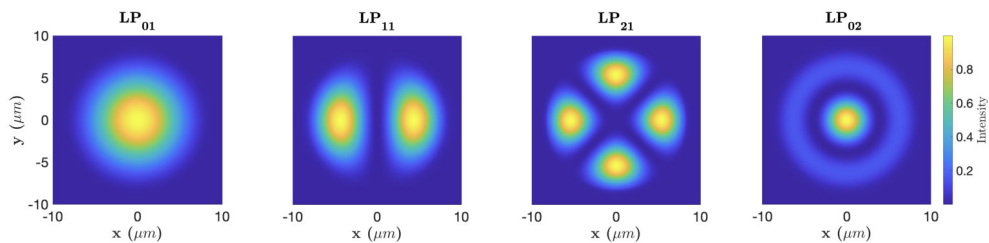
FIGURE 2.5: Mode intensity distribution for the four lowest ordered LP_{lm}, for a step-index SMF with 2a = 8.2 μm, λ = 1550 nm, n$_1$ = 1.4650, and n$_2$ = 1.4573. The figures were plotted using open-source MATLAB code. [15]

Furthermore, single mode operation can be determined by selecting a certain operating wavelength as the cut-off wavelength λ_c given by:

$$\lambda_c = \frac{2\pi a n_1}{V_c}(2\Delta)^{\frac{1}{2}} \tag{2.26}$$

Dividing Eq 2.26 by Eq 2.22, we obtain the inverse relationship:

$$\frac{\lambda_c}{\lambda} = \frac{V}{V_c} \tag{2.27}$$

Thus for step index fiber where $V_c = 2.405$, The cutoff wavelength is given by:

$$\lambda_c = \frac{V\lambda}{2.405} \tag{2.28}$$

Here, the fiber will transmit light in a single mode only for $\lambda > \lambda_c$

The solutions of the electromagnetic wave equations in standard optical fibers, typically demonstrates a very small relative index difference, where $\Delta << 1$. These fibers satisfy the weakly guiding approximation, where the approximate solutions for modes include hybrid modes (HE, EH) and transverse modes (TE, TM), which can be represented by two linearly polarized (LP_{lm}) modes [16], where the integers, l=0,1,2,... and m =1,2,3... , specify the electric field intensity profile bounded in two dimensions. It is important to note that these modes are not exact modes of the fiber except for the fundamental mode. However, the weakly guiding principle allows to relate the traditional modes to the LP modes, (see Table no 2.1). The subscripts l and m are related to the intensity profile of the electric field for a particular LP mode. Moreover, results convenient for this research describe the LP modes in the standard fiber utilized, where the polarization states are well-defined.

Linearly polarized mode	Exact mode
LP_{01}	HE_{11}
LP_{11}	HE_{21}, TE_{01}, TM_{01}
LP_{21}	HE_{31}, EH_{11}
LP_{02}	HE_{12}
LP_{lm}	HE_{2m}, TE_{0m}, TM_{0m}
LP_{lm}(l$\neq$ 0 or 1)	$HE_{l+1.m}$, $EH_{l-1.m}$

TABLE 2.1: Linearly polarized modes with their corresponding exact mode equivalence

2.3   Tapering the fiber

A tapered optical fiber is a fiber with reduced dimensions along a specified length of a SMF by stretching a heated fiber. This reduction is characterized by a geometric interface divided into three sections (see figure 2.4):

1. The untapered fiber: This refers to the SMF without any deformation.

2. The tapered transitions: The segment where the fiber decreases from the standard size of SMF to the waist is referred to as the 'down transition', while the 'up transition' is the segment where the fiber dimensions increase from the waist to the SMF.

3. The waist: This section represents the smallest diameter, which remains constant along the taper region.
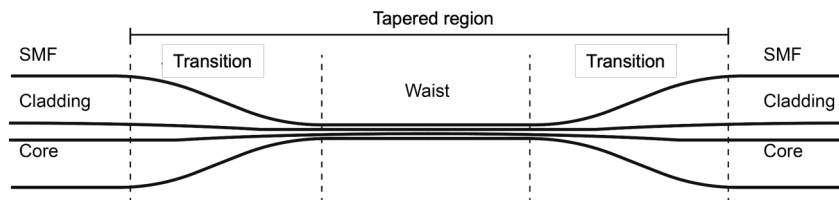
FIGURE 2.6: Tapered optical fiber scheme

The most commonly employed technique for fabricating a taper involves pulling a heated fiber using two translation stages to stretch the fiber, while a section of it is softened by a heater, allowing controlled reduction of its dimensions. Figure 2.6 illustrates this method. Assuming uniform heating of the fiber and that the geometry of the heated fiber remains cylindrical, the mathematical model for this reduction can be described by the model developed by Birks et al. in 1992,[17].
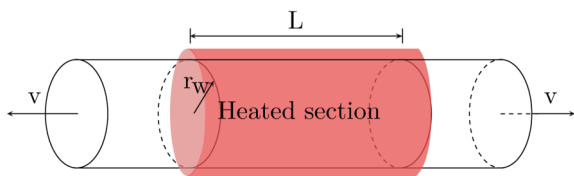
2.3.1   The model

FIGURE 2.7:   Uniform heating of the fiber

This model enables the prediction of the diameter profile of a taper based on two crucial parameters of the heating and pulling technique: the pulling velocities v and the length of the hot-zone L. Figure 2.6 illustrates the model, where, by uniform heating the fiber and achieving uniform viscosity, the taper reduction will consistently maintain a cylindrical shape.

Hence, when a constant velocity v is applied at the edges to pull the fiber, the tapering process begins at an initial time t, and continues until a remaining time $t + \delta t$, where δt represents the duration during which the stages exert the pulling

force. Consequently, the original length L is elongated to $L + \delta x$, where δx represents the tapered length. As a result, the untapered radius r_w decreases to $r_w + \delta r_w$, indicating the tapered radius. Besides, the length of the hot-zone also changes to $L + \delta L$. (see Figure 2.7.)

The final waist is equal to the final hot-zone length by the process time stops and the conditions satisfies:
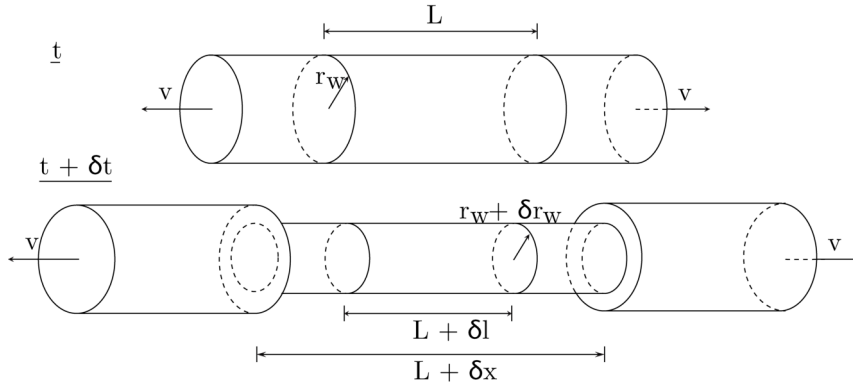
$$L \geq 0 \tag{2.29}$$

$$\frac{dL}{dx} \leq 1 \tag{2.30}$$

FIGURE 2.8: Tapering the fiber by conservation of volume

Thus, the volume of the glass cylinder at time $t + \delta t$ is expressed by:

$$\pi r_w^2 L = (r_w + \delta r_w)^2 (L + \delta x) \tag{2.31}$$

where δr_w is radius variation expressed negative value. Regarding the equation we obtain:

$$\left(\frac{r_w}{r_w + \delta r_w} \right)^2 = \frac{(L + \delta x)}{L} \tag{2.32}$$

For small variations $(\delta r_w \ll r_w)$, we can approximate to:

$$\left(\frac{r_w}{r_w + \delta r_w} \right)^2 = \left(\frac{1}{1 + \delta r_w / r_w} \right) \approx 1 - 2\frac{\delta r_w}{r_w} \tag{2.33}$$

Thus, rewriting the Equation 2.11,

$$1 - 2\frac{\delta r_w}{r_w} = \frac{(L + \delta x)}{L} \tag{2.34}$$

Evaluating the limit when $\delta t \to \infty$, in the equation 2.13, we obtain:

$$\frac{dr_w}{dx} = -\frac{r_w}{2L} \tag{2.35}$$

As mentioned, the length of the heating section depends on the tapering process. Therefore, we denote it as $L = L(t)$. Besides, note that x increases as a function

of time, when the fiber is being pulled by the stages obtaining L as a fiction of x, expressed by: $L + L(x)$.

Integrating both sides of equation 2.14, we have:

$$\int_{r0}^{r} \frac{dr_w'}{r_w'} = -\frac{1}{2} \int_0^x \frac{dx'}{L(x')} \tag{2.36}$$

Note that the limits r_0 refers to the radius of the untapped fiber (initial radius), and r is the taper radius, and the limits of the second integral refers to the elongations along the length L. Finally, the expression relating the radius of the waist r_w, with the total pulling length x, is:

$$r_w(x) = r_0 \; exp\left(-\frac{1}{2} \int_0^x \frac{dx'}{L(x')}\right) \tag{2.37}$$

Considering L as a constant during the tapering process, the solution for the fiber waist radius is given by:

$$r_w(x) = r_0 \; exp\left(-\frac{x}{2L_0}\right) \tag{2.38}$$

For the initial radius, we denote $r_0 = r_w(0)$. Then, for a distance z along the tapered section $r(z)$, at a given point z, relative to r_w and L (see Figure 2.7). With these boundary conditions, we can calculate the radius $r(z)$ of the taper section. If $r(z) = r_w(x)$, then:

$$r(z) = \begin{cases} r_0 & for \quad z < z_P, \\ r_0 e^{-(z-z_P)/L_0} & for \quad z_P < z < z_P', \\ r_0 e^{-x/(2L_0)} & for \quad z_P' < z < z_Q', \\ r_0 e^{(z-z_Q)/L_0} & for \quad z_Q' < z < z_Q, \\ r_0 & for \quad z > z_Q. \end{cases} \tag{2.39}$$

The radius evolution along the fiber by Equation 2.18, is expressed:

$$L(x) + 2z_0 - x + L_0 \tag{2.40}$$

It is important to note that this expression is valid as long as $L \geq 0$.

This analysis is based on the constant heating of the fiber, where $L(x) = L_0$. Therefore, the single pulling state is given by $z_0 = x/2$, which represents the pulling length. Besides, the waist length equals the final heating zone after the tapering process.Figure 2.8 A), plots the result of the dependence of the waist radius with the pulling length ´x', and B) plots the equation 2.18, where the radius of the tapered region depends on the constant heating section L_0
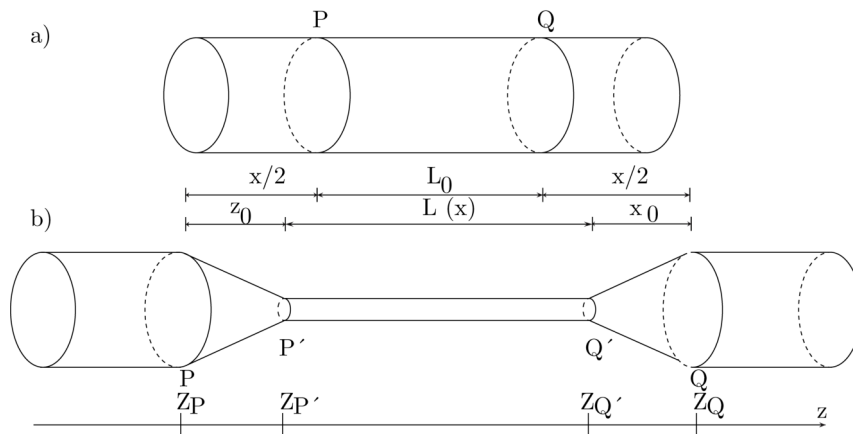
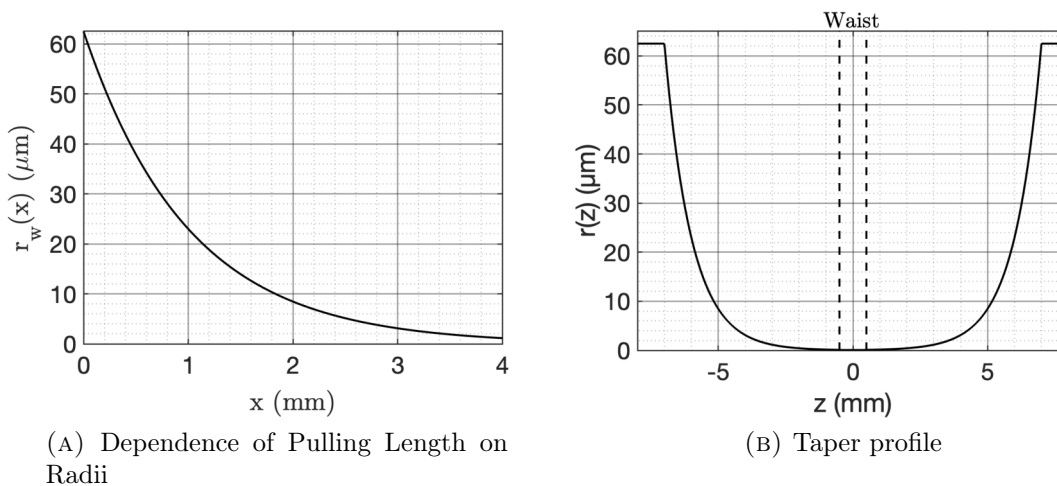FIGURE 2.9: Tapering the fiber by conservation of volume

(A) Dependence of Pulling Length on Radii

(B) Taper profile

FIGURE 2.10: The result of plotting the Briks model for $r_0 = 62.5\mu m$ for a SMF, with $L_0 = 1$ and z= 14 mm

Summary

The Birks Model provides a useful tool for this project, as it allows for the theoretical prediction of the shape and dimensions of the tapered fiber. However, in practice, especially when using plasma as a heater, the model may not be directly applicable. This is because the pulling forces may not be uniform, and the heating section may not be constant and uniform due to the translation of the fiber within the heater. Despite these limitations, we have considered this model for comparison with ideal conditions, providing us with a valuable overview of the expected theoretical results compared to experimental outcomes.

2.4   Adiabaticity criteria

A taper is considered adiabatic if the tapered transition angle is small enough every-where to ensure minimal power losses from the fundamental mode as it propagates along the length of the taper. Within an adiabatic taper of a single-mode fiber, the fields and propagation constant can be accurately described by those of the local fundamental mode, which conserves power during propagation (Love et al., 1991, [18]). Conversely, a taper is deemed non-adiabatic if the slope angle of the tapered transitions is abrupt enough to excite higher-order modes, ensuring that coupling occurs primarily between the fundamental mode of the untapered fiber and the first two modes of the taper waveguide [19]), resulting in mode propagation losses.

In cylindrical geometry, the modal electric field $\boldsymbol{E}$(x,y,z), where z represents the distance along the tapered fiber and x,y are the transverse coordinates, as illus-trated in Figure 1.3 (A).

$$\boldsymbol{E}(x, y, z) = a(z)\hat{e}(x, y, \beta(z))exp\left\{i \int_0^z \beta(z')dz'\right\} \tag{2.41}$$

where $a(z)$ is the modal amplitude, $\beta(z)$ is the propagation constant at position z, and $\hat{e}$ refers to the transverse dependence.
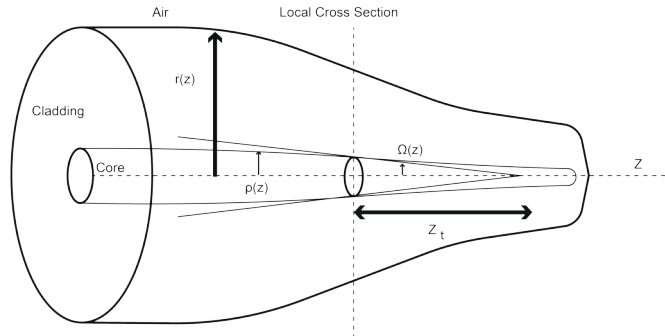
FIGURE 2.11: Tapered fiber transition cladding-air interface

The integral within the exponent represents the accumulated phase change along the tapered fiber, and the apostrophe denotes that the fields are orthonormal. This orthonormality ensures that, in the absence of coupling, the power is conserved as the mode propagates, i.e. $a(z)$ is constant. Figure 1.4 (B) illustrates the evaluation of z along the tapered fiber to evaluate the taper angle at every point across the tapered transition length.

Assuming that the taper is axisymmetric, as in the case of a single fiber taper, the fundamental local mode LP_{01} can only excite modes with the same azimuthal symmetry, i.e., the higher order LP_{0m} cladding local modes, with the highest cou-pling to the nearest mode LP_{02}. For non-axisymmetric fiber tapers, such as a bent taper, coupling will occur to the mode with the nearest propagation constant to the fundamental mode, i.e., the modes with $l>1$ as the LP_{11} mode (see Figure 2.4).

2.4.1 Length-scale criterion

The length-scale criterion establishes that the local taper length-scale must be much larger than the coupling length between the fundamental mode and the dominant coupling mode to minimize power losses. As illustrated in Figure 1.3 (A), the length-scale z_t, determines the height of a right circular cone with a base coincident with the local cross-section and an apex angle equal to the local taper angle $\Omega(z)$ =arctan $|d\rho/dz|$, where z is the distance along the tapered fiber, and $\rho = \rho(z)$ represents the local core radius. For adiabatic tapers: $\Omega(z) << 1$, then

$$z_t = \rho/\Omega \tag{2.42}$$

The local coupling length $z_b = z_b(z)$, where the beat length length of the excited higher modes interferes with the fundamental mode, is defined by:

$$z_b = \frac{2\pi}{\beta_1(z) - \beta_2(z)} \tag{2.43}$$

Here $\beta_1(z)$ is the propagation constant of the fundamental mode and $\beta_2(z)$ the propagation constant for the second local mode. The tapered transitions are called adiabatic if $z_t >> z_b$, with negligible power loss from the fundamental mode. For, $z_t << z_b$, the higher modes are excited and consequently the power will leak out from the fundamental mode to higher order modes. Finally, if $z_b = z_t$, determines the distinction between adiabatic taper and lossy taper, by equating Eq(1.09) and Eq(1.10), we obtain:

$$\Omega = \frac{\rho(\beta_1 - \beta_2)}{2\pi} \tag{2.44}$$

Thus $\Omega(z)$ is defined as a function of the local core radius. For a taper with a local taper angle at any point of z, $\Omega(z) > \Omega$, then taper is non-adiabatic and the excitation and coupling modes will occur.

The Figure 2.10, the $\Omega(z)$ is plotted a function of the normalized core radius $\rho(z)/\rho_0$.

The taper section with angle $\Omega(z)$ smaller than the solid line signifies that this taper and the taper angle corresponds to an exponential taper.

Additionally, the inequality expression of the Equation 2.21 and 2.22, the tapered fiber can be expressed to:

$$\left|\frac{dr}{dz}\right| = tan\ \Omega < \frac{\rho(\beta_1 - \beta_2)}{2\pi} \tag{2.45}$$

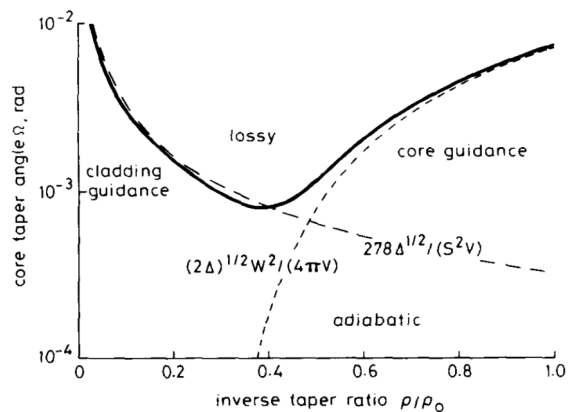Then, for the expression bellow it can be rewritten as a function of local cladding

FIGURE 2.12: Adiabaticity for the LP$_{01}$ mode, for n_{cl} = 1.4505, n_{co} =1.4537 and $\lambda = 1.3\mu m$. The Figure is taken from (Love et al., 1991, [18])

radius r=r(z) as [20]:

$$\left|\frac{dr}{dz}\right| = < \frac{r(\beta_1 - \beta_2)}{2\pi} \qquad (2.46)$$

Therefore, another approximate criterion to classify a taper as adiabatic or lossy by the tapering angles:

$$\Omega = \frac{\rho(\beta_1 - \beta_2)}{2\pi}F \qquad (2.47)$$

Where F refers to the adiabaticity adimensional factor, between 0 and 1. Where for values where $F \approx 0.5$ the transmission of the taper will be higher than 95 %, considering an adiabatic taper, the optimal profile is achieved when f=1. [21]

2.5 Experimental evaluation of the adiabaticity criterion

The determination of whether a taper is adiabatic or non-adiabatic can also be estimated through experimental measurements. In addition to evaluating the theoretical criterion, we experimentally assessed the conditions that enable us to determine the adiabaticity of the tapers manufactured and characterized in this report. Furthermore, we referred as a highly non-adiabatic tapers, as those exhibiting abrupt transitions, considerable losses, and modal interference that can be analyzed trough the Fast Fourier Transform FFT, which allows us to observe the spatial frequencies present in the interference pattern, corresponding to different optical paths in the taper.

2.5.1 Transmittance

An experimental test to evaluate light transmission losses on a taper involves transmittance measurement, where an optical source and a power meter were used, as illustrated in Figure 2.12. Then, for the the measurements of loses the following
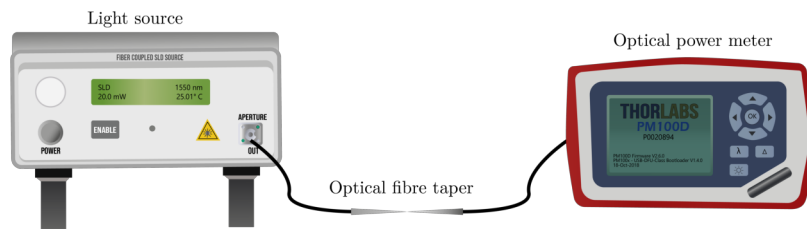
FIGURE 2.13: Taper light transmission scheme

equation is employed [22]:

$$\alpha = 10 \; log_{10}\frac{P_1}{P_2} \qquad (2.48)$$

Where α represents the losses in decibels (dB), P_1 denotes the input power and P_2 the output power, both expressed in Watts (W).

To measure the transmittance of a taper, a light source is connected to the tapered fiber as an input, and the power is measured on the other side of the taper as the output of the system to measure the light transmission losses. The input power reference (P_1) is the power supplied by the light source to the SMF fiber before the taper, and the output power is measured after the taper using an optical power meter (see Figure 2.12).

Tapers that transmit 99% of power typically exhibit negligible losses, ideally to be used in fiber-to-chip couplers [23] [24], fiber couplers, and WDM, while those above 95% of transmittance generally have very low losses. Conversely, tapers retaining 95% or less may incur considerable to high losses, indicating that they are likely to be lossy and non-adiabatic tapers. This non-adiabatic taper is ideal for the sensing application attaching high sensitivity, and the tapered section is typically used as the sensor without the utilization of other inteferometers in the same fiber setup. [25] and lasers [26].

2.5.2 Light spectrum

The visualization of the transmitted spectrum of a taper using a broadband light source at the input and an Optical Spectrum Analyzer OSA at the output of the taper, allows us to visualize the spectrum at different wavelengths of an SMF as the reference signal, and with the tapered fiber as the spectrum transmitted. In the case of an adiabatic taper, the spectrum should closely resemble the reference spectrum, with minimal insertion losses attributed to the taper and the fiber system components (e.g., connectors, splices). Conversely, for non-adiabatic tapers, the spectrum will display interference patterns due to multimodal interference. By comparing this spectrum with that of the source, we can observe a lossy spectrum that depends on the shape of the taper relative to the reference.
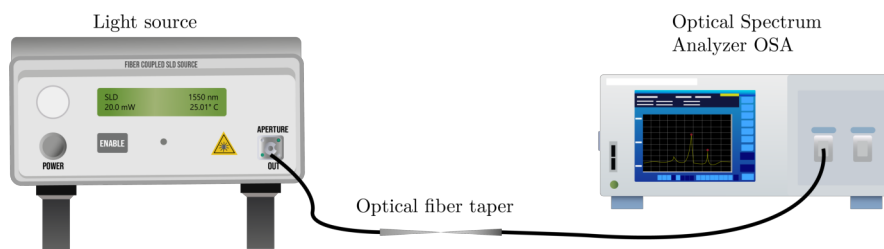

FIGURE 2.14: Scheme to visualize the spectrum transmitted through a tapered fiber

2.6   Mode propagation in tapered fiber

The propagation of modes in a tapered optical fiber cannot be accurately approximated by linearly polarized (LP) modes due to the significant difference in refractive index (n) between the core and cladding, as the light is primarily guided by the cladding-air interface. Therefore, exact modes are required to estimate mode propagation theory in the taper. However, for comparison purposes, it is convenient to compare the LP modes with their respective equivalent exact modes depicted in Table 2.1. This allows for a comparison of mode propagation between standard SMF and tapered SMF.

The tapered fiber satisfies the condition where the core mode is $n_{cl} < n_{eff} < n_{co}$. The fiber parameters and modal parameters are defined by:

$$u_1 = k(n_{co}^2 - n_{eff}^2)^{\frac{1}{2}} \tag{2.49}$$

$$w = k(n_{eff}^2 - n_{cl}^2)^{\frac{1}{2}} \tag{2.50}$$

Then, by taking the wave equation (2.24) in a single-mode fiber (SMF), we have the solution as follows:

$$\psi = \begin{cases} A j_v(u_1 r) e^{iv\phi} & for \quad 0 \leq r \leq \rho; \\ C K_v(wr) e^{iv\phi} & for \quad \rho \leq r \leq \rho_{cl}. \end{cases} \tag{2.51}$$

Here, A and C are constants, ρ and ρ_{cl} are the radii of the core and the cladding, respectively. J_v and K_v are the vth-order Bessel function of the first kind and the modified Bessel function of the second kind, respectively. For modes LP_{0m} and $LP1m$ modes, v=0 and v=1, respectively. Continuity of the electromagnetic field ψ and its first derivative $\frac{d\psi}{dr}$ at the core boundary $r = \rho$ relate the values of AA and CC and leads to a set of eigenvalue equations. This provides the following mode condition [27]:

$$v_1 \frac{J_{v+1}(u_1 \rho)}{J_v(u_1 \rho)} = w \frac{K_{v+1}(w\rho)}{K_v(w\rho)} \tag{2.52}$$

The eigenvalues obtained from the Eq. 2.48 are labeled as β_{vm} with $v = 0, 1, 2, ..., m = 1, 2, 3, ...$, where the subscript m indicates the mth root of Eq. 2.48 of the corresponding modes LP_{vm}

2.7 The evanescent field in tapered fiber

The principle of total internal reflection RI in single-mode optical fibers SMF ensures that all the power associated with the fundamental mode propagates within the core. In this process, the electric field is approximated by a Gaussian distribution and is concentrated within the core (see Figure 2.13(a). However, a small portion of the energy is coupled into the cladding modes, where the electric field decays exponentially in the direction of an outward normal to the core-cladding interface. This phenomenon is known as the evanescent field. [28]

(A) Electric field propagation of the fundamental mode in a SMF

(B) Field amplitude distribution $E(r)$ of the fundamental mode in and MDF in a SMF
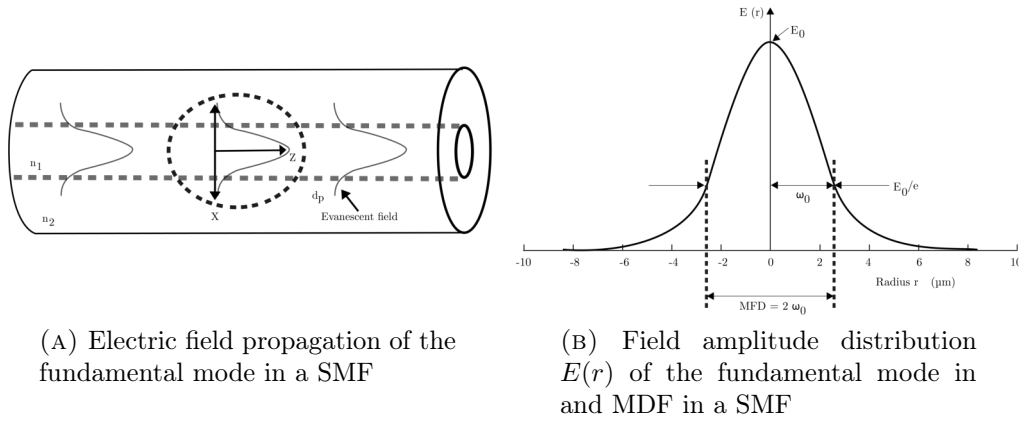
FIGURE 2.15: Evanescent field phenomenon in an optical fiber

The Mode Field Diameter, $MFD = 2\omega_0$, where ω_0 is the nominal half width of the input excitation. Hence, MFD is defined as the distance between the opposite $1/e = 0.37$ field amplitude points and the power $1/e^2 = 0.135$ points with respect to the fiber axis, as clearly shown in Figure 2.13(b).

The electric field amplitude, E at a distance x along the normal is given by:

$$E = E_0^{-x/d_p} \tag{2.53}$$

where E_0 corresponds to the Electric field and d_p is the penetration depth between the core and cladding interface. The magnitude of the penetration depth is given by:

$$d_p = \frac{\lambda}{2\pi n_1 \sqrt{sin^2\theta - (n_2/n_1)^2}} \tag{2.54}$$

where λ is the wavelength in the vacuum, θ is the angle of incidence relative to the normal of the interface, n_1 and n_2, are the refractive indices of the core and cladding, respectively.

The tapering fiber has the potential to increase d_p as a function of the NA, the RI of the cladding, the surrounding refractive index SRI , the taper ratio $TR = r_w/r_0$, the taper length L, and the taper position z. The evanescent field emerges differently along the tapered region, and the fraction of power propagating in it (η_{EF}) depends on the ratio of λ/r. Hence, a tapered fiber with a smaller radius would produce
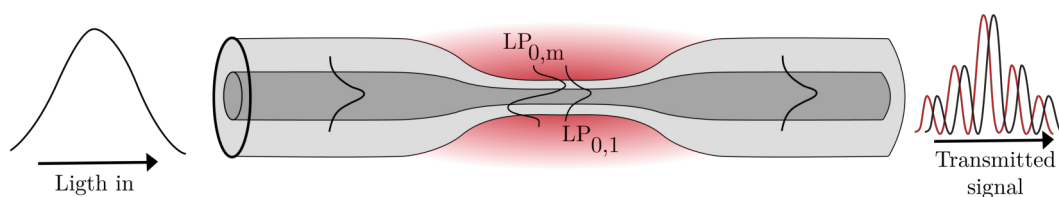
FIGURE 2.16: Evanescent field phenomenon in tapered fiber

a larger fractional power of the evanescent field [29]. The largest evanescent field occurs at the waist, making this region the most sensitive. (see Figure 2.14)

In the case of a non-adiabatic fiber taper, coupling primarily occurs between the fundamental mode of the untapered fiber and the first two modes of the taper waveguide (LP_{01}, LP_{02}), where due to the difference in refractive indices between the air and the cladding, the taper typically supports more than one mode, the taper region thus becomes a multimode waveguide. As a result of the back-and-forth coupling between the single mode of the fiber and the two (or more) modes, the taper presents multimodal interference. The efficiency of this coupling depends on the relative phase of the participating modes. Consequently, this region behaves like a Mach-Zehnder interferometer. If there are only two modes, the relative phase difference is given by $\Delta\Phi = \Delta\beta L$, where $\Delta\beta$ is the difference in the propagation constants of the two modes and L is the length of the interaction along the taper [30].

Chapter 3

Taper fabrication techniques

This chapter presents a study of the plasma generated by an electric field and provides a detailed description of the plasma-based technique that we employed. Additionally, a literature review of heat-and-pull techniques is presented to compare and position our proposed technique as an alternative to existing technologies used in the fabrication of tapered optical fibers. This assessment considers critical factors, including taper dimensions, evaluation of the light power transmission, and the fabrication time.
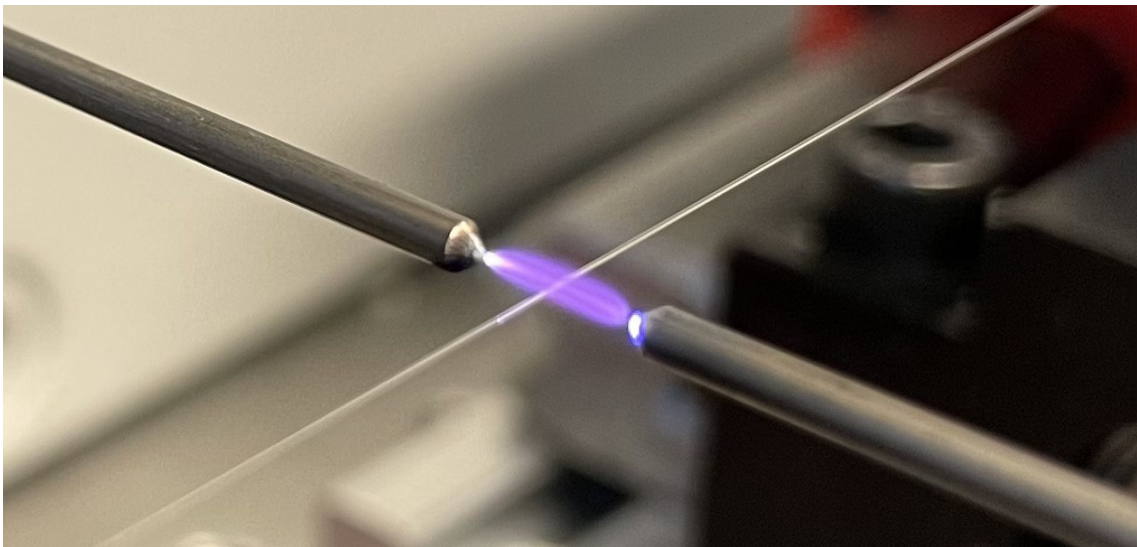
FIGURE 3.1: Plasma heating the optical fiber

3.1   Plasma overview

The heat source employed to soften the silica is plasma, generated through the application of a strong electric field between a pair of tungsten electrodes. This electric field ionizes the gas between the electrodes, in this case air, by inducing a significant number of charge carriers in the air that is naturally an excellent insulator at room temperature, under these conditions, it undergoes a transition to a state where it can conduct electrical current, resulting in the production of extremely high temperatures due the high speed movement of electrons and ions.

This process is known as electrical breakdown, and it is one of the most common processes to ionize the air for plasma production. The plasma often called the fourth state of matter, distinct from the three states of matter, solid, liquid, and gas. Unlike the transitions from solid to liquid and liquid to gas that occur with elevated temperatures, plasma represents a unique state. In this state, the molecules of the gas are decomposed into atoms and, subsequently these atoms are decomposed into electrons and positively charged ions.

Figure 3.1 represents the circuit that we utilized to produce the plasma, a potential difference is applied by an AC source, and the electrons are accelerated by the electric field in front of the cathode and collide with the gas atoms. The significant collisions are the inelastic collisions leading to excitation and ionization of the gas. The application of high voltage triggers, and the ions produced by the ionization process can be detected with a mass spectrometer. When subjected to high voltage, excited atoms or ions emit characteristic photons, producing elevated temperatures.
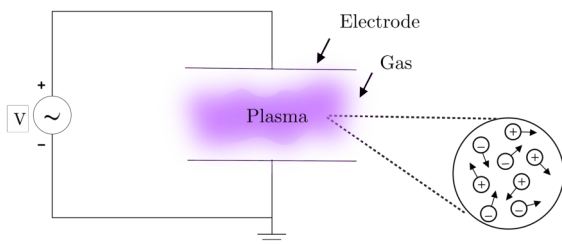
FIGURE 3.2:   Plasma generation circuit

The plasma temperature can be estimated by different techniques, as optical emission spectrometry [31]. Nevertheless, it is difficult to measure the temperature explicitly, and the theoretical or analytical procedures can only estimate the temperature range of the plasma. The relation of the electron speed through the pressurization of the ionization process can estimate the temperature of the ionized gas.

To measure the frequency of discharges between the electrodes to produce the electrical breakdown, it is necessary to know the composition of the gas, the distance between the electrodes, the frequency of the applied field, and the geometry of the electrodes. For air, the breakdown voltage in the High Voltage circuit ranges from 10 kV to 20 kV.

One common method to estimate the frequency of electric discharge is to consider

the breakdown voltage of the medium between the electrodes. For air, this breakdown voltage typically ranges from 3 kV/mm to 30 kV/mm, depending on factors such as pressure, humidity and electrode geometry.

Figure 2.5 illustrates the process of an elementary glow discharge. Upon application of a potential difference between the electrodes, the argon gas (used here for explanatory purposes) undergoes breakdown, generating electrons and positive ions. The emitted electrons initiate collisions within the plasma, leading to the excitation of electrons to higher energy levels. Subsequently, radiation is emitted as these electrons return to their initial levels.

3.1.1 Plasma condition

The formation of plasma occurs when the average kinetic energy, denoted by the electron temperature T_e ,(where the temperature is considered as an energy unit with the Boltzmann constant as unity), exceeds the average Coulomb energy required for an ion to capture an electron. Here, d represents the average separation between the nearest electron and ion, e is the elementary charge, and ε_0 is the permittivity of vacuum.

FIGURE 3.3: Schematic overview of the basic plasma process in a glow discharge, Source: [32]

Assuming that the ions are singly ionized and n_0 is the average number of electrons or ions per unit volume, the estimation of d is achievable through the relationship $e^2/4\pi\varepsilon_0 d$. The condition for plasma formation can then be expressed as [32]:

$$\left(\frac{4\pi}{3}n_0\right)^{1/3}\frac{e^2}{4\pi\varepsilon_0 T_e} \ll 1 \tag{3.1}$$

3.1.2   Plasma technique

The heat-and-pull plasma-based technique is depicted in Figure 3.4. The process begins by transporting the fiber to the right, with significantly faster movement of the right translation stage to achieve a pulling effect while simultaneously transporting the fiber through the plasma. This approach was adopted because of the limited hot zone of the plasma, approximately 0.5 mm, and the impracticality of brushing this heater due to the perturbations caused by movement, which affect stable plasma production. Furthermore, since the plasma exceeds the minimum threshold required to fuse the silica (>1,200 degrees), pre-heating the fiber before pulling is unnecessary, as it softens immediately upon contact with the plasma.

The distance L is determined as the total length of the tapered fiber, equating to the distance the fiber is transported through the plasma between the electrodes. The velocity and travel distance are primarily determined by the faster translation stage, dictating the length L, and the speed at which the fiber passes through the plasma. Besides, before the pulling process, the plasma is off where the fiber is positioned at initial L=0, and with a velocity of $v = 0$.

These two parameters according to the Briks model described in chapter 2, these two parameters will determine the radius along the tapered fiber. This model can only estimate the dimensions of the tapered fiber working under ideal conditions as a constant heat section and mass conservation.

Nevertheless, through experimental testing using the plasma-based technique,

FIGURE 3.4: Fiber pulling rig

the velocity v, and the taper length L, determines the radius of the waist. If the fiber moves too slowly towards the plasma, the fiber risks burning. Conversely, if the fiber is transported at high speed, the dimensions of the taper will successfully reduced.

Thus, plasma is considered an effective heater that softens the fiber. As a result, the radius of the taper can reach approximately $8\mu m$ in diameter over the taper length.

The use of plasma for heating the fiber allows manufacturing highly symmetric non-

adiabatic tapers, with abrupt tapered transitions, Moreover, based on the literature reviewed for this research, this is the first optical fiber tapering rig that employs plasma. The aim of this technique is to offer additional options for implementing a heater capable of producing abrupt transitions, high symmetric non-adiabatic tapers, and affordable elements to construct a cost effective rig.

3.2   Fabrication techniques

The selection of a heating source for softening the optical fiber is a crucial factor in the manufacturing of tapered fibers The principal heat-pulling techniques reported for tapering optical fibers are: Flame Brushing [33] [34][20], CO_2 Laser [35][36] [37], Ceramic Microheater [38][39], Electric Arc Discharge [39][40] and Plasma [**This work**]. Each technique has its own advantages and limitations, and the choice of technique depends on factors such as the required taper dimensions, adiabaticity, as determined by the specific application.

3.2.1   Flame brushing technique

The rigs that use a gas flame to heat the fiber by a gas mass flow controllers to produce a flame with Hydrogen or a mixture of gases like butane or propane, combined with oxygen. (Garcia-Fernandez et al. 2011) [41]. The flame is applied to the fiber in a smooth bidirectional movement along a predetermined length, generating a sufficiently temperature, around 990 ^{o}C [34] for melting and stretching the fiber. In Figure 3.7, a standard flame-brushing scheme is illustrated.

This results in the elongation of the fiber, accompanied by a reduced diameter at the brushing region, referred to as the hot zone. The desired taper shape of the fiber can be precisely defined by controlling both the movement of the flame and the pulling speed of the fiber. Flames are known to be susceptible to fluctuations induced by turbulent gas flow and residual air currents within the environment.
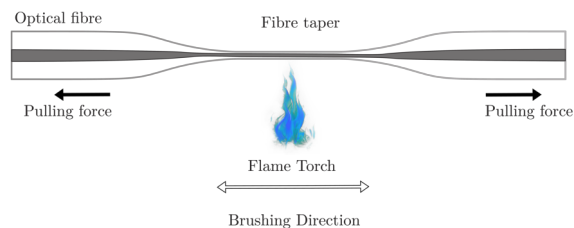
FIGURE 3.5:   Flame brushing method

These fluctuations can result in irregularities along the waist diameter of the taper. Also, contaminants such as the content of hydrogen (OH) radicals caused by flame combustion, such as soot particles, can adhere to the fiber surface during the tapering process (G Brambilla 2010) [42]. Nevertheless, the flame brushing technique allows the manufacturing of adiabatic, micro and nanoscale tapered fibers (∼200 nm).

3.2.2 Ceramic microheater technique

The utilization of a ceramic microheater enables precise linear temperature increase of a resistive material with the application of voltage. This microheater comprises a tungsten wire meandering around a ceramic core in a closed keyhole shape, causing a temperature rise through the applied current. The resistance of the wire causes it to heat up and emits radiation similar to that of an incandescent light bulb. The elevation of temperature occurs within a highly confined, small cylindrical volume along the heater. The fiber is positioned at the center of this cylindrical area, typically with a diameter of 2 mm and a length of 22 mm.

Figure 3.6 shows an illustration of ceramic microheater, whereby using this technique it is possible to make a brushing movement of the oven for increase the heating length of the fiber.[43]. This system can achieve maximum temperatures of up to 1700 degrees Celsius [44].

It is noteworthy that the operation of this system typically requires a pre-heating period, to stabilize the temperature effectively of the silica for optimal softening of the fiber. The use of this fabrication technique allows for the production of adiabatic nanoscale tapered fibers[1].

Additionally, ceramic microheater sources are sensitive to production lifespan because of their susceptibility to damage from thermal shocks resulting from

FIGURE 3.6: Ceramic microheater method

rapid temperature changes. This limitation can adversely affect the reproducibility of the fabrication results. Finally, it should be noted that these devices come with a higher cost, which needs to be taken into consideration.

3.2.3 CO$_2$ laser technique

The CO$_2$ laser serves as an effective heat source, softening the fiber directly by targeting the laser into the fiber through the absorption of laser radiation. This method eliminates concerns related to fiber cleanliness, as any combustion residues are promptly removed during the process, resulting in a rapid thermal response and easy control of the heating temperature through a precise application of voltage. [45].
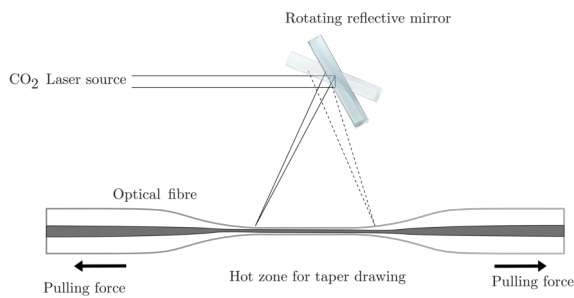
FIGURE 3.7: CO_2 Laser method

Ward et al. [46] reported the minimum diameter obtained using CO_2 Laser heating from 3-4 μm. In the fabrication process, the power output and the capability to scan the beam across the fiber are not affected by air currents or other adverse environmental conditions. The temperature of the laser beam typically ranges from 1500 to 2000 K [47], depending on the power of the laser. However, it is important to consider that the implementation of this technique involves the initial very high cost of the CO_2 laser. Additionally, operating the CO_2 laser demands strict adherence to safety requirements, as it falls under the Class 4 laser classification.

3.2.4 Electric arc discharge technique

Several commercially available optical fiber splicing machines incorporate the capability to tapering the fiber. These machines feature a complex system of cameras and electrodes that automate align the optical fibers between the electrodes using two translation stages. This system produces an effective heating zone through the application of an electric arc discharge generated between the electrodes.
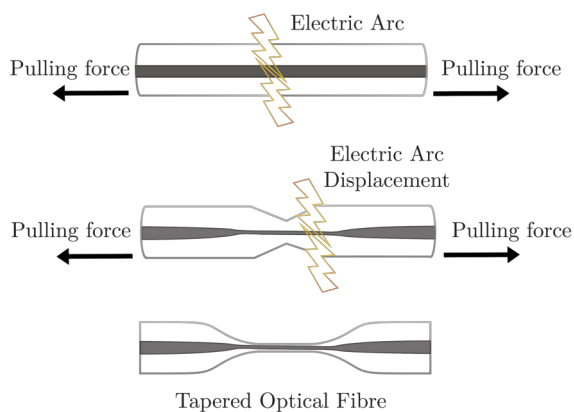
FIGURE 3.8: Electric Arc Discharge method

Figure 3.8 illustrates the application of electric arc discharge, where translation the electrodes or the fiber enables coverage of a greater length of the fiber. This is because the arc is small and only covers a couple of millimeters at a time.

This electric arc transforms into a plasma state, ionizing the air and creating an effective heating source, reaching around 2100 degrees [48].

The resulting tapers reported using this technique achieve a diameter of 10 and 3 μm [49] ,[50] . A limitation using the splicing machines is that the taper are short in length due limited travel distance of the translation stages.

3.2.5   Summary

While conducting this comparison, we investigated and contrasted the utilization of the plasma as a new alternative to existing methods. The table below summarizes the results obtained using these techniques, according to literature.

Tapering Technique	Process Time (min)	Waist Diameter (μm)	Taper Length (mm)	Insertion loss in air (dB)	Reference
Flame brushing	~ 3	1.1	15	1.0	[51]
Ceramic micro-heater	4	$\sim$250 nm	40	0.20	[1]
CO_2 Laser	N/A	3-4	40	0.20	[46]
Electric arc	1	3	10	0.16	[49] [50]
Plasma	0.12	8	15	0.96	**This work**

TABLE 3.1: Features of tapered fibers fabricated by different heating methods

Therefore, plasma combines the following advantages:

- **Economical Implementation:** plasma generation requires a commercially available, ultra-low-cost and safe circuit.

- **Durable Electrodes:** The proposed electrodes exhibit high resistance to the effects of discharges, resulting in prolonged durability.

- **Safety and Simplicity:** Unlike other methods, the plasma technique eliminates the necessity for flammable gases, enhancing overall safety while streamlining the operational procedure. Using a commercial flyback (see materials list) ensures safe operation through adherence to operational guidelines and safety protocols.

- **Accessible Replication:** The successful replication and operation of this method demands only fundamental/basic engineering knowledge, reducing barriers to replication and implementation.

- **Efficiency in Taper Fabrication:** The plasma technique boasts rapid manufacturing of tapers, aligning with the demands of time-sensitive applications.

Limitations of the utilization of the plasma:

- Intense air currents in the heating zone can disturb the plasma beam, leading to irregularities in the taper structure.

- The initialization of the plasma produces a strong pressurization of the air and this high energy can break and burn the fiber.

Chapter 4

Optical fiber tapering rig

This chapter outlines the process of designing, constructing, and operating a computer controlled electro-mechanical rig dedicated to manufacturing tapered optical fiber structures with a precise and controllable process by employing the plasma-based heating technique. The rig offers significant advantages in terms of cost-effectiveness, ease of operation, and simplicity for replication. Finally, we propose recommendations for future enhancements to optimize its capabilities.
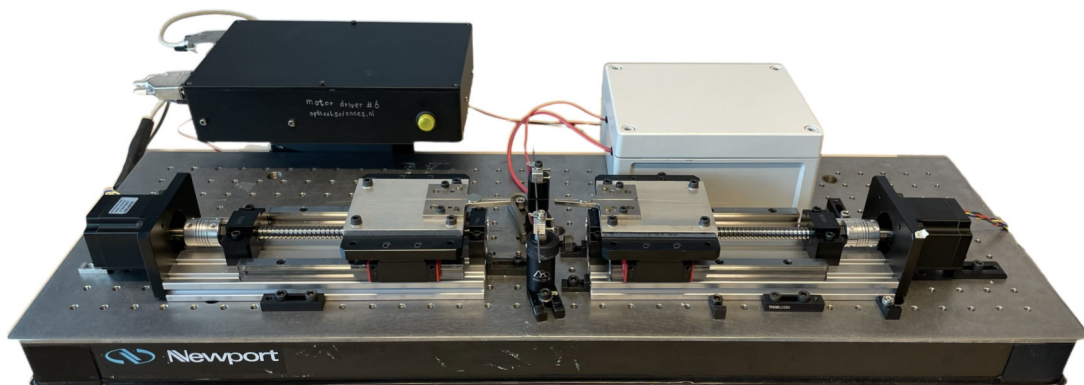
FIGURE 4.1: fiber pulling rig

4.1 Hardware description

The tapering rig proposed in this work comprises a mechanical setup controlled by a circuit that receives operational instructions through a computer. This configuration allows collaborative operation between the elements involved, resulting in a semi-automatic system for manufacturing tapered optical fibers. The illustration of the electro-mechanical rig is shown in Figure 4.2 showcasing the elements: 1) motor control module, 2) computer, 3) plasma module, 4) ultra-low vibration translation stages, 5) linear guides, 6) stepper motors, 7) heating section: with two tungsten electrodes holding with optical posts and 8) optical table.
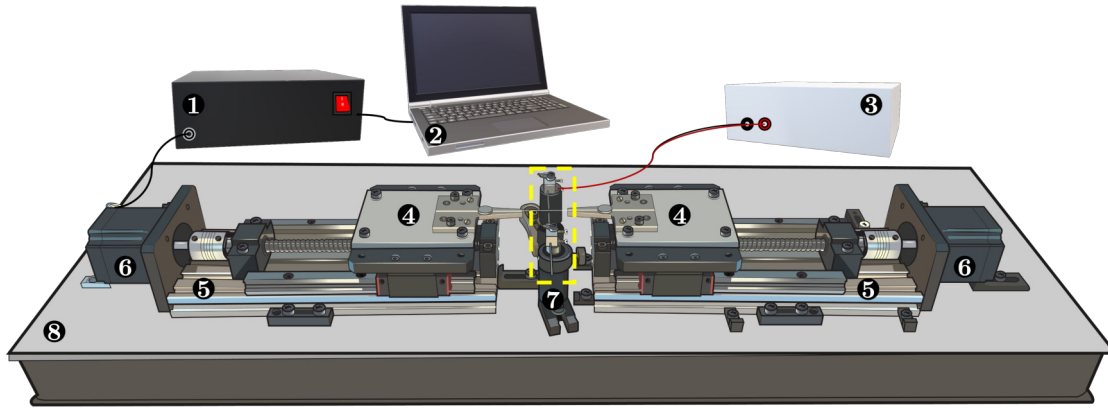
FIGURE 4.2: Illustration of the fiber pulling rig

The operating principle of the rig is the well-known fused tapering process, and it starts by pulling the fiber using two ultra-low vibration translarion stages mounted on a linear guide module. The stages move in the same direction, but the right stage moves at a speed 35 times faster than the left platform, covering a distance 35 times greater than that of the left, to simultaneously pull and transport the fiber through the plasma (see Figure 4.3).

The stages achieve precise linear movement by the utilization of high-precision standard stepper motors that rotate a ball screw , enabling bidirectional movement of the stages. The platform glides smoothly on two metal linear rails with a low friction coefficient, ensuring a stable motion and reduced vibrations. The movement of the motors allow the user to define the desired linear travel distance of the stages with resolution $\sim 20~\mu m$ with the utilization of the micro-stepper driver TB6600. This driver amplifies the resolution of angular motor movement, as a result, increase the resolution of the linear distance.

The acceleration and speed of the stages can be customized in the programming code, where acceleration plays a crucial role in the fabrication tapering process. When the pulling action is performed at a higher speed, the dimensions of the waist diameter become significantly smaller. Conversely, if the pulling is performed at a slower speed, the waist diameter decreases less. The acceleration essentially dictates the speed of the execution of the movement, and opting for the highest possible ac-

celeration of $10^{10} \ m/s^2$, demonstrates the optimal performance of the motors. This choice enables precise and rapid movements, contributing to the overall efficiency of the system.

During the fiber pulling process, a Zero-Voltage Switching (ZVS) Module using a Tesla coil generates plasma by inducing high voltage ($>$10kV), discharges that ionize the air between a pair of tungsten electrodes. The fiber is fixed with a neodymium magnet in the V-groove, positioning it the bare fiber section between the tungsten electrodes (see Figure 4.3, A), serving as the heating region where the plasma is generated, with temperatures exceeding 2000 degrees Celsius [52]. This extreme heat effectively softens the fiber, subsequently enabling its diameter reduction as it is drawn, resulting in a mechanically stable, tapered, biconical structure. These characteristics are discussed in detail in Chapter 3.

(A) Plasma OFF

(B) Plasma ON

(C) Elements: a) optical fiber, b) Tungsten electrodes, c) Neodymium magnets and d) V-groove, e) platforms, f)linear guide and g) ball screw
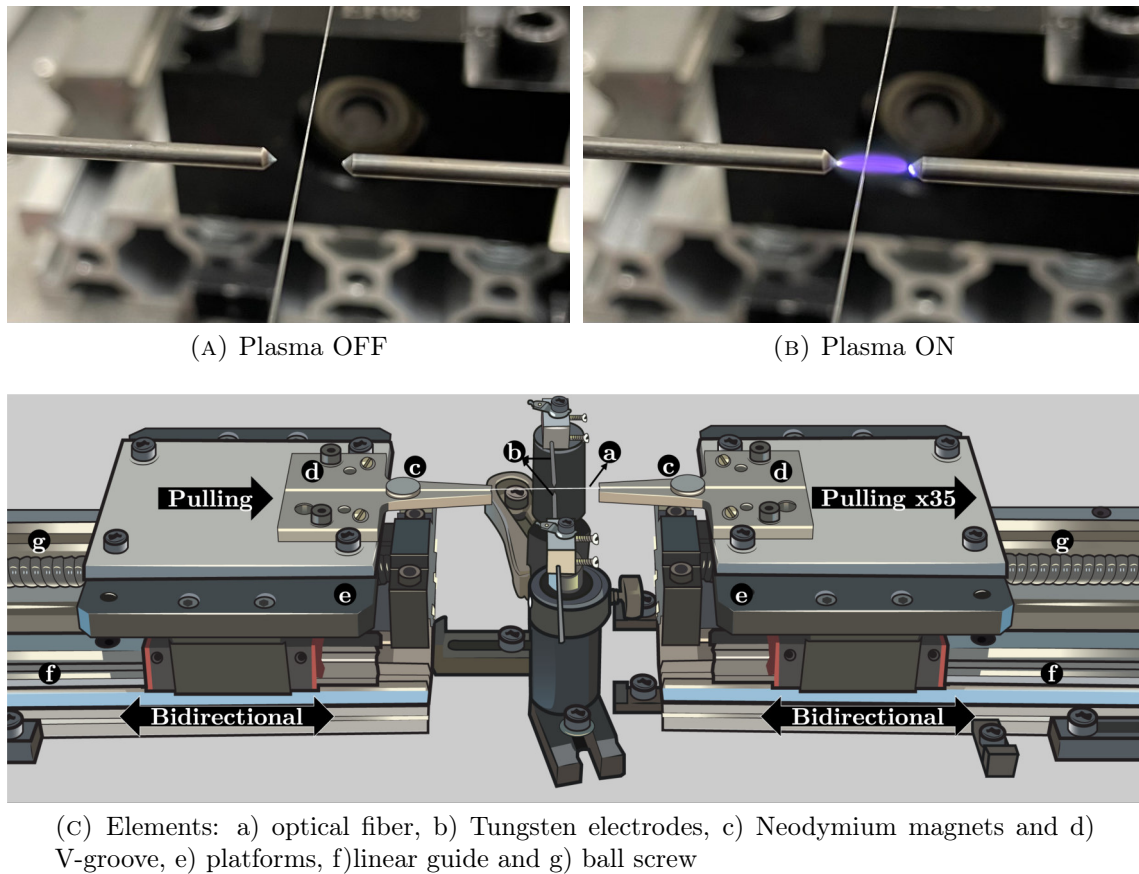
FIGURE 4.3: Pulling and heating section

The taper length is determined by the travel distance of the faster translation stage, represented by the Right Platform. The lowest stage (Left Platform) does not influence the determination of the taper length; however, it moves in the same direction; by moving slower, it exerts an opposing force to attain the fiber pulling. With this configuration, both platforms execute the movement at the same time, but covering

different linear distance and speed, given by the following relation:

$$t_1 \ [s] = \frac{35x}{35y} \tag{4.1}$$

$$t_2 \ [s] = \frac{x}{y} \tag{4.2}$$

where t_1 and t_2 represent the operation time in seconds [s] for the right and left platforms, respectively. Here, x represents the linear distance [m] and y, indicates the speed [m/s]. It is noteworthy that $t_1 = t_2$, which indicates the simultaneous movement of the platforms covered in the same time duration.

The waist diameter is the result of the interplay between two key factors: 1) the duration of exposure of the bare fiber to the plasma and 2) The speed at which the platforms execute the pulling. The code already specifies the optimal values for the plasma activation time and acceleration, determined through experimental tests. The travel distance and speed of the translation stages are determined by the user according to the dimensions required of the tapered fiber.

4.2   Mechanical setup

The mechanical setup (refer to Figure 4.4) comprises two linear guide modules[1] positioned in a front-to-front orientation, maintaining a 100 mm separation between them. The tungsten electrodes are positioned through the use of optical posts, aligning them between the linear guide modules at the V-groove height, with 5 mm spacing between the electrodes. Moreover, the use of a holographic optical table facilitates precise alignment of the elements due to its perfectly flat surface. Additionally, the holes are designed to mitigate external vibrations, which further aids in reducing the already small vibrations of the linear guide modules.
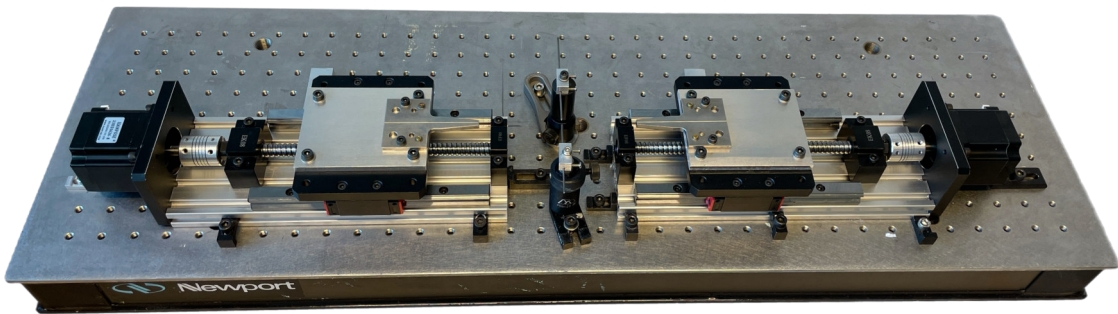
FIGURE 4.4: Mechanical Setup

---

[1]NEMA23 HPV6 sfu1204 with stepper motor

4.2.1 Linear displacement

The stepper motor executes rotational motion to the ball screw, enabling bidirectional linear movement of the platform. The ball screw has a resolution of 4 mm per revolution of the screw shaft, resulting in a linear displacement of the stages by 4 mm for each revolution. Notably, the stepper motor requires 1600 steps to complete a single revolution of the ball screw. Table 4.1 outlines the specifications of the linear guide module, providing additional details that are visually represented in Figure 3.5.

Linear Guide	
Total effective stroke [mm]	100
Ball screw type	SFU1204/SFU1210
Lead	4 mm
Positioning accuracy [mm]	0.05
Linear displacement resolution [μm]	$\sim$20

Stepper Motor	
Steps per revolution	1600
Step angle (deg)	1.8

TABLE 4.1: Linear guide module specifications

Hence, it is possible to precisely determine the linear displacement of the platforms by establishing a correlation with the number of steps executed by the motors. This relationship is expressed by the following equation:

$$1 \text{ [mm]} = 400 \text{ steps}$$

The total travel distance of each platform is 100 mm. The following diagrams of the Linear Guide Modules provide the dimensions of the elements involved in this module, as well as the sizes of the holes of the plate of the platform to adapt a base with the V-groove, (all values in millimeters).
The utilization of the Microstepper Driver TB6600, offers the capability to significantly increase the angle resolution of motors, thereby improving the precision of linear displacement up to 0.02 millimeters, which is equivalent to 20 micrometers. Since the taper length is required in millimeters, this level of precision ensures the attachment of a very precise linear movement.

As previously mentioned, the right platform in the rig determines the taper length, but if this platforms is configured with a 35 factor to cover a linear distance of 1 mm, 400/35 steps are required to execute the rotational movement of the stepper motors equivalent to this linear distance, as indicated by the following relation:

$$1[mm] = \frac{400}{35} steps \tag{4.3}$$

Subsequently, the user specifies the desired taper length in millimeters by entering this value in the plasma pulling rig software. The program receives the taper length
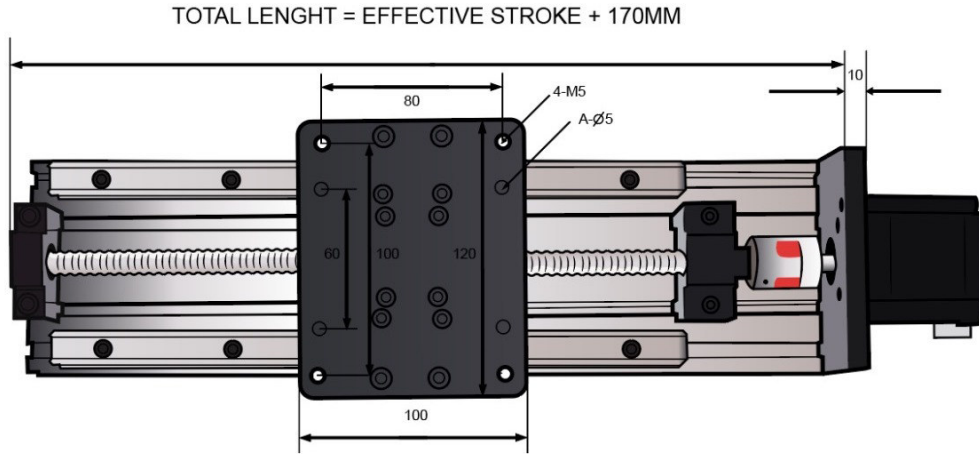
FIGURE 4.5: Linear guide module diagram with specifications

value and proceeds to move the right platform to the corresponding linear distance, following the relationship outlined in Equation 3.4.

$$Taper\ length\ (Rigth\ platform) = \frac{400}{35}l \tag{4.4}$$

Where l, corresponds to the taper length in millimeters. With this relation is possible to determine the parameters in the standard values for the speed (meters per second), time (seconds) and distance (meters), where:

$$speed = \frac{\frac{400}{35}x^{-3}[m]}{time[s]} \tag{4.5}$$

4.3 Electrical circuit

The mechanical configuration requires a motor control module to precisely regulate the movement of the platforms, encompassing speed and acceleration parameters. In addition, it involves an interconnected high-voltage circuit for plasma generation, the control of which is facilitated by a relay. This electrical system is operated through the use of the Arduino UNO and the instructions are provided via the Monitor Serial of the Arduino IDE.

igure 4.6 presents the circuit diagram, offering a detailed view of the component connections [2]. The motor control module initiates the circuit by receiving power from a 12 VDC, 3 A power supply. The Microstepper Driver regulates the power supply to the stepper motors, providing 12 VDC with a maximum output current of 2.8 A. However, in practice, the motors require only 0.4 A, as determined by experimental measurements.

---

[2]The assembly instructions of the motor control module are described in the Appendix A
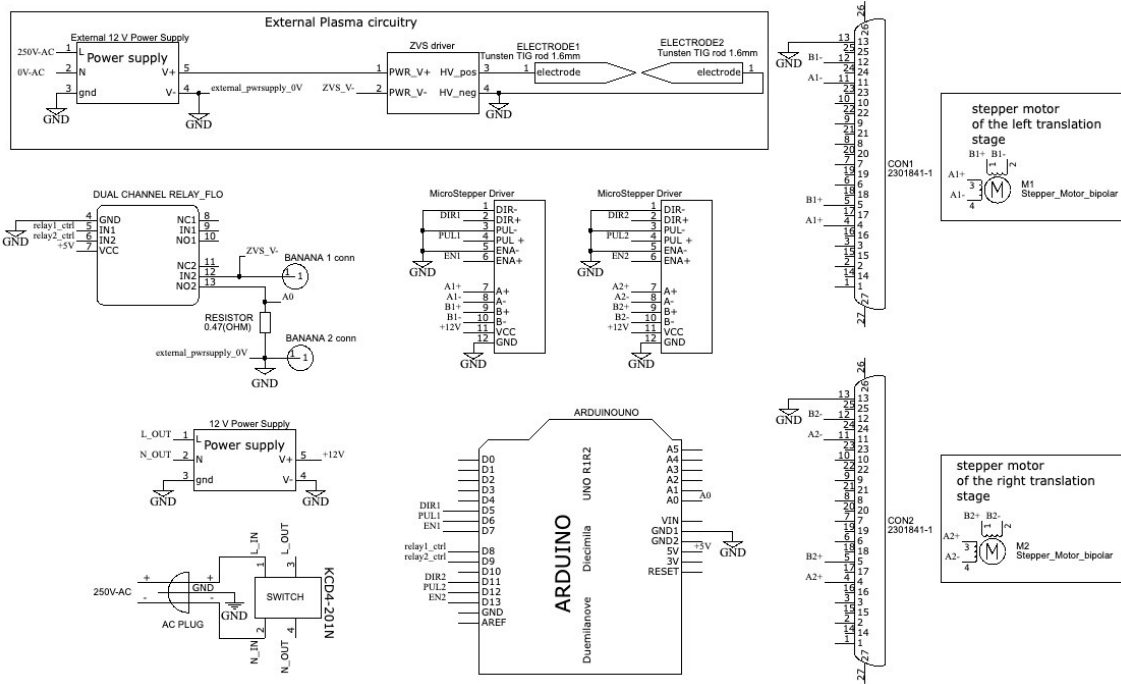
FIGURE 4.6: Circuit diagram of the motor control module

The rotational movement of the motors is governed by the input signals and direction within a common-anode connection. In this configuration, the Arduino initiates the motion by setting the signal to 0, activating the rotation either in a clockwise (CW) or anticlockwise direction (ACW), determined by the programming code. The specific direction is contingent upon the intended movement of the platform, whether it is to the right or left.

Simultaneously with the initiation of motor movement, the relay, initially set as normally open, closes the circuit. This action activates the external plasma circuit through the connection of an external 12 VDC 2 A power supply, linked in common ground with the motor control circuit. The on/off duration of the plasma is established within the programming code, aligning with the period during which the motors execute the movement of the platforms.

The ZVS driver is depicted in Figure 4.6, with the high-voltage module stage situated at the output of this module. This circuit multiplies the input power by a factor of 1000, resulting in an output exceeding 12 kV and 24 kW. The V+ and V- outputs from the Tesla coil are connected to tungsten electrodes, where plasma is generated through high-voltage discharge. To ensure the production of homogeneous plasma, it is necessary to apply a current of at least 2 A to the plasma power supply. Experimental determinations have established that there is no need to increase the power of the input in the ZVS driver, as doing so would elevate discharge power and temperatures to the extent that the optical fiber would burn, due to the extreme temperatures that the plasma produced by the plasma resulting from electric discharge, surpassing 10,000 degrees. [52].

4.4   Tapering process

To operating the rig, a desktop application for the Microsoft Windows system was developed using Visual Studio. This application provides a Graphical User Interface GUI with all the commands needed for taper fabrication. It is designed to be opened and run easily, allowing users to select the appropriate Arduino USB port. Once running, the commands are sent via serial communication between the GUI and the Arduino UNO. Figure 4.7 shows the GUI for operating the rig.
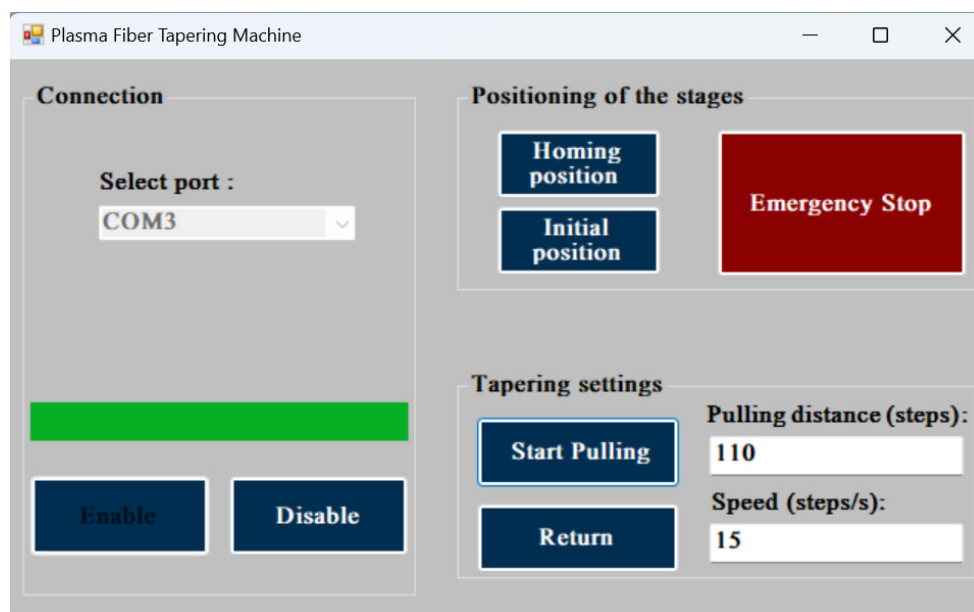
FIGURE 4.7: GUI to operating the rig

The positioning and taper settings must be provided by the user by following the instructions also described in the next flow diagram:
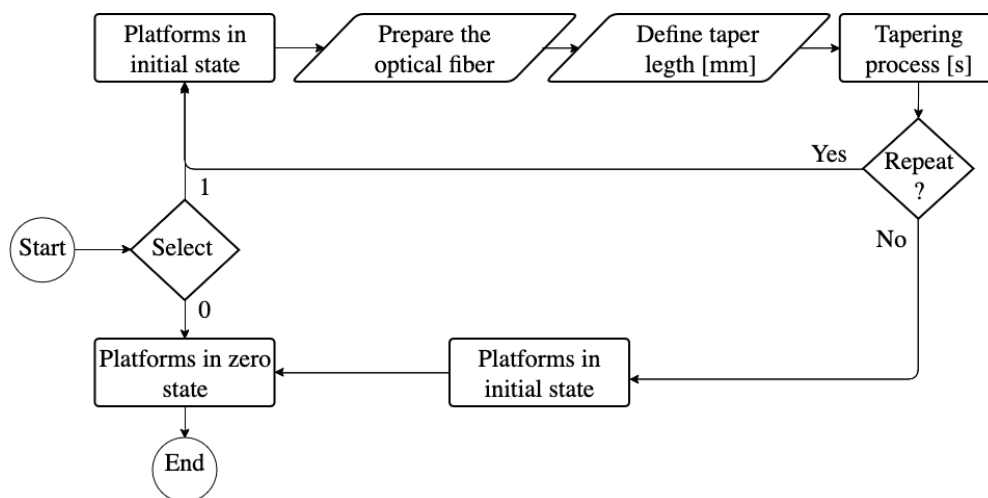
FIGURE 4.8: Flow diagram of the tapering process

1.- Initializing the pulling rig: The first step consists on moving the stages in the initial position where the homing position the stages are situated at the end of the travel track of the the rail, maintaining 100 mm gap between them (see Figure 4.9A). In the initial position, the stages move 30 mm in opposite directions, now with a separation of 160 mm between them (see Figure 4.9B). This configuration enables bidirectional movement to pull and translate the fiber.
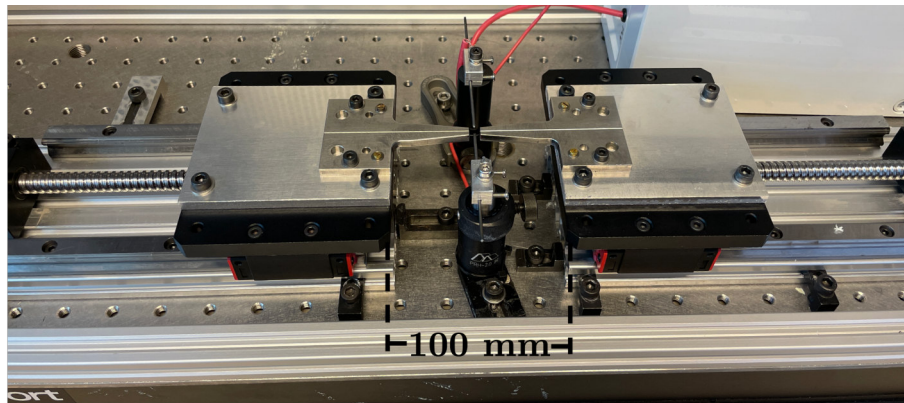
(A) Homing position
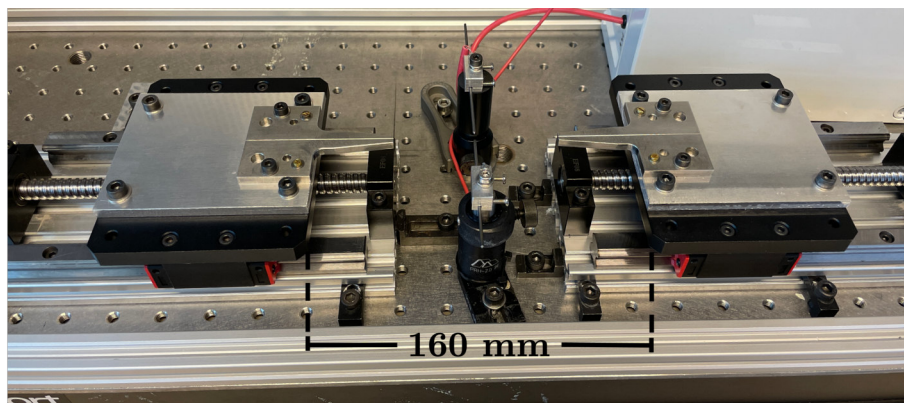
(B) Initial position

FIGURE 4.9: Pulling and heating section

2.- Preparing the fiber: Once the rig is initialized, preparing the optical fiber involves removing the coating from the section that will be tapered. Depending on the desired tapered length, we recommend adding an extra two centimeters at the ends to ensure sufficient bare fiber beyond the tapered section. Subsequently, the fiber is placed in the V-grooves and fixed using neodymium magnets, ensuring that the fiber is sufficiently taut and well-aligned between the electrodes.

Considering that the right translation stage performs the displacement to the right, the bare fiber is positioned 20 milimeters to the right before the electrodes. This ensures that the plasma will cover the desired length of the taper and that the taper will be positioned in the middle of the bare fiber section.
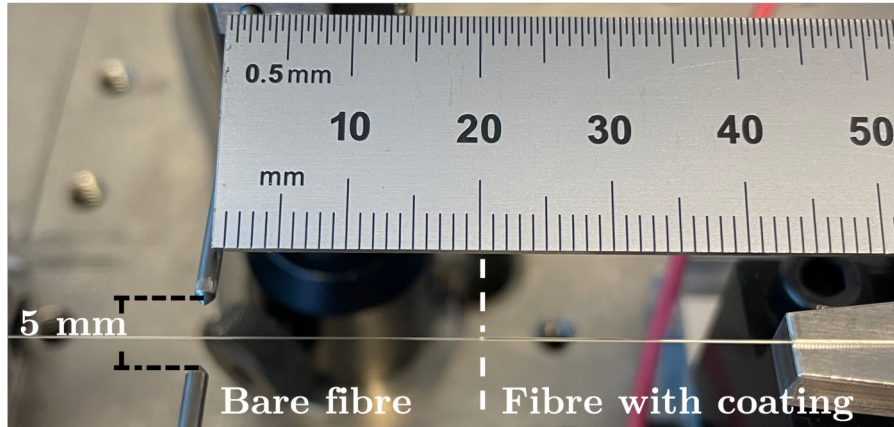
FIGURE 4.10: Fiber placement

3.- Selection of the taper dimensions: By entering the required length in steps and speed in (step/s), the motors will initiate the movement of the platforms, and the plasma will activate during the pulling time. It is important to note that the pre-heating of the fiber is unnecessary due to the extreme temperature of the plasma, which immediately softens the fiber upon contact. In this case, we have chosen to set a constant speed of 15 steps/s, which is equivalent to $4x10^{-4}m/s$, according to Equation 3.5. This chosen speed typically achieves a waist diameter of $8 \mu m$.

4.- Tapering process: This is the most crucial step in the taper manufacturing process, involving the pulling and heating of the fiber within the plasma. The bare fiber must be precisely aligned within the plasma beam with a diameter approximately 1 mm during the pulling process. The optical fiber remains constantly taut as the right stage exerts strong tension, ensuring the continuous passage of the fiber into the plasma. Finally, immediately upon completion of the stages movement, the plasma is deactivated, and the tapered fiber is ready for removal.
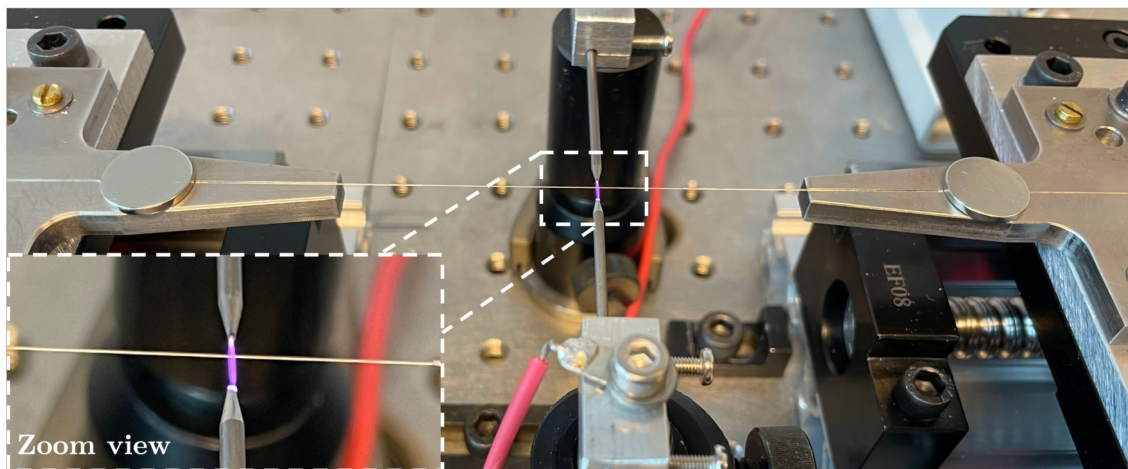
FIGURE 4.11: Flow diagram of the tapering process

5.- Repeat the tapering process: After each tapering process, the stages must be returned to the initial position. If the user wishes to finish the process, the stages must be first returned to the initial position and then to the homing position to disable the rig.

4.4.1 Safety and security requirements

The high voltage produced by the Tesla coil of the ZVS module emits considerable electromagnetic noise, which can disturb nearby electrical components. To isolate this electromagnetic noise, an aluminum Faraday cage enclosure was constructed. This enclosure maintains a constant electric field inside when a nonzero electric charge is applied. The frequency range of the electric field was measured using a digital oscilloscope at a distance of 10 centimeters from the electrodes, resulting in a frequency range of 60 kHz as is plotted in figure 4.12 as signal 2, while signal 1 in the same figure corresponds to the voltage measured outside the closed Faraday enclosure.
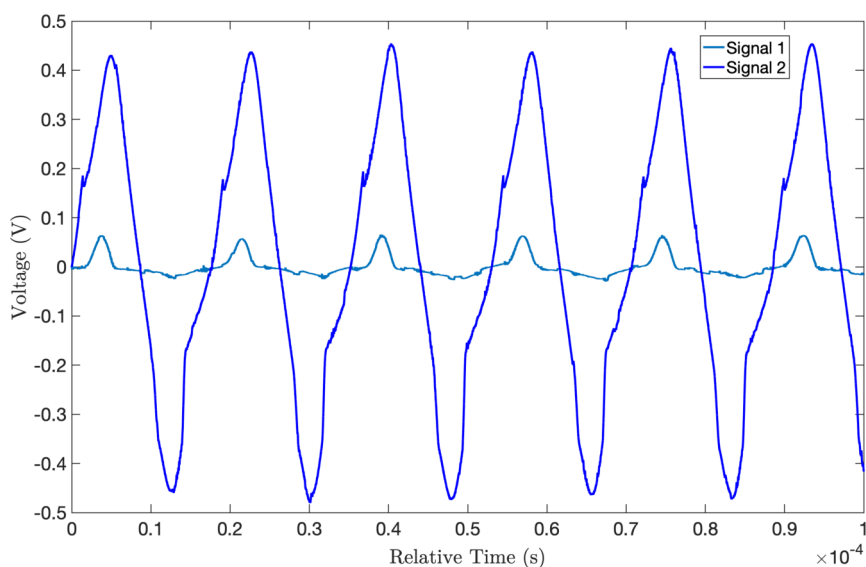
FIGURE 4.12: Plasma frequency measurements: Signal 1 is taken at 10 cm from the electrodes inside the enclosure, while Signal 2 measures the voltage outside the enclosure.

Figure 4.13 shows a photograph of the rig enclosed in a cage, designed based on the Faraday cage principle [53], ensuring that the hole size in the mesh is significantly smaller than the wavelength of the electromagnetic waves produced by the plasma. Given a frequency of 60 kHz, the corresponding wavelength is 5000 meters. The mesh used in the cage has a hole diameter of 1 cm, which is much smaller than the wavelength produced, ensuring effective isolation of electromagnetic noise. Furthermore, the aluminum cage has 1mm thickness and a high density of holes per square meter. This configuration creates a dense barrier to electromagnetic waves, ensuring effective shielding against electromagnetic interference.
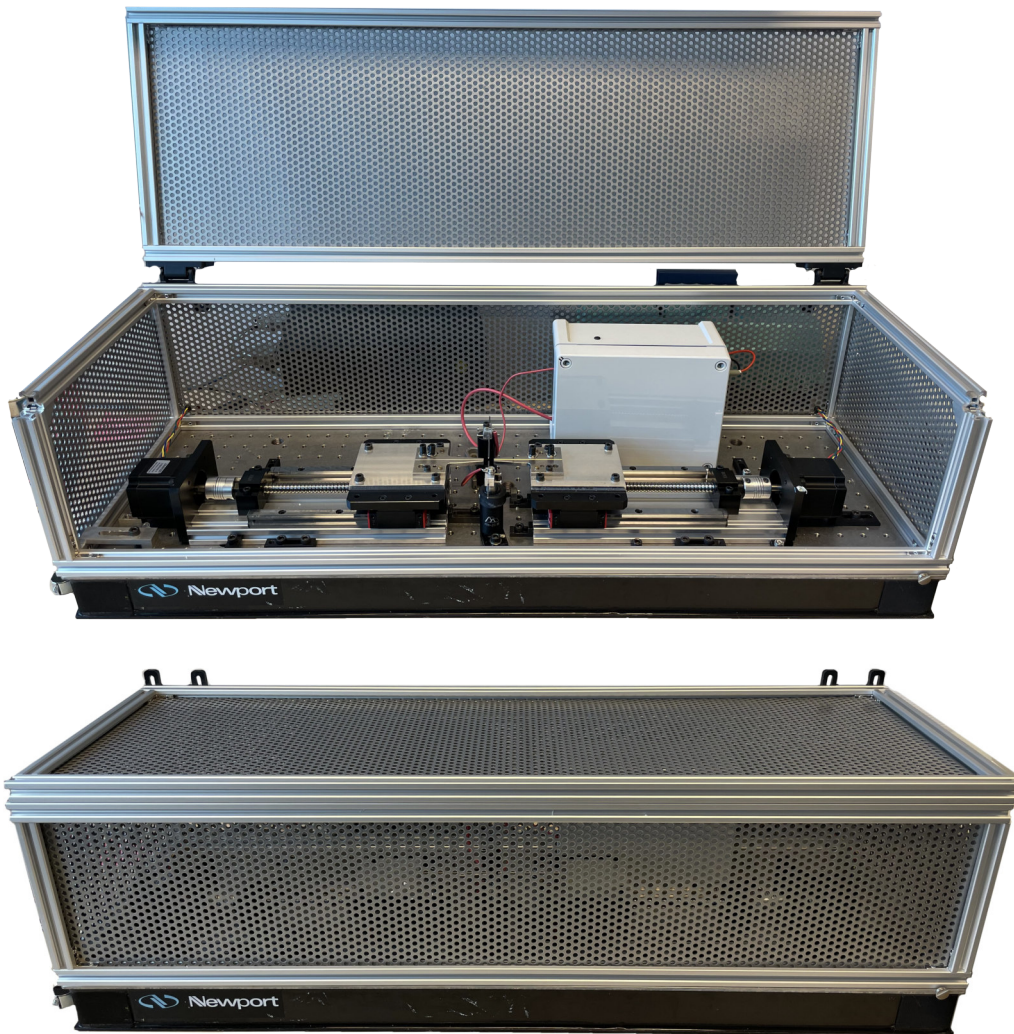
FIGURE 4.13: Plasma pulling rig enclosure in an aluminum Faraday cage

Chapter 5

Characterizing the taper

For the tapered optical fiber fabrication process, it is important to consider the symmetry of the tapered fiber, the light transmission properties and the adiabaticity criteria to demonstrate the quality of the fabricated devices. This chapter outlines the characterization of the taper dimensions, whereas the taper profile is evaluated to determine the shape of the tapered transition, the diameter of the waist, and the taper length. Moreover, evaluation of the optical properties of these structures is conducted, such as light transmission losses, spectral response, and adiabaticity criteria. In addition, a statistical study of the taper dimensions and the optical response is presented to validate the fabrication process of the rig, demonstrating good reproducibility. Finally, we demonstrate the fabrication capabilities of the rig by manufacturing tapers with lengths ranging from 2.5 to 15 mm, along with the analysis of typical transmission spectra.
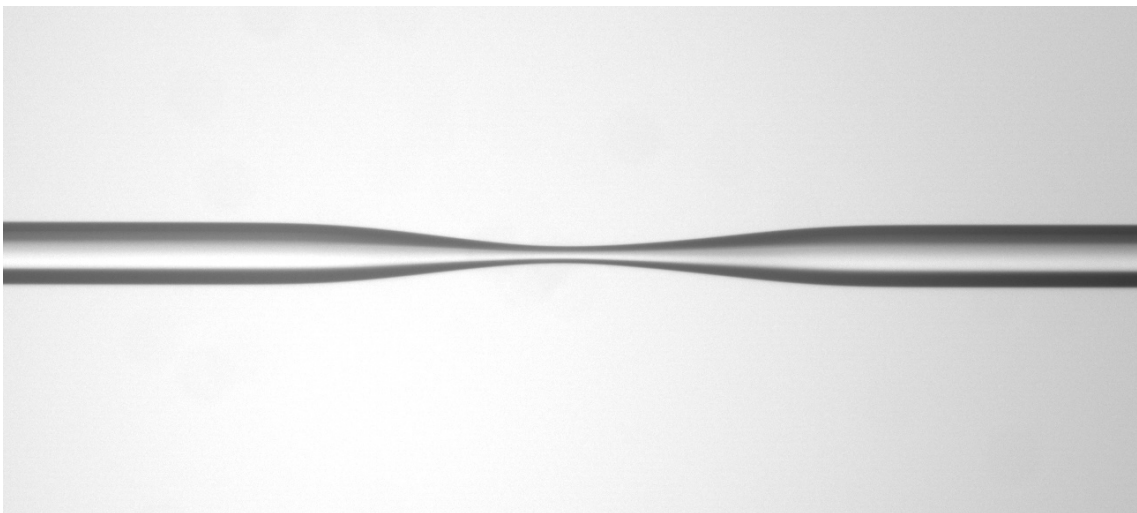
FIGURE 5.1: A photograph of an optical fiber taper

5.1   Taper dimensions

The taper dimensions were measured using a photo acquisition setup, developed for this purpose in house, to take a photograph of the fiber and then analyze the image by the relation of the pixel size of the camera and the real scale of an SMF fiber. Employing this technique allows to evaluate the shape of the down and up transitions and   the   taper   dimensions.
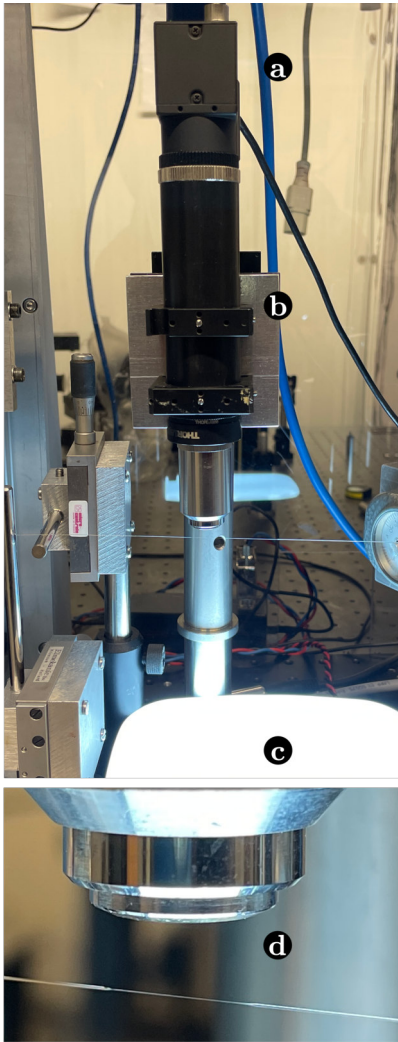
FIGURE 5.2:   Photo acquisition setup

Figure 5.2 shows the photo acquisition setup, including a) camera , b) microscope, c) optical fiber, d) a LED light, and e) shows the zoom section of the lens focusing the fiber.

To capture a well-contrasted photo of the fiber, we use a FLIR BFLY-U3-23S6M-C monochromatic camera with 5.86 µm * 5.86 µm pixels unit cell size of 5.86 m * 5.86 m pixels in conjunction with a microscope with an objective of 10x magnification; Numerical aperture (NA) of 0.25 and tube length of 10 cm.   Moreover, a shadow image is obtained by illuminating the fiber from below using a commercial white LED light to detect the edges.   The picture is focused using a motorized x,y translation stage with micrometer resolution, where the camera and microscope are mounted to ensure the best image quality.   The fiber is manually positioned and tensioned by using the translation stages of the rig to translate the tapered region across the microscope.

A photograph of the fiber is taken every 0.1 mm in the tapered region. We start by capturing photos of the untapered fiber and then translating the fiber to the right. This means that the pictures will be taken from the down-tapered transition, as shown in Figure 5.3 (a), and cover the entire tapered region until the untapered fiber passes the up-tapered transition, shown in Figure 5.3 (c).

The compilation of the pictures allows for the observation of the edges of the shadows. The camera pixel size is 0.7 μm,then we can quantify the relation of the pixel size to the nominal diameter of an SMF which corresponds to the diameter of a single-mode fiber (SMF) of 125 μm, then by knowing this relation the pixels for the
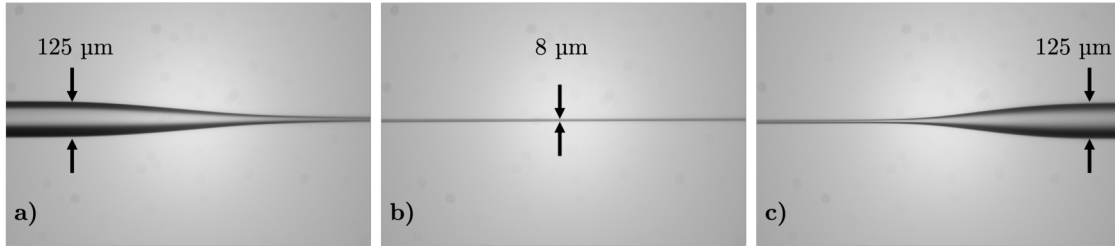
FIGURE 5.3: A taper photograph with L= 10 mm and a waist diameter of 8 μm, depicting a) down tapered transition, b) waist, and c) up tapered transition

smaller fiber can be calculated and recorded as well as the position. The diameter values are obtained to obtain the fiber profile as illustrated in Figure 5.3.

5.1.1 Fiber profile

Figure 5.4 shows the fiber taper profile of the extract values obtained with the image processing of 165 pictures in the case of the taper with 10 mm of length. The thinner diameter of the tapered section is $8\mu m$ ($\pm 0.3\mu m$), showing slight variations in values. However, it remains constant within the 7 mm length of the waist section.
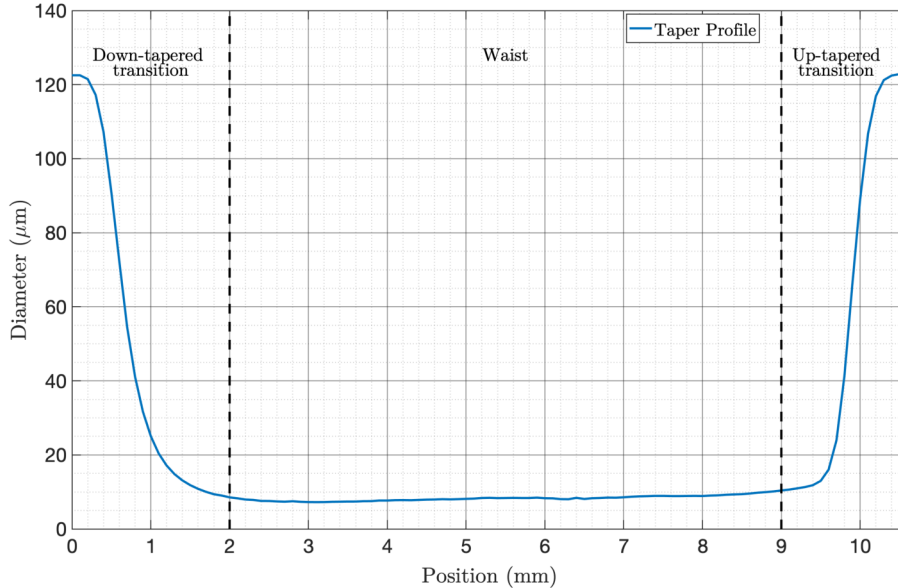
FIGURE 5.4: Taper profile

In the case of tapered transitions, there is a 2 mm length between the two preceding values of the diameter of the untapered fiber and the first diameter value of the waist for the down-tapered transition. Similarly, there is a 2 mm length from the last diameter value of the waist to the two succeeding diameter values of the untapered fiber in the case of the up-tapered transition. This distance of transitions

when the fiber is reduced is considerably short in comparison with the techniques addressed in Chapter 3.

The abrupt slope of the tapered transitions allows for the higher modes excitation because part of the light escapes to the air and then recombined into the microfiber with a variation in the velocity with respect of the fundamental mode, and this slight variation in propagation velocity produces multimodal interference. Besides, the Gaussian propagation profile of the modes in the tapered region presents a large evanescent field, which leads to a greater interaction of the light with the surrounding medium. In consequence, there are considerable light transmission losses, where the adiabaticity criterion is not fulfilled due to the abrupt inclination angle and the losses obtained, and we can support this affirmation by evaluating the shape of the fiber and the losses. Nonetheless the main application reported using the tapered fiber is for the sensing application [10], where the non-adiabatic taper is used directly as a sensor.
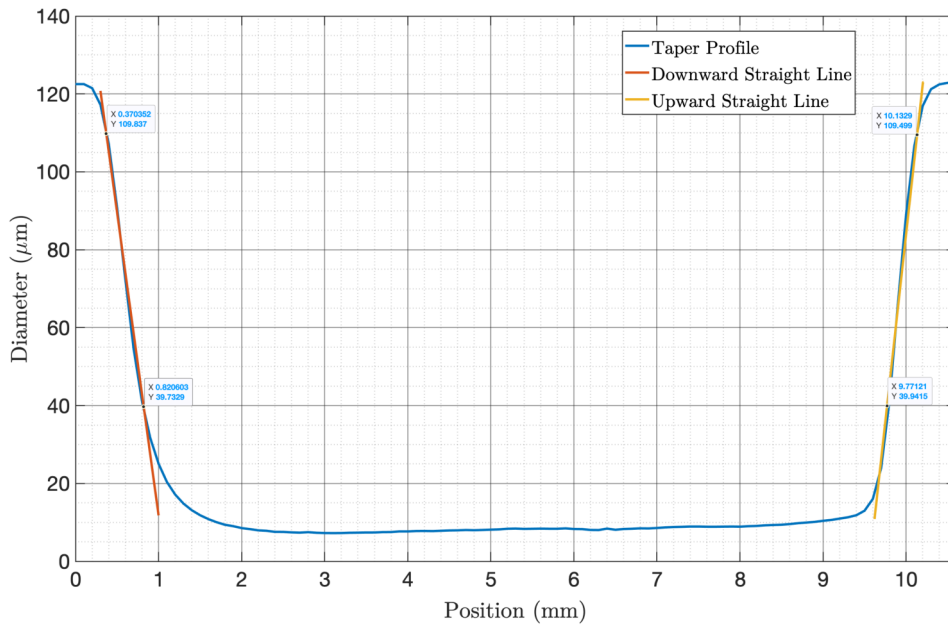
FIGURE 5.5: Straight lines in the Down and Up tapered transitions

The shapes of the tapered transitions are not exactly the same; the down-tapered transition exhibits a smooth shape compared to the up transition, which is more abrupt. In Figure 5.5, a straight line is drawn along the values of the down and up curves. The slope value is calculated using the coordinates of two points on a line $P_1(X_1, Y_1)$ and $P_2(X_2, Y_2)$. This value indicates the tangent of its inclination angle, as described by the following equation [54] :

$$m = tan \ \theta = \frac{Y_2 - Y_2}{X_2 - X_1} \qquad (5.1)$$

Where m is the slope value and θ is the inclination angle.

Then, the slope value and its angle of inclination are calculated for both lines to compare and analyze the difference between them, using the following calculated values:

Downward line: m =-155.6995 and θ= 89.632 degrees
Upward line: m= 192.3037 and θ = 89.7021 degrees
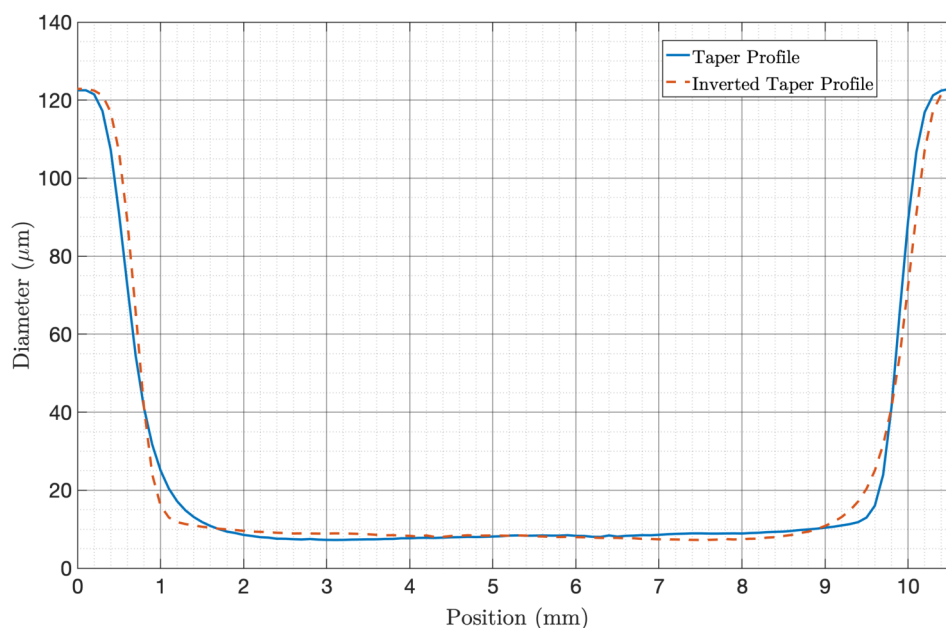
FIGURE 5.6: The comparison with the inverted taper profile

The plot of the inverted taper profile superposed to the taper profile allows one to distinguish the sections of the trace that present more differences (see Figure 5.6). The main variations are in the section, whereas the curve reaches the waist dimensions.

The difference in these evaluated parameters of both transitions provides us with insight into the variation of the transitions achieved using plasma. Nonetheless, we acknowledge that, while using this heating technique, we can obtain a biconical taper shape with a consistent profile.

To evaluate the capabilities of tapering rig of the fabricated devices, we begin by fabricating a short taper to evaluate the behavior of the mechanical system. A pitch of 15 steps per second is predetermined and the travel distance for each cone is adjusted based on the desired taper length. The transition of the tapers follows the same pattern as described previously, confirming that the shape obtained is attributed to the heater and the performance of the rig.

5.2 Statistics of the fabrication process

To demonstrate the level of control over the fabrication process, we manufactured several tapers and calculated the manufacturing process's statistics. In the following table, we present the average results of 100 tapers fabricated with 110 steps of travel distance and 15 steps/s, the temperature and humidity parameters were measured for every taper fabricated as two representative conditions for the glass processing, resulting in:

Number of tests	Temperature ($^{\circ}C$)	Humidity (%)	Taper length (mm)	Waist length (mm)	Repeatability (%)
100	21.4	41	10.6	9.44	7.3

TABLE 5.1: Taper fabrication statistics

In Figure 5.7, we show the taper profiles of 10 manufactured tapers, where it is evident that their dimensions are consistent similar, and the shapes of the up-down transitions exhibit uniform behavior. Furthermore, the diameter of the waist can be considered highly constant, although some fluctuations may be observed in specific tapers. This variability is attributed to external factors, such as strong air currents, which can affect the alignment of the bare fiber with plasma.
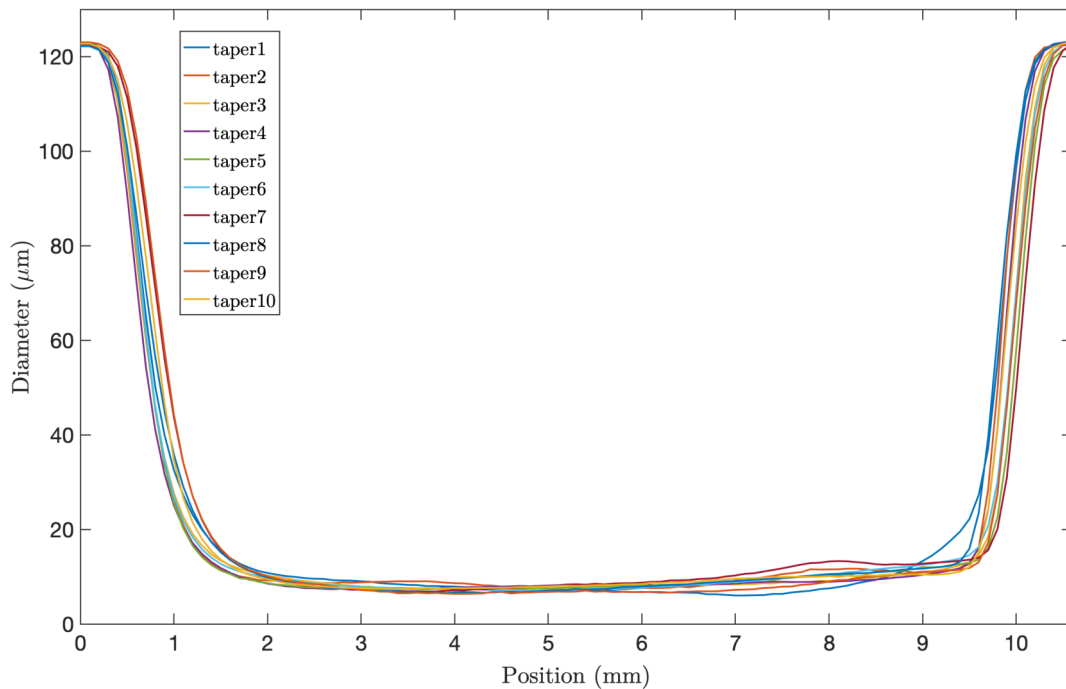
FIGURE 5.7: Taper profile of 10 tapers manufactured with 10 mm of pulling distance and 15 steps/s, achieving taper length (L)= 10 mm and waist diameter of 8 μm

The main curve between the 10 tapers reported is plotted in Figure 5.8 A, to analyze and obtain the experimental main taper profile for the taper with 10 mm of length and then compare with the theoretical taper profile (see Figure 5.8 B) using the Birks model described previously. This comparison allows us to estimate whether the taper is highly symmetric if the waist remains constant and the taper transitions are symmetric between them.
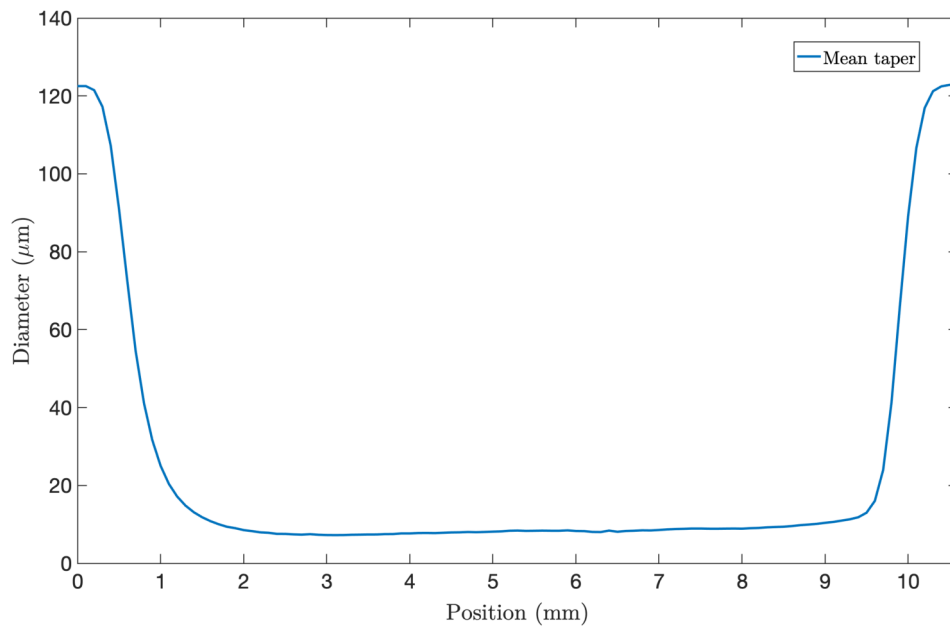
(A) Mean experimental taper profile of 10 tapers
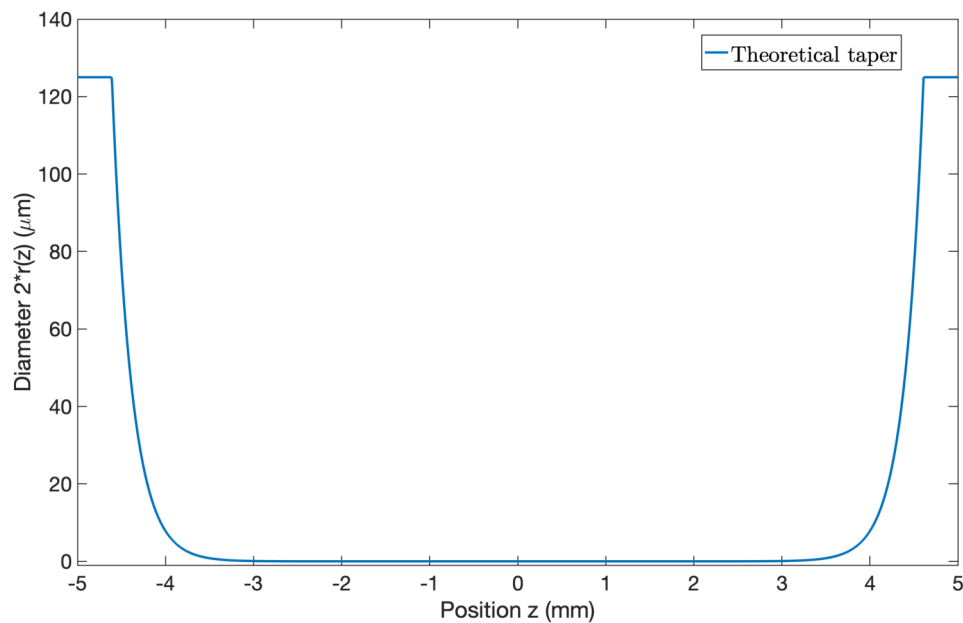
(B) Theoretical taper Profile using the Birks model

FIGURE 5.8: Theoretical and experimental taper profile

The standard deviation of these 10 samples is evaluated to verify the positive
and negative values obtained and compare them with the main profile curve. Figure
5.8 plots the mean curve, the standard deviation and the CV coefficient of variation.
This allows for the distinction of the taper profile's shape and the variations between
the data points in specific position.
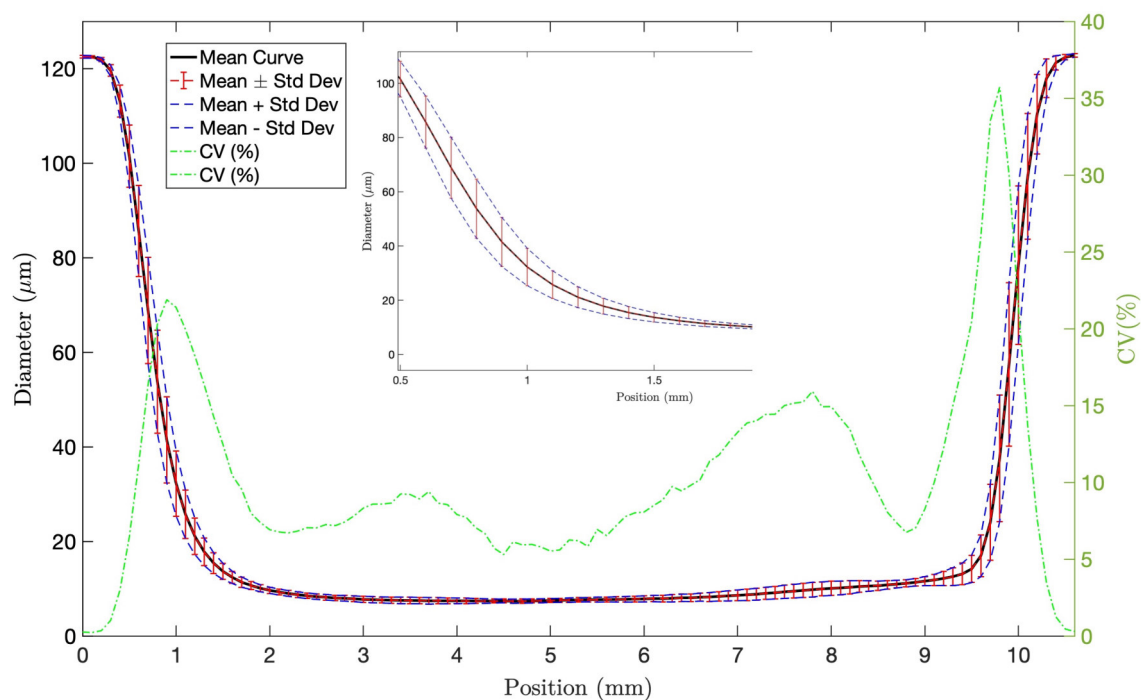
FIGURE 5.9: Mean curve, mean ± standard deviation and coefficient of vari-
ation The repeatability of the manufacturing process is evaluated by deriving
the main taper profile for the tapers and comparing the positive and negative
standard deviations relative to the central curve. The Coefficient of Variation
(CV) is then calculated as the ratio of the standard deviation to the mean,
representing repeatability between diameters at distinct positions.

This study reveals variations in the up-down transitions, as previously mentioned.
However, the dimensions of length, waist, and curvature are remarkably consistent.
Furthermore, a uniform waist diameter is achieved, demonstrating excellent tapered
construction performance with high repeatability. The level of coefficient of variation
(CV), showing only the variation 35%, indicates low variability and high precision
in the manufacturing process.

5.3 Light transmission

In order to determine the losses and the optical response, a tunable laser operating whithin the wavelength range of 1465 to 1599 nm and a Light wave multimeter were employed. Light transmission through the fiber was measured both before and after the pulling process. This facilitated the setting of spectral references for both the untapered fiber and the tapered fiber, as depicted in Figure 5.10 a). It is important to note that the specific shape of the taper at the input/output does not affect the light transmission spectra, as the spectra remain consistent regardless of the taper shape in this experimental setup.
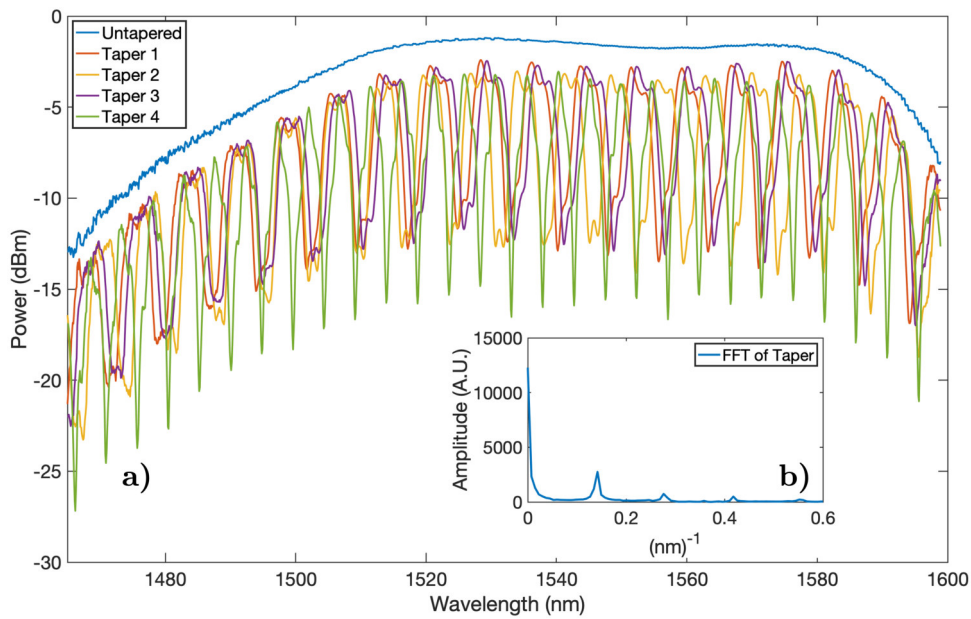
FIGURE 5.10: (a) Light transmission spectra of four 10-mm tapers with a diameter of 8 μm. The spectra show a Free Spectral Range (FSR) of 4.8 nm for the spectrum in green and 7.9 nm for the spectrum in red. (b) FFT of Taper 1, highlighting the fundamental mode and the excitation of higher-order modes.

The transmission of several tapers, characterized by the dimensions discussed earlier, was measured to estimate the typical optical response of the fabricated devices. Figure 5.9(a) shows the spectrum of four of these devices, demonstrating similar shape of the spectrum. However, by evaluating the FFT of each spectrum, it becomes evident that the modes involved are not identical, indicating slight variations between the devices. The visibility of the fringes ranges from 9 to 12 dBm, which is exceptional for amplitude optical response sensors. The average losses are less than 1.5 dB, which is considered low for these devices. In particular, the tapers exhibit an interference spectrum attributed to the excitation of higher-order modes, as observed in the Fast Fourier Transform (FFT) of the taper spectrum (see Figure 5.6(b)). At least one higher mode is discernible, creating multimode interference with the fundamental mode.

5.4 Manufacturing capabilities

The table below provides information on tapered fibers fabricated with lengths ranging from 2.5 mm to 15 mm. These fibers were manufactured at a pulling speed of 15 steps/s, with the taper length adjusted as necessary. For short tapers, such as the 2.5 mm ones, the typical curve observed shows very abrupt tapered transitions, reaching diameters of 15 μm. For tapers longer than 5 mm, a constant diameter is achieved, though some fluctuations are observed along the waist length. Despite this, the tapered transitions remain abrupt and measure 2 mm in length for all cases. The minimum waist diameter obtained was 6 μm in the taper with a length of 15 mm. This is attributed to the fact that as the rig exerts more pull, the fiber elongates more.

Taper Length (mm)	Waist length wL(mm)	Waist diameter (μm)	Reference
Taper 2.5 mm	1	15	Figure 5.11
Taper 5 mm	2	8	Figure 5.12
Taper 9 mm	6	7	Figure 5.13
Taper 11 mm	8	6	Figure 5.14
Taper 15 mm	11	6	Figure 5.15

TABLE 5.2: Dimensions measured of tapers ranging from 2.5 mm to 15 mm
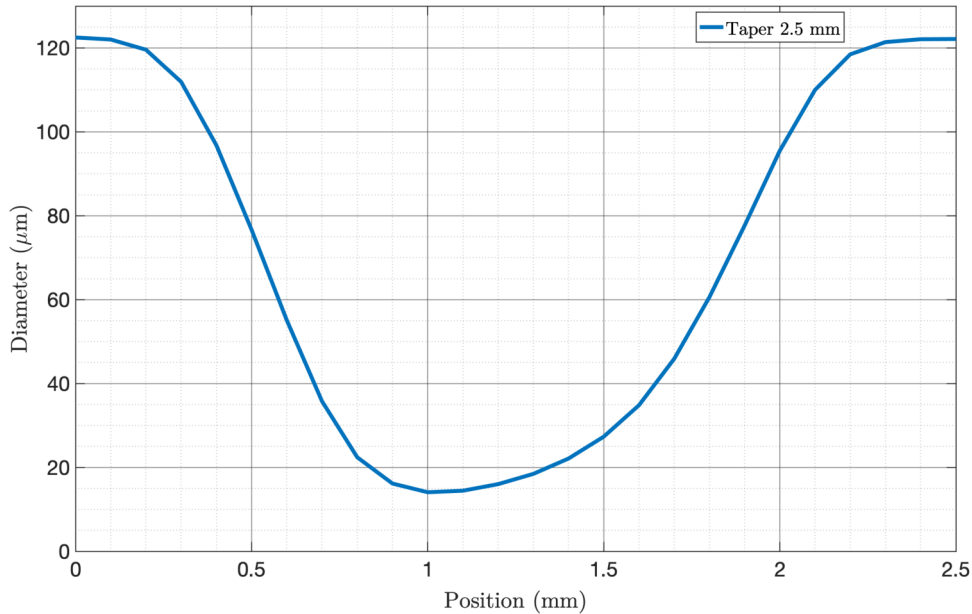
FIGURE 5.11: Taper L= 2.5 mm and waist=15 μ m
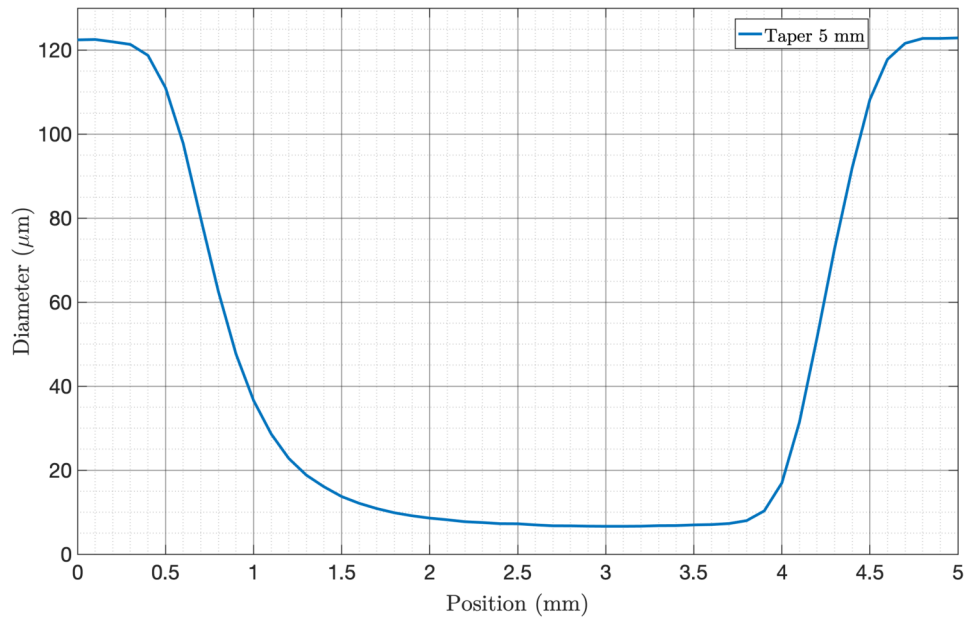
FIGURE 5.12: Taper L= 5 mm and waist=8 μ m
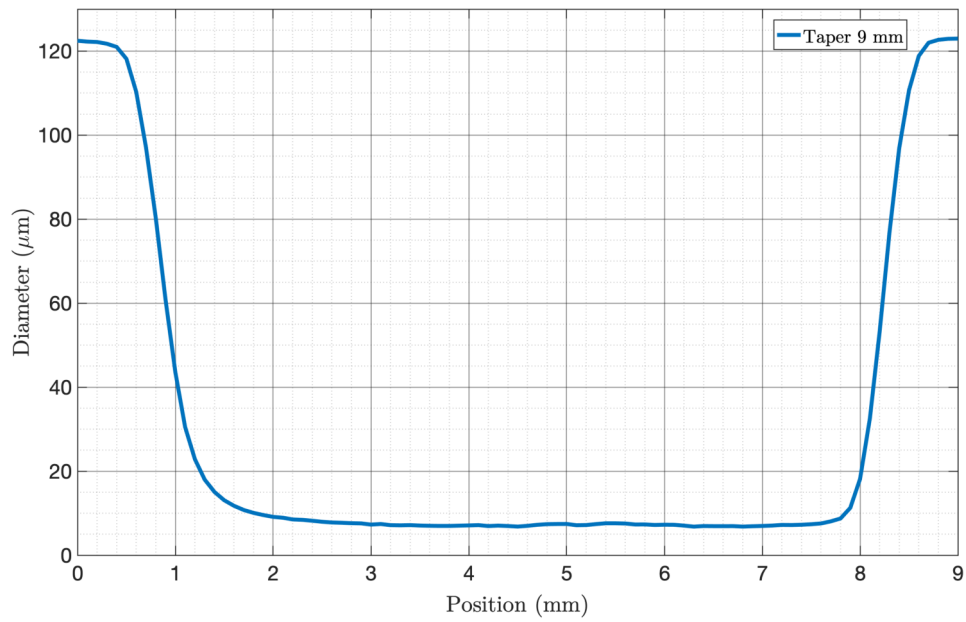
FIGURE 5.13: Taper L= 9 mm and waist=7 μ m
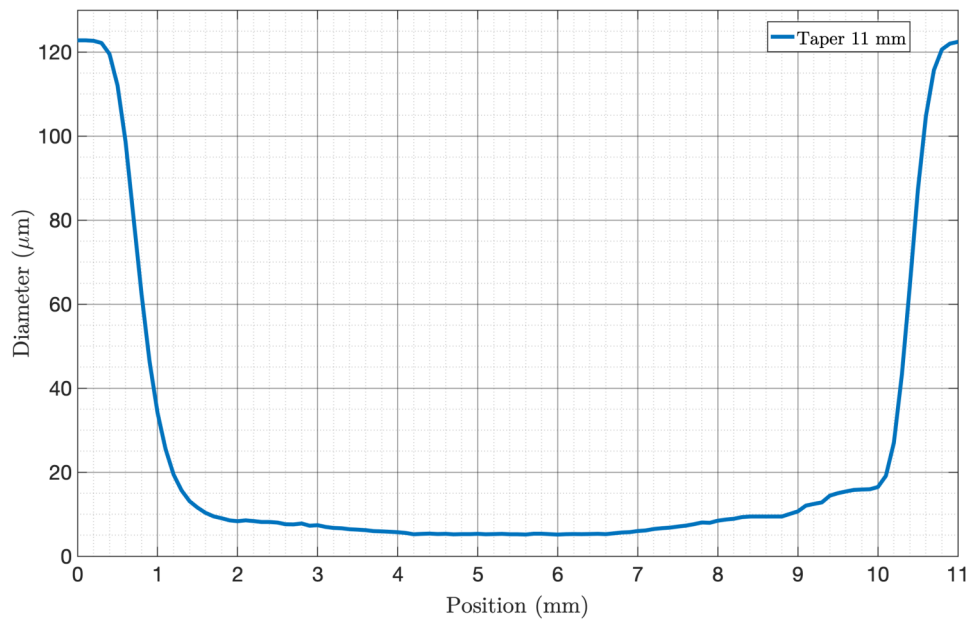
FIGURE 5.14: Taper L= 11 mm and waist=6 μ m
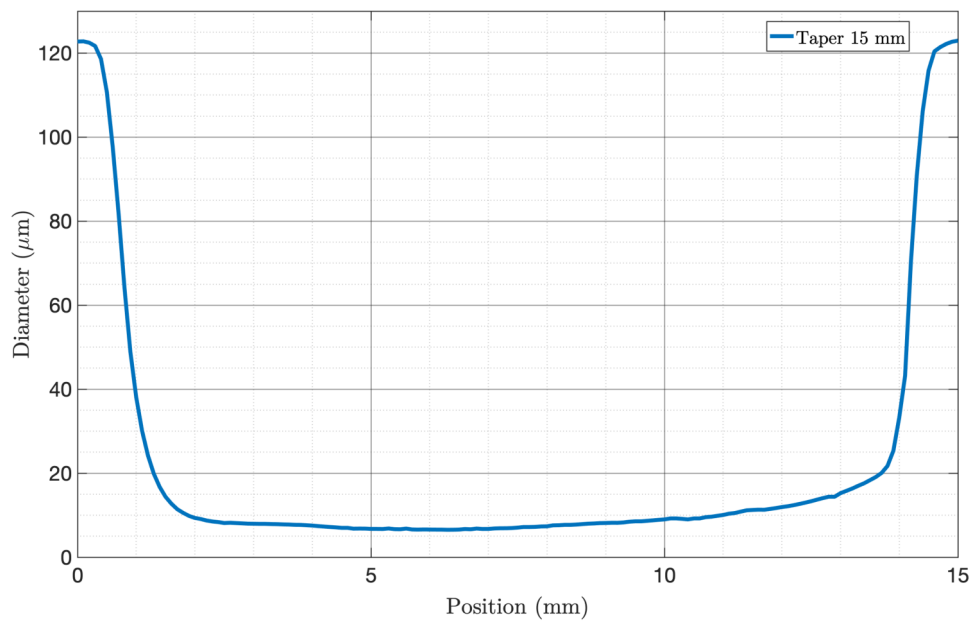
FIGURE 5.15: Taper L= 15 mm and waist=6 μ m

5.4.1   Light transmission properties of the tapers

The following table presents the light transmission properties of the tapered fibers evaluated in Section 5.4. To analyze the impact of higher modes on the total spectrum, we plot the Fast Fourier Transform (FFT). Moreover, this plot illustrates how distance between two adjacent peaks or valleys known as the Free Spectral Range (**FSR**) depends on the taper length, as described in the following equation [55]:

$$FSR \approx \frac{\lambda^2}{\Delta n \cdot wL} \tag{5.2}$$

Where *Deltan* is the refractive index difference of the fiber, wL is the waist length of the tapers and λ in this case is the central wavelength of the light source. Here, it is clear that the FSR strongly depends on the change in refractive indices as well as on the waist length. These two parameters are associated to the elongation of the tapered waist by pulling the fiber using the faster translation stage.

Taper Length (mm)	Insertion Losses (dB)	FSR nm	Fringes visibility (dB)	Reference
Taper 2.5 mm	1.37	-	-	Figure 5.16
Taper 5 mm	1.1	19.1	14.30	Figure 5.17
Taper 9 mm	6	7.6	12.83	Figure 5.18
Taper 11 mm	8	8	15.36	Figure 5.19
Taper 15 mm	11	3.9	11.78	Figure 5.20

TABLE 5.3: Light transmission properties of tapered structures with lengths ranging from 2.5 mm to 15 mm

The visibility of the fringes refers to the maximum amplitude of the fringes observed in each spectrum. In this context, a taper with ~14 dB visibility is considered exceptionally high for an amplitude-dependent sensor using a taper, according to the literature [56]. Additionally, by increasing the taper length, it is possible to modulate the number of fringes. This occurs because the fundamental mode and a higher-order mode interfere, creating an interference pattern. As the taper length increases, the frequency of the modes becomes higher, resulting in finer fringes. This allows for the selection of a narrower optical wavelength range, making it suitable for analysis with narrow-band light sources.

In the case of short tapers (<2.5 mm in length), waist length (wL) or changes in refractive index Δn result in the participation of many higher-order modes. This prevents the formation of a well-defined interference pattern. Further, to visualize any possible fringes, a broader optical source is required.
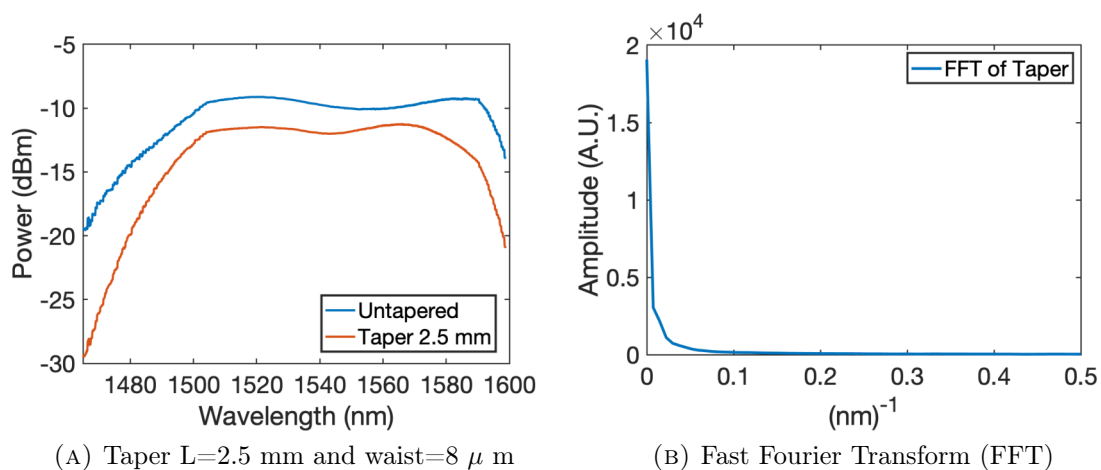
(A) Taper L=2.5 mm and waist=8 μ m

(B) Fast Fourier Transform (FFT)

FIGURE 5.16: Taper 2.5 mm

(A) Taper L= 5 mm and waist=8 μ m

(B) Fast Fourier Transform (FFT)

FIGURE 5.17: Taper 5 mm

(A) Taper L=9mm and waist=8 μ m

(B) Fast Fourier Transform (FFT)

FIGURE 5.18: Taper 9 mm

(A) Taper L=11mm and waist=8 μ m

(B) Fast Fourier Transform (FFT)

FIGURE 5.19: Taper 11 mm

(A) Taper L=15mm and waist=8 μ m

(B) Fast Fourier Transform (FFT)
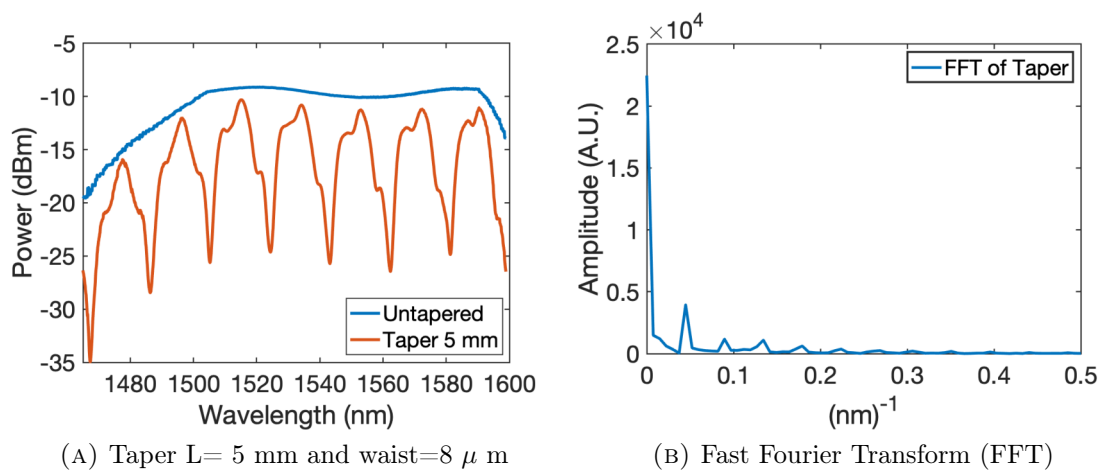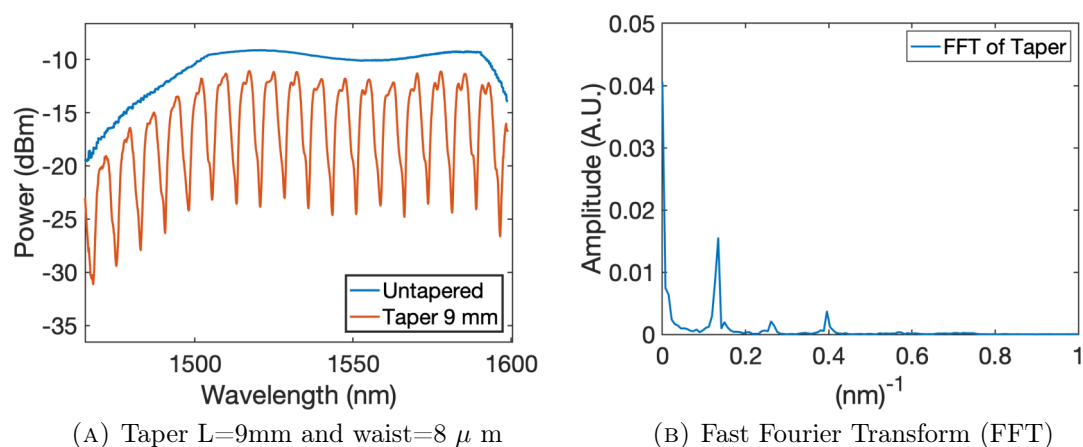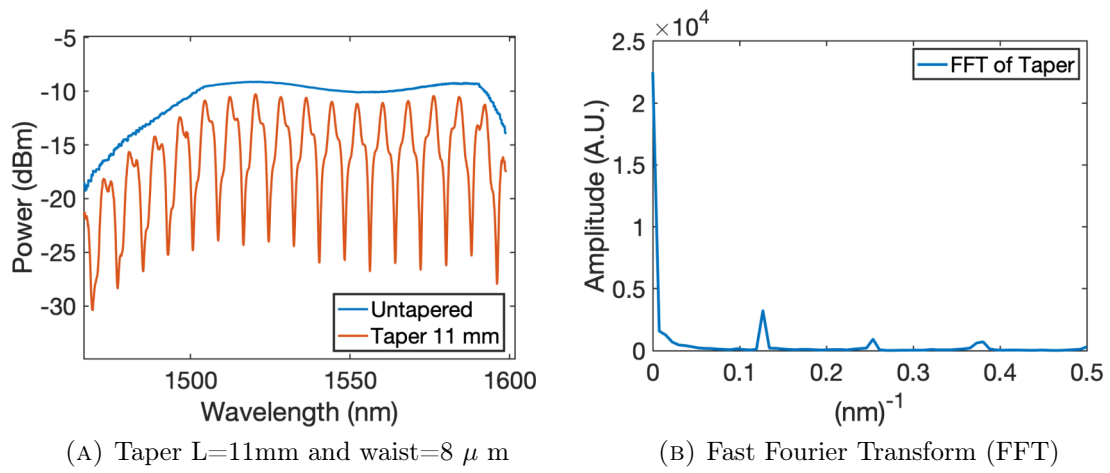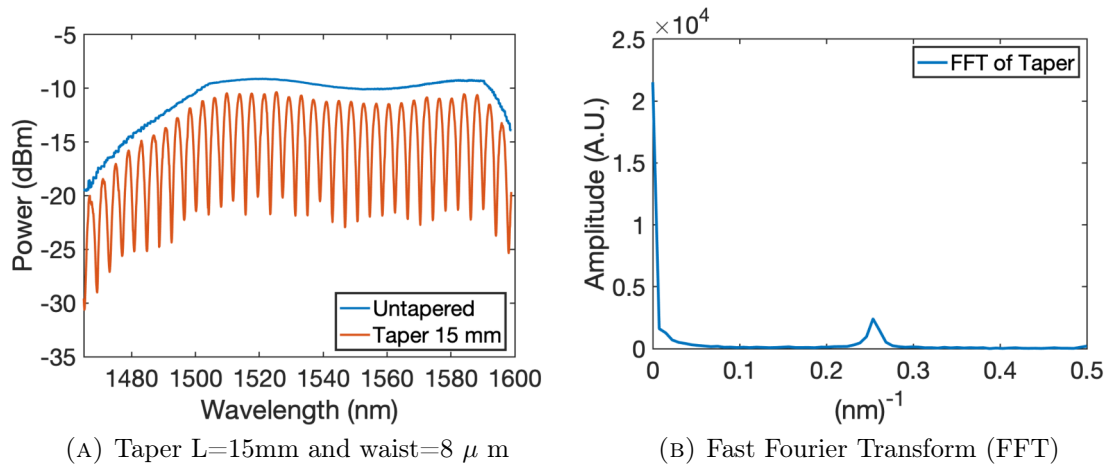
FIGURE 5.20: Taper 15 mm

Chapter 6

Results

This chapter describes the implementation of a tapered fiber to measure temperature through direct contact with a hot base plate, which was developed as an intrinsic temperature sensor. This study investigates the sensor's performance, focusing on its sensitivity and optical response. The results demonstrate the high potential of using the tapered fiber fabricated with the previously described plasma pulling rig. The experimental setup for temperature measurement and a theoretical analysis of the results is provided.

6.1 Taper as temperature sensor

The taper dimensions were 15 mm of taper length (L), 11 mm of waist length wL, and 8 μm waist diameter. The Mach-Zehnder interferometer cavity formed in the tapered region produce the interference patter of the light transmission spectrum due the interaction of at least the first fundamental mode and a higher order mode.

The study of this interference was conducted by assuming that there are only two modes interacting and creating the interference pattern. In the case of the untapered fiber region, the refractive indices of the core mode and the cladding mode are n_1 and n_2. Thus, the resultant intensity of the SMF fiber is given by [57]:

$$I_T = I_{co} + I_{cl} + 2\sqrt{I_{co}I_{cl}}cos\phi \tag{6.1}$$

where I_{co} and I_{cl} are the intensities of the fundamental mode in the core and the higher order more in the cladding, and ϕ is the phase difference between these two interfering modes. By considering only one higher-order mode excited, we take the waist length wL of the tapered region L as the interferometer length, as this is the most sensitive region of the sensor. Furthermore, the two interfering modes have the same interferometer length but different optical path lengths due to the difference in the core and cladding indices. This difference in the optical path is set by the refractive index difference Δn. Thus, the relative phase difference between the two interfering modes can be expressed as:

$$\phi = \frac{2\pi}{\lambda}\Delta n \cdot wL \tag{6.2}$$

Here, λ is the central wavelength of the light source. As the temperature changes, the refractive index of silica changes due to the thermal expansion effect, causing the length of the taper to increase, then the phase of the interferometric spectrum will consequently change. This temperature dependence of the refractive index is known as the thermo-optic effect [58]. If the $wL(t)$ and $\Delta n(T)$ represent the waist length and the difference in indices of the two modes at a certain temperature T, respectively. The equation 6.2 take form:

$$\phi = \frac{2\pi}{\lambda}\Delta n(T) \cdot wL(t) \tag{6.3}$$

By evaluating the equation 6.3 at room temperature conditions as the initial temperature $T = T_0$, we have $\Delta n = \Delta n(T_0)$ and $wL = wL(T_0)$. Then the thermo-optic coefficient of silica corresponds to $\eta = (\partial \Delta n/\partial T)_{T=T_0}$. The equations then are:

$$\Delta n(T) = \Delta n(T_0)[1 + \eta \cdot \Delta T] \tag{6.4}$$

and

$$wL(T) = wL(T_0)[1 + \alpha \cdot \Delta T] \tag{6.5}$$

where $\alpha = 5.5 \cdot 10^{-7} K^{-1}$ is the thermal expansion coefficient of the silica.

Equations 6.4 and 6.5 demonstrate that variations in temperature lead to changes in Δn and wL, consequently altering the phase of the intensity of the interferometry. Therefore, there will be a wavelength shift $\Delta\lambda$, in the interference spectrum caused by the thermo-optic coefficient η and the influence of the thermal expansion coefficient of the silica α. The expression for the relative wavelength shift, $\Delta\lambda/\lambda$, caused by a temperature change ΔT can be derived using equations. 6.4, 6.5 and substituting in 6.3 as:

$$\frac{\Delta\lambda}{\lambda} = -\frac{1}{\Delta n(T_0)wL(T)}(\frac{\partial \Delta n}{\partial T})_{T=T_0} \cdot wL(T_0)\Delta T \tag{6.6}$$

Using equation 6.6, we establish a direct relationship between the wavelength shift and the temperature variation relative to the initial temperature T_0. The change in temperature causes a shift in the pattern from its initial state, which can be quantified by expressing the peak wavelength as a function of temperature. Furthermore, by establishing this relation with the waist taper length wL, and the refractive index difference Δn, which are associated with the thermal expansion coefficient and the thermo-optic coefficient of silica, respectively, we can express the relative wavelength shift $\Delta\lambda/\lambda$ caused by a temperature change ΔT as follows [59]:

$$\frac{\Delta\lambda}{\lambda} \approx (\alpha + \eta)\Delta T \tag{6.7}$$

6.1.1 Experimental setup to measure temperature

The typical optical response of the tapered fiber, featuring a length of 15 mm, a waist length of 11 mm, and transitions of 2 mm length at both ends, is depicted in Figure 6.1. The normalized spectrum was derived by measuring the relative transmission of the taper, defined as the ratio of the light transmission spectra of the untapered fiber and the tapered fiber. The average insertion losses are less than 0.8 dB, and the fringe visibility is up to 10 dB.
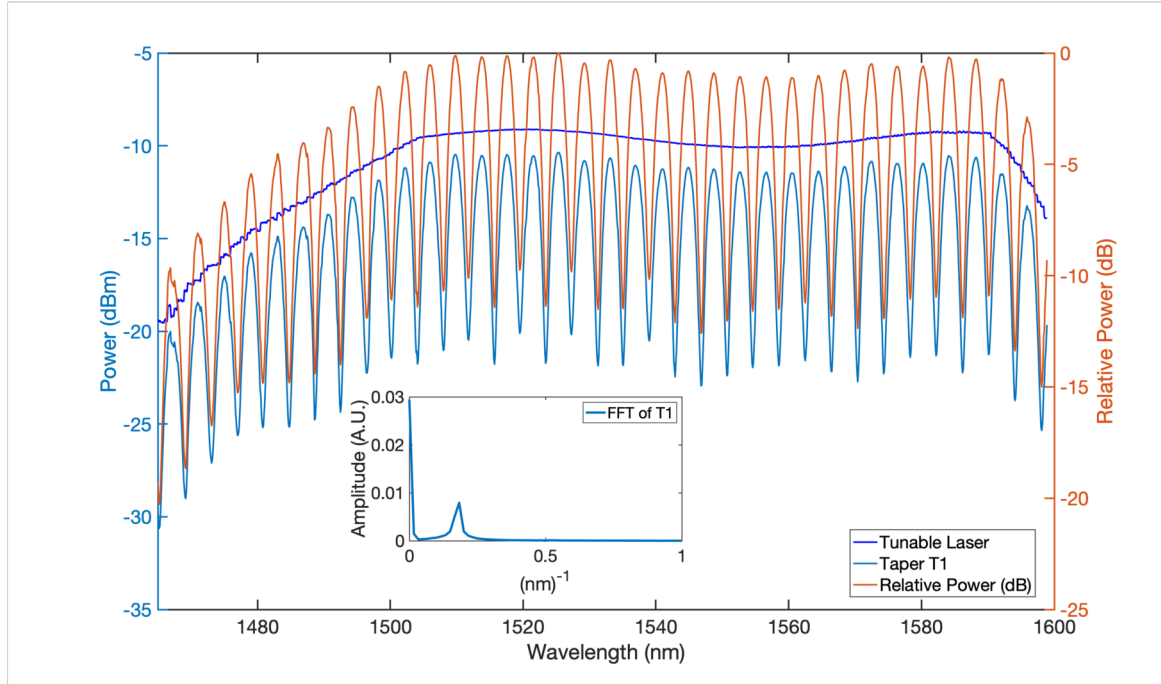
FIGURE 6.1: Typical spectral response of a 15 mm taper, highlighting the untapered spectrum referenced to the tunable laser, the spectrum of the 15 mm taper labeled as Taper T1, the normalized spectrum representing relative power and the FFT of the taper T1.

The fabricated sensor was placed on a stirring hot plate, specifically the Corning PC-420D, which offered a temperature ranged from room temperature 20 $°C$ to 550 $°C$. Once the oven reached 30 $°C$ as initial temperature, we allowed approximately 20 minutes for the temperature to stabilize before initiating the measurement process.

To measure light transmission, we utilized a tunable laser, specifically the HP 8168C, operating within a wavelength range of 1469 to 1599 nm, as the light source coupled into the system. The light transmitted from the fiber sensor output was detected using an HP 8153A lightwave multimeter. Spectra were recorded over a temperature range of 30 $°C$ to 140 $°C$, with increments of 10 $°C$.

(A) 1) Tunable laser and 2) Lightwave multimeter

(B) 3) Hot plate, 4) Polystyrene and 4) Optical fiber
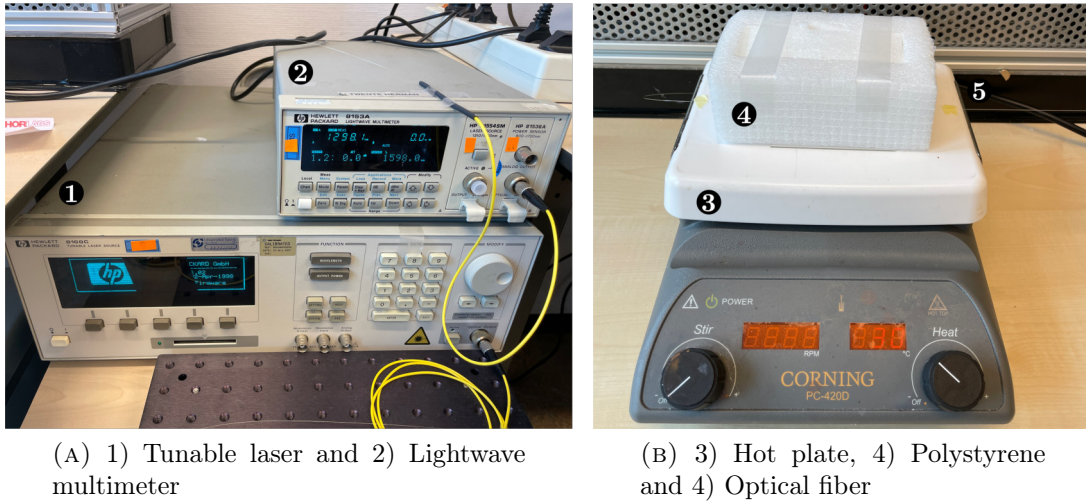
FIGURE 6.2: Experimental setup to measure the temperature

Figure 6.1 shows the experimental setup for temperature measurement. In (a), the setup includes the light source and the optical detector. In (b), the hot plate is shown where the taper is placed. The sensor is protected using expanded polystyrene to isolate it from external disturbances and maintain consistent environmental conditions around the sensor.
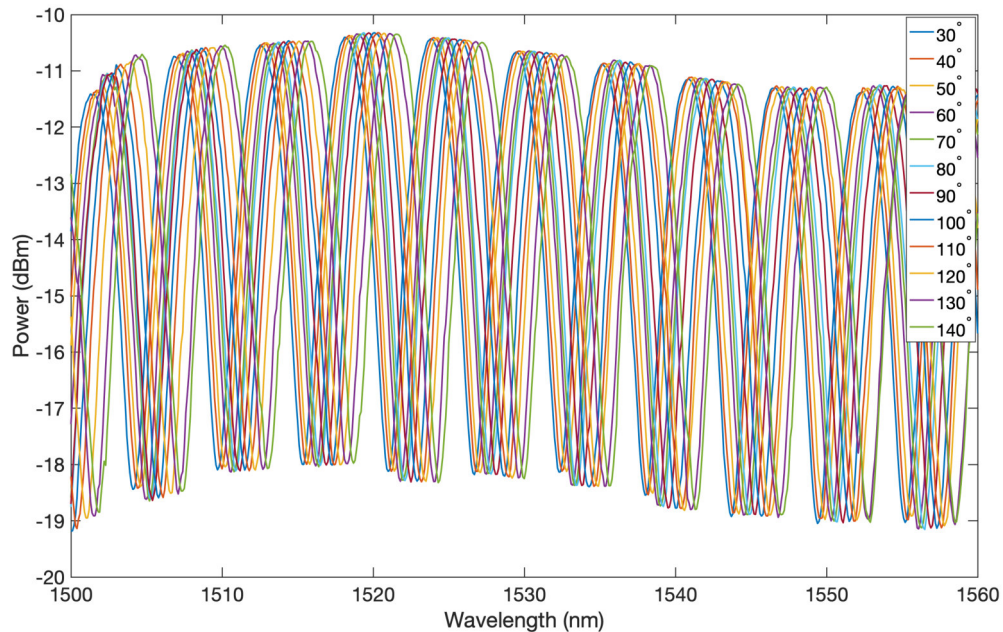
FIGURE 6.3: Spectral response of the taper by showing the untapered

To evaluate the distance between two adjacent peaks or valleys in the spectrum pattern, we calculate the free spectral range, defined as:

$$FSR \approx= \frac{\lambda^2}{\Delta n \cdot wL} \tag{6.8}$$

Hence, it is clear that the FSR strongly depends on the change in refractive indices as well as on the waist length. Changes in temperature affect the refractive indices of the core and the cladding (thermo-optic effect), as well as the fiber length (thermal expansion), thereby causing the interference fringes to shift accordingly.
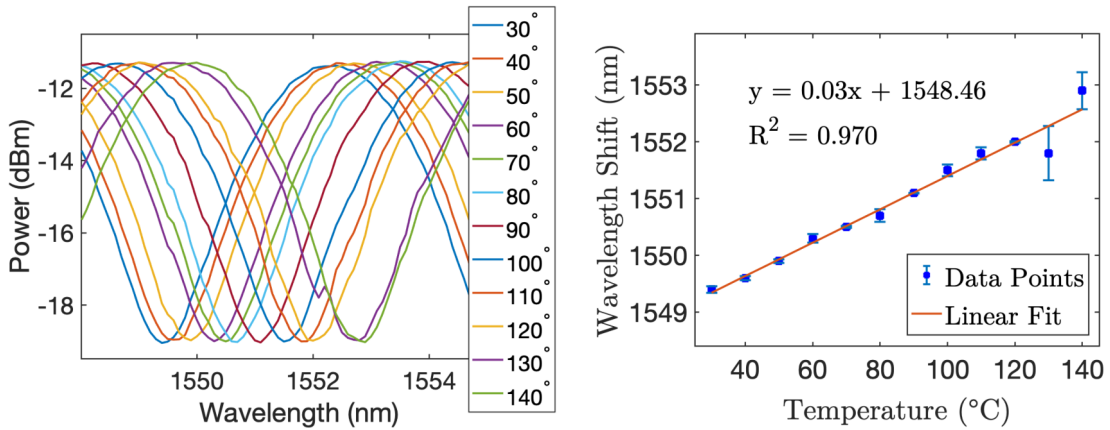
(A) The transmission spectra at different temperatures ranged from wavelengths from 1510 to 1556 nm

(B) Sensitivity plot of the sensor with a linear fit and error bars for the data, indicating a resolution of 200 pm/°C.

FIGURE 6.4: Transmission spectra across the wavelength range of 1542 to 1549 nm at different temperatures
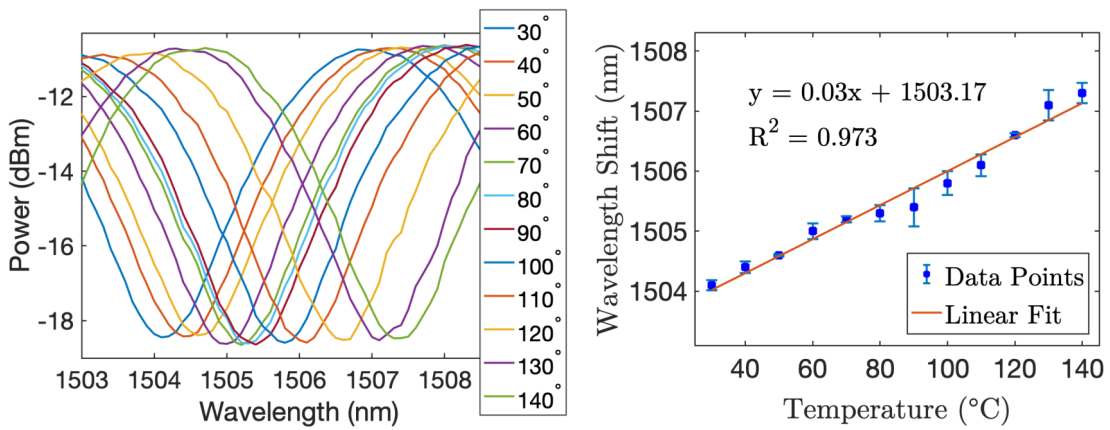
(A) Transmission spectra across the wavelength range of 1504 to 1507 nm at different temperatures

(B) Sensitivity plot of the sensor with a linear fit and error bars for the data, indicating a resolution of 200 pm/°C.

FIGURE 6.5: Transmission spectra for the sensor at different temperatures

6.1.2   Discussion

Figure 6.4 A and 6.4 C show the light transmission spectrum of the sensor at different temperatures. The heating applied by the base plate directly with the lower surface of the tapered fiber causes a shift in the spectrum towards longer wavelengths. This shift is attributed to the dominance of thermal expansion in the fiber, as described by Equation 6.7. In addition, the tapered section of the waist expands sufficiently to increase the thermal expansion coefficient (η), which is positive, overriding the negative thermo-optic coefficient (α), resulting in a positive wavelength shift.

The linear approximation presented in Figures 6.4 B and 6.4 D allows comparison of the error function of each data, establishing the linear behavior of the measurements. These deviations are represented by the error function, which shows slight variations with respect to the straight line. Furthermore, the calculation of the coefficient of determination (R^2) for both graphs indicates that the fitting is more than 97% of the variance in the wavelength shift due to temperature changes, predicting a similar response for higher temperatures.

The following table includes the performance characteristics of the sensor in two different wavelength ranges.

Sensor ID	Temperature ranges ($^\circ C$)	Wavelength ranges (nm)	FSR (nm)	Sensitivity (pm/$^\circ C$)
T1	30 to 140	1549.4 to 1552.9	4.354	200
T1	30 to 140	1504.1 to 1507.3	4.354	100

TABLE 6.1: Sensitivity of the temperature sensor T1 evaluated in different wavelength ranges

This experiment demonstrated the capability to apply these small-size and low-cost devices as phase optical sensors. The resolution expressed in picometers highlights these sensors as ultra-high-sensitivity devices if we compare them with electrical sensors.

Chapter 7

Conclusion

A cost-effective, computer controlled and reliable optical fiber tapering system was developed and validated. The key features of the system: readily available hardware, open-source software, and simple operation make it affordable and attractive for groups with an interest in applications based on tapered structures within a range of fields in science and engineering. The detailed description of the rig is essential for other research groups to reproduce it successfully. Mechanically strong (compared to tapered devices manufactured via other techniques) tapers with interference fringes (with 14 dB depth) ranging from 1465 nm to 1599 nm, were obtained.

The capabilities of this electromechanical system exhibit the possibility of manufacturing short tapers, measuring a few millimeters, to longer tapers of several centimeters. This is achieved by controlling the pulling distance with translation stages that have a total travel distance of 15 centimeters. Furthermore, the capability to customize the performance of the rig by modifying the programming code allows users to make concatenated tapers in the same optical fiber by controlling the gap distance between the tapers.

In addition, this thesis demonstrates that plasma can be utilized as a heating source for the fabrication of symmetrical taper structures with a high degree of reproducibility. Initially, there was uncertainty regarding the suitability of such a high-temperature source for silica glass processing because the temperatures generated by plasma are much higher than the boiling point of silica. Early tests revealed that the optical fiber could easily burn after just a few seconds of contact with the plasma. However, through precise control of the setup via programming and by adjusting the fabrication parameters and the movement of the translation stages, an optimal fabrication process was successfully achieved through experimental trials.

The design of the plasma pulling rig was inspired by existing rigs reported in the literature, with the interesting challenge of implementing plasma as a heater. Developing and tailoring the plasma control circuit was essential to manipulate it correctly and safely given the potential dangers of improper operation.

Furthermore, reviewing current heat and pull methods provided a basis for comparison in the fabrication process and allowed a detailed evaluation of the taper characteristics offered by each method. This review helped identify the most suitable method for our purposes. For instance, the brushing technique using plasma was immediately discarded because the movement of the plasma misaligned the fiber, and the inconsistent heating causes irregularities in the taper structure.

Going forward, once I managed to thin the fiber, I began characterizing the stretched fiber using the camera setup described in Chapter 4 to determine the types of structures that the rig could produce. Initially, these structures were non-symmetric and not reproducible when the theoretical taper profile was compared with the experimental results. Consequently, I conducted extensive production of tapered fibers to explore the fabrication settings and manual procedures for manipulating the fiber to obtain the most symmetrical taper profile possible.

Otherwise, the heat and pull technique, which involves moving the stages in the same direction, proved to be the most suitable method. This technique has been implemented using a ceramic microheater setup at the Optical Sciences Group of the University of Twente. As a consequence, it also proved highly convenient for plasma use. In this case, we can manufacture shorter tapers compared to the ceramic microheater because the ceramic microheater can only cover a hot section longer than 20 mm, while plasma can cover an exceedingly small hot section (around 1 mm). Nevertheless, by quickly transporting and simultaneously pulling, we were able to cover more section in the fiber and then reduce its dimensions with good symmetry.

Furthermore, I noticed that even if the stretched fibers were asymmetric, their mechanical robustness remained intact while manipulating them, contrary to that in my experience the tapers made using the flame brushing technique by the rig I operated at the Universidad de Guanajuato, resulted to be fragile and were difficult to remove from the stages. This mechanical robustness is attributed to the plasma source because it is considered a clean source because the elevated temperatures mostly burn the particles that can adhere to the glass surface of the fiber, the same as when using the flame brushing technique.

The literature review on single-mode tapered fibers and their applications was crucial in achieving the main goal of this work. This review enabled me to determine that the fabricated tapers are non-adiabatic and lossy. Despite this, I realized that they are highly attractive for many applications in the field of optical sensors. Although theory suggests that adiabatic tapers have the best quality due to negligible losses, the light transmission losses in the fabricated tapers are less than 1.0 dB. This low level of loss means that the output power can still be easily detected and used effectively as sensors. Additionally, the high robustness of these devices allows their implementation in various configurations, such as U-bent tapered sensors (see Figure 7.1), or for directly measuring the curvature angle by bending the taper.

(A) Bending the fiber   (B) Tapered region
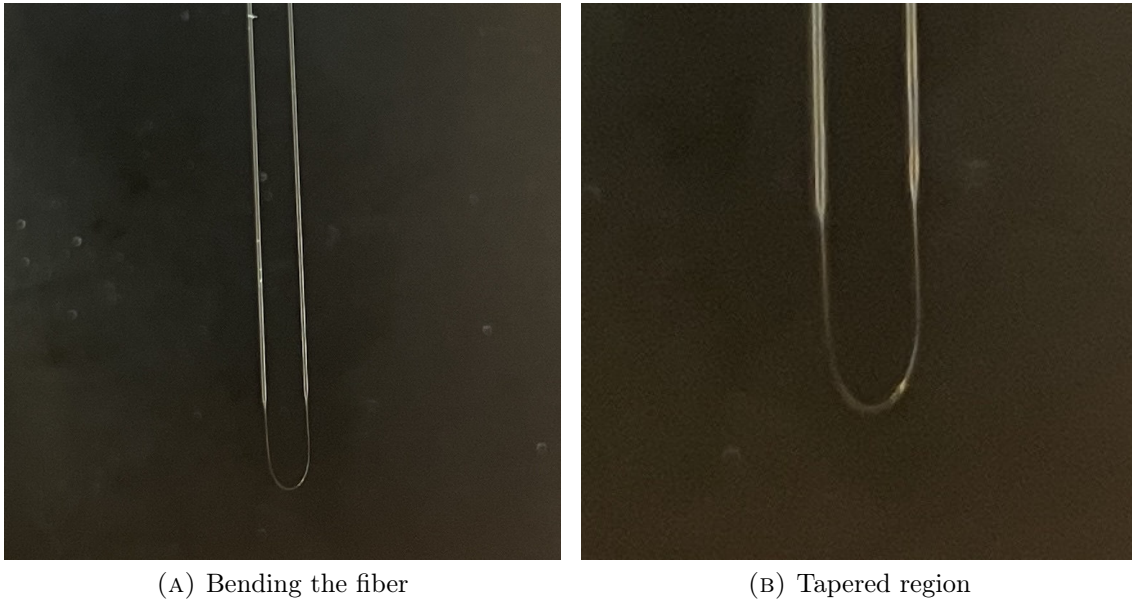
FIGURE 7.1: U-bent tapered fiber

The multimodal interference observed in these devices is notably attributed to the excitation of higher modes in the tapered section. Single-mode operation occurs under specific conditions related to the cutoff wavelength λ_c, V number, numerical aperture NA, and acceptance angle θ_a of the fiber. When a section of the fiber is stretched, these parameters change due to the smaller waist diameters. This results in a decrease in the V number and commonly produces a cladding mode known as the predominant higher mode.

The analysis of the Fast Fourier Transform (FFT) reveals that the excitation of multiple higher-order modes produces a modulated interference pattern. This pattern arises from the interaction between the higher-order modes and the fundamental mode, resulting in both constructive and destructive interference of the intensities of each mode involved.

However, it is more convenient to analyze the theory by considering only the fundamental mode and the next higher mode, as these are the most predominant in the interference effect. By manipulating the tapers, it becomes evident that, at some point, the higher modes represented in the FFT disappear. This may occur due to changes in the surrounding medium of the taper or to the stress applied when the taper shape is varied by manipulating the fiber. The intensity of these higher modes is transferred as insertion losses and then the spectrum looks smoother.

7.1   Future work

Full control engineering of important parameters such as the temperature gradient for the heating source, differential pulling, and taper geometry will be carried out in the next iteration of the tapering system presented in this work. Additionally, the possibility to modify system operations through programming code, improvements in the mechanical setup, and the incorporation of external hardware highly compatible with Arduino allows us to explore different configurations and settings.

This enables the fabrication of not only symmetric tapers but also asymmetric structures, which are suitable for several applications. The possibility of using diverse types of optical fibers, such as Photonic-crystal fiber (PCF), fiber Bragg grating (FBG), and multicore fiber (MCF), is very attractive for achieving even more sensitivity. Furthermore, the small size of the plasma and the high resolution of the translation stages enable precise adjustments. By applying plasma discharges to the fiber and translating it within a range of 200 micrometers (μm) to 1 millimeter (mm), while periodically controlling these perturbations, long grating periods can be effectively fabricated in optical fibers.

7.2   Publications

[1] L.F. Granados-Zambrano, J.P. Korterik, J.M. Estudillo-Ayala, R. Rojas Laguna, D. Jauregui-Vazquez, H.L. Offerhaus and J.A. Alvarez-Chavez, "Plasma-based Optical Fiber Tapering Rig", HardwareX. Under peer review.

Acronyms

ASE Amplified Spontaneous Emission. 1

EDFA Erbium-Doped Fiber Amplifier. 1

EW Evanescent Wave. 1

FBG Fiber Bragg Grating. 2

FFT Fast Fourier Transform. 16, 53

FSR Free Spectral Range. 53

LiDAR Light Detection and Ranging. 1

MCF multi-core Fiber. 2

OSA Optical Spectrum Analyzer. 17

PCF Photonic-crystal fiber. 2

SMF Single Mode Fiber. iii, 6

TIR Total Internal Reflection. 6

ZVS Zero-Voltage Switching. 31

List of Figures

List of Tables

Bibliography

[1] J R Ek-Ek, F Martinez-Pinon, J A Alvarez-Chavez, D E Ceballos-Herrera, R Sanchez-Lara, and H L Offerhaus. Fundamental mode intensity evolution in tapered optical fibres. *Laser Physics*, 30(12):126204, nov 2020. URL: https://dx.doi.org/10.1088/1555-6611/abbe1e, doi:10.1088/1555-6611/abbe1e.

[2] H. Ahmad, M.F. Salleh, M.K.A. Zaini, M.Z. Samion, and S.A. Reduan. Performance comparison of supercontinuum generation using various tapered fiber waist diameters with a mode-locked fiber laser. *Optik*, 272:170414, 2023. URL: https://www.sciencedirect.com/science/article/pii/S0030402622016722, doi:10.1016/j.ijleo.2022.170414.

[3] G. Salceda-Delgado, A. Martinez-Rios, M.A. Jimenez-Lizarraga, V.C. Rodríguez-Carreón, R. Selvas-Aguilar, J.M. Sierra-Hernandez, R. Rojas-Laguna, and J.I. López-Zenteno. Modifiable optical fiber tapered mach–zehnder interferometer for tune and switch optical fiber laser applications. *Optical Fiber Technology*, 70:102884, 2022. URL: https://www.sciencedirect.com/science/article/pii/S1068520022000670, doi:10.1016/j.yofte.2022.102884.

[4] Kwan Chi Kao. Dielectric-fibre surface waveguides for optical frequencies. 1999. URL: https://api.semanticscholar.org/CorpusID:229311796.

[5] P.M. Becker, A.A. Olsson, and J.R. Simpson. *Erbium-Doped Fiber Amplifiers: Fundamentals and Technology*. Optics and Photonics. Elsevier Science, 1999. URL: https://books.google.nl/books?id=uAOq75yt5CcC.

[6] M.A. Saifi. Optical amplifiers. In K.H. Jürgen Buschow, Robert W. Cahn, Merton C. Flemings, Bernhard Ilschner, Edward J. Kramer, Subhash Mahajan, and Patrick Veyssière, editors, *Encyclopedia of Materials: Science and Technology*, pages 6416–6423. Elsevier, Oxford, 2001. URL: https://www.sciencedirect.com/science/article/pii/B0080431526011359, doi:10.1016/B0-08-043152-6/01135-9.

[7] Md Shah Alam and Jared Oluoch. A survey of safe landing zone detection techniques for autonomous unmanned aerial vehicles (uavs). *Expert Systems with Applications*, 179:115091, 2021. URL: https://www.sciencedirect.com/science/article/pii/S0957417421005327, doi:10.1016/j.eswa.2021.115091.

[8] David J. Monk and David R. Walt. Optical fiber-based biosensors. *Analytical and Bioanalytical Chemistry*, 379(7-8):931–945, 2004. doi:10.1007/s00216-004-2650-x.

[9] Martin Kyselák, Karel Slavicek, David Grenar, Marek Bohrn, and Jiri Vavra. Fiber optic polarization temperature sensor for biomedical and military security systems. In Brian M. Cullum, Douglas Kiehl, and Eric S. McLamore, editors, *Smart Biomedical and Physiological Sensor Technology XIX*, volume 12123, page 121230A. International Society for Optics and Photonics, SPIE, 2022. doi:10.1117/12.2618911.

[10] Bakr Ahmed Taha, Norazida Ali, Nurfarhana Mohamad Sapiee, Mahmoud Muhanad Fadhel, Ros Maria Mat Yeh, Nur Nadia Bachok, Yousif Al Mashhadany, and Norhana Arsad. Comprehensive review tapered optical fiber configurations for sensing application: Trend and challenges. *Biosensors*, 11(8), 2021. URL: https://www.mdpi.com/2079-6374/11/8/253, doi:10.3390/bios11080253.

[11] María-Cruz Navarrete, Natalia Díaz-Herrera, Agustín González-Cano, and Óscar Esteban. Surface plasmon resonance in the visible region in sensors based on tapered optical fibers. *Sensors and Actuators B: Chemical*, 190:881–885, 2014. URL: https://www.sciencedirect.com/science/article/pii/S0925400513011076, doi:10.1016/j.snb.2013.09.066.

[12] Libo Yuan, Zhihai Liu, Jun Yang, and Chunying Guan. Twin-core fiber optical tweezers. *Opt. Express*, 16(7):4559–4566, Mar 2008. URL: https://opg.optica.org/oe/abstract.cfm?URI=oe-16-7-4559, doi:10.1364/OE.16.004559.

[13] Allan W. Snyder and John D. Love. *Fundamental properties of modes*, pages 208–237. Springer US, Boston, MA, 1983. doi:10.1007/978-1-4613-2813-1_3.

[14] P. Belanger. *Optical Fiber Theory: A Supplement To Applied Electromagnetism*. Series In Optics And Photonics. World Scientific Publishing Company, 1993. URL: https://books.google.nl/books?id=U5dIDQAAQBAJ.

[15] Lucian Bojor. Fiber modes. https://www.mathworks.com/matlabcentral/fileexchange/9126-fiber-modes, February 15 2024. MATLAB Central File Exchange.

[16] S.J. M. *Optical Fiber Communications: Principles and Practice*. Pearson Education, 2009. URL: https://books.google.nl/books?id=ok0XX-3MgMoC.

[17] T.A. Birks and Y.W. Li. The shape of fiber tapers. *Lightwave Technology, Journal of*, 10(4):432 –438, April 1992. doi:10.1109/50.134196.

[18] J.D. Love. Tapered single-mode fibres and devices. part 1: Adiabaticity criteria. *IEE Proceedings J (Optoelectronics)*, 138:343–354(11), October 1991. URL: https://digital-library.theiet.org/content/journals/10.1049/ip-j.1991.0060.

[19] Richard J. Black, Suzanne Lacroix, François Gonthier, and John D. Love. Tapered single-mode fibres and devices. ii. experimental and theoretical quantification. 1991. URL: https://api.semanticscholar.org/CorpusID:135698329.

[20] S.W. Harun, K.S. Lim, C.K. Tio, K. Dimyati, and H. Ahmad. Theoretical analysis and fabrication of tapered fiber. *Optik*, 124(6):538–543, 2013. URL: https://www.sciencedirect.com/science/article/pii/S0030402612000654, doi:10.1016/j.ijleo.2011.12.054.

[21] Ryutaro Nagai and Takao Aoki. Ultra-low-loss tapered optical fibers with minimal lengths. *Opt. Express*, 22(23):28427–28436, Nov 2014. URL: https://opg.optica.org/oe/abstract.cfm?URI=oe-22-23-28427, doi:10.1364/OE.22.028427.

[22] Ajoy Ghatak and K. Thyagarajan. *An Introduction to Fiber Optics*. Cambridge University Press, 1998.

[23] Saeed Khan, Sonia M. Buckley, Jeff Chiles, Richard P. Mirin, Sae Woo Nam, and Jeffrey M. Shainline. Low-loss, high-bandwidth fiber-to-chip coupling using capped adiabatic tapered fibers. *APL Photonics*, 5(5):056101, 05 2020. arXiv:https://pubs.aip.org/aip/app/article-pdf/doi/10.1063/1.5145105/14569856/056101_1_online.pdf, doi:10.1063/1.5145105.

[24] Anatol Khilo, Miloš A. Popović, Mohammad Araghchini, and Franz X. Kärtner. Efficient planar fiber-to-chip coupler based on two-stage adiabatic evolution. *Opt. Express*, 18(15):15790–15806, Jul 2010. URL: https://opg.optica.org/oe/abstract.cfm?URI=oe-18-15-15790, doi:10.1364/OE.18.015790.

[25] H. Latifi, M. I. Zibaii, S. M. Hosseini, et al. Nonadiabatic tapered optical fiber for biosensor applications. *Photonic Sensors*, 2:340–356, 2012. doi:10.1007/s13320-012-0086-z.

[26] M. A. Quintela, A. Quintela, N. Becue, J. M. Lázaro, F. Anabitarte, and J. M. Lopez-Higuera. Tunable fiber laser using concatenated non-adiabatic single-mode fiber tapers. In David Sampson, Stephen Collins, Kyunghwan Oh, and Ryozo Yamauchi, editors, *19th International Conference on Optical Fibre Sensors*, volume 7004, page 700453. International Society for Optics and Photonics, SPIE, 2008. doi:10.1117/12.786184.

[27] Amnon Yariv and Pochi Yeh. *Photonics: Optical Electronics in Modern Communications*. Oxford University Press, 2007.

[28] B.D. Gupta. *Fiber Optic Sensors: Principles and Applications*. New India Publishing Agency, 2006. URL: https://books.google.nl/books?id=3fmkOUvirOMC.

[29] Gilberto Brambilla. Optical fibre nanotaper sensors. *Optical Fiber Technology*, 16(6):331–342, 2010. Special Fiber Structures and their Applications. URL: https://www.sciencedirect.com/science/article/pii/S1068520010000805, doi:10.1016/j.yofte.2010.08.009.

[30] Carlos A. J. Gouveia, Jose M. Baptista, and Pedro A.S. Jorge. Refractometric optical fiber platforms for label free sensing. In Sulaiman Wadi Harun and Hamzah Arof, editors, *Current Developments in Optical Fiber Technology*, chapter 13. IntechOpen, Rijeka, 2013. doi:10.5772/55376.

[31] A Descoeudres, Ch Hollenstein, R Demellayer, and G Wälder. Optical emission spectroscopy of electrical discharge machining plasma. *Journal of Physics D: Applied Physics*, 37(6):875, feb 2004. URL: `https://dx.doi.org/10.1088/0022-3727/37/6/012`, doi:10.1088/0022-3727/37/6/012.

[32] Annemie Bogaerts, Erik Neyts, Renaat Gijbels, and Joost van der Mullen. Gas discharge plasmas and their applications. *Spectrochimica Acta Part B: Atomic Spectroscopy*, 57(4):609–658, 2002. URL: `https://www.sciencedirect.com/science/article/pii/S0584854701004062`, doi:10.1016/S0584-8547(01)00406-2.

[33] Donghwa Lee, Kwang Jo Lee, Jin-Hun Kim, Kyungdeuk Park, Dongjin Lee, Yoon-Ho Kim, and Heedeuk Shin. Fabrication method for ultralong optical micro/nano-fibers. *Current Applied Physics*, 19(12):1334–1337, 2019. URL: `https://www.sciencedirect.com/science/article/pii/S1567173919302160`, doi:10.1016/j.cap.2019.08.018.

[34] Jean C. Graf, Silvio A. Teston, Pedro V. de Barba, Jeferson Dallmann, Jose A. S. Lima, José A. S. Lima, Hypolito J. Kalinowski, and Aleksander S. Paterno. Fiber taper rig using a simplified heat source and the flame-brush technique. In *2009 SBMO/IEEE MTT-S International Microwave and Optoelectronics Conference (IMOC)*, pages 621–624, 2009. doi:10.1109/IMOC.2009.5427507.

[35] Jonathan M. Ward, Danny G. O'Shea, Brian J. Shortt, Michael J. Morrissey, Kieran Deasy, and Síle G. Nic Chormaic. Heat-and-pull rig for fiber taper fabrication. *Review of Scientific Instruments*, 77(8):083105, 08 2006. arXiv:https://pubs.aip.org/aip/rsi/article-pdf/doi/10.1063/1.2239033/13530264/083105_1_online.pdf, doi:10.1063/1.2239033.

[36] Fabien Bayle and Jean-Pierre Meunier. Efficient fabrication of fused-fiber biconical taper structures by a scanned co2 laser beam technique. *Appl. Opt.*, 44(30):6402–6411, Oct 2005. URL: `https://opg.optica.org/ao/abstract.cfm?URI=ao-44-30-6402`, doi:10.1364/AO.44.006402.

[37] Gongwen Zhu. High efficiency mode field adapters fabricated with CO2 laser splicer. In Alexei L. Glebov and Paul O. Leisher, editors, *Components and Packaging for Laser Systems V*, volume 10899, page 108991A. International Society for Optics and Photonics, SPIE, 2019. doi:10.1117/12.2507509.

[38] Lu Ding, Cherif Belacel, Sara Ducci, Giuseppe Leo, and Ivan Favero. Ultralow loss single-mode silica tapers manufactured by a microheater. *Appl. Opt.*, 49(13):2441–2445, May 2010. URL: `https://opg.optica.org/ao/abstract.cfm?URI=ao-49-13-2441`, doi:10.1364/AO.49.002441.

[39] Mateusz Lakomski, Bartlomiej Guzowski, and Arkadiusz Wozniak. Fabrication of ultra-long tapered optical fibers. *Microelectronic Engineering*, 221:111193, 2020. URL: https://www.sciencedirect.com/science/article/pii/S0167931719303491, doi:10.1016/j.mee.2019.111193.

[40] Bartlomiej Guzowski, Mateusz Łakomski, Krzysztof Peczek, and Mateusz Melka. Evaluation of the tapered optical fiber geometry repeatability in arc-discharge method fabrication. 2020. URL: https://ssrn.com/abstract=4605479, doi:10.2139/ssrn.4605479.

[41] R. Garcia-Fernandez, W. Alt, F. Bruse, et al. Optical nanofibers and spectroscopy. *Appl. Phys. B*, 105(3):3, 2011. doi:10.1007/s00340-011-4730-x.

[42] G Brambilla. Optical fibre nanowires and microwires: a review. *Journal of Optics*, 12(4):043001, mar 2010. URL: https://dx.doi.org/10.1088/2040-8978/12/4/043001, doi:10.1088/2040-8978/12/4/043001.

[43] Pengfei Wang, Lin Bo, Yuliya Semenova, Gerald Farrell, and Gilberto Brambilla. Optical microfibre based photonic components and their applications in label-free biosensing. *Biosensors*, 5(3):471–499, 2015. doi:10.3390/bios5030471.

[44] Yoshiaki Takeuchi, Mamoru Hirayama, Shin Sumida, and Osamu Kobayashi. Characteristics of ceramic microheater for fiber coupler fabrication. *Japanese Journal of Applied Physics*, 37(6S):3665, jun 1998. URL: https://dx.doi.org/10.1143/JJAP.37.3665, doi:10.1143/JJAP.37.3665.

[45] N Hidayat, M S Aziz, G Krishnan, A R Johari, H Nur, A Taufiq, N Mufti, R R Mukti, and H Bakhtiar. Tapered optical fibers using co2 laser and their sensing performances. *Journal of Physics: Conference Series*, 2432(1):012013, feb 2023. URL: https://dx.doi.org/10.1088/1742-6596/2432/1/012013, doi:10.1088/1742-6596/2432/1/012013.

[46] Jonathan Ward, Danny O'Shea, Brian Shortt, Michael Morrissey, Kieran Deasy, and Síle Nic Chormaic. Heat-and-pull rig for fiber taper fabrication. *Review of Scientific Instruments*, 77, 05 2006. doi:10.1063/1.2239033.

[47] A.J.C. Grellier, N.K. Zayer, and C.N. Pannell. Heat transfer modelling in co2 laser processing of optical fibres. *Optics Communications*, 152(4):324–328, 1998. URL: https://www.sciencedirect.com/science/article/pii/S0030401898001643, doi:10.1016/S0030-4018(98)00164-3.

[48] Chen Chen, Song Gao, Liang Chen, and Xiaoyi Bao. Distributed high temperature monitoring of smf under electrical arc discharges based on ofdr. *Sensors*, 20(22), 2020. URL: https://www.mdpi.com/1424-8220/20/22/6407, doi:10.3390/s20226407.

[49] Peng Xiao, Zhen Sun, Yan Huang, Wenfu Lin, Yuchen Ge, Ruitao Xiao, Kaqiang Li, Zhenru Li, Hanglin Lu, Mingjin Yang, Lili Liang, Li-Peng Sun, Yang Ran, Jie Li, and Bai-Ou Guan. Development of an optical microfiber immunosensor for prostate specific antigen analysis using

a high-order-diffraction long period grating. *Opt. Express*, 28(11):15783–15793, May 2020. URL: https://opg.optica.org/oe/abstract.cfm?URI=oe-28-11-15783, doi:10.1364/OE.391889.

[50] Hamidreza Karimi-Alavijeh, Alireza Taslimi, Mohammad Hassan Maghsoudian, Mohammad Hosein Poorghadiri, and Mohammad Kazemzadeh. Fabrication of low-loss adiabatic optical microfibers using an attainable arc-discharge fiber tapering setup. *Optics Communications*, 522:128669, 2022. URL: https://www.sciencedirect.com/science/article/pii/S0030401822004394, doi:10.1016/j.optcom.2022.128669.

[51] Benedikt D Hauer, Philip H Kim, C Doolin, and et al. On-chip cavity optomechanical coupling. *EPJ Techn Instrum*, 1(1):4, 2014. doi:10.1140/epjti4.

[52] Kazimierz Albinski, Karol Musiol, Adam Miernikiewicz, Stefan Labuz, and Marek Malota. The temperature of a plasma used in electrical discharge machining. *Plasma Sources Science and Technology*, 5(4):736, nov 1996. URL: https://dx.doi.org/10.1088/0963-0252/5/4/015, doi:10.1088/0963-0252/5/4/015.

[53] R. Schmitt. *Electromagnetics Explained: A Handbook for Wireless/ RF, EMC, and High-Speed Electronics*. EDN Series for Design Engineers. Elsevier Science, 2002. URL: https://books.google.nl/books?id=7gJ4RocvEskC.

[54] G. Fuller and J.D. Tarwater. *Analytic Geometry*. Addison-Wesley, 1992. URL: https://books.google.nl/books?id=cZbuPwAACAAJ.

[55] LV Nguyen, D Hwang, S Moon, DS Moon, and Y Chung. High temperature fiber sensor with high sensitivity based on core diameter mismatch. *Optics Express*, 16(15):11369–11375, 2008. doi:10.1364/oe.16.011369.

[56] Zhipeng Yu, Long Jin, Lipeng Sun, Jie Li, Yang Ran, and Bai-Ou Guan. Highly sensitive fiber taper interferometric hydrogen sensors. *IEEE Photonics Journal*, 8(1):1–9, 2016. doi:10.1109/JPHOT.2015.2507369.

[57] T. Yadav, M. Mustapa, Muhammad Hafiz Abu Bakar, and Mohd Adzir Mahdi. Study of single mode tapered fiber-optic interferometer of different waist diameters and its application as a temperature sensor. *Journal of the European Optical Society: Rapid Publications*, 9, 07 2014. doi:10.2971/jeos.2014.14024.

[58] Eric Numkam Fokoua, Marco N. Petrovich, Tom Bradley, Francesco Poletti, David J. Richardson, and Radan Slavík. How to make the propagation time through an optical fiber fully insensitive to temperature variations. *Optica*, 4(6):659–668, Jun 2017. URL: https://opg.optica.org/optica/abstract.cfm?URI=optica-4-6-659, doi:10.1364/OPTICA.4.000659.

[59] Enbang Li, Xiaolin Wang, and Chao Zhang. Fiber-optic temperature sensor based on interference of selective higher-order modes. *Applied Physics Letters*, 89:091119–091119, 08 2006. doi:10.1063/1.2344835.

Appendix A

Building instructions

The construction process of the plasma pulling rig consists of three procedures: the construction of the motor control module, the construction of the ZVS plasma Module, and the assembly of the mechanical setup.

A.1 Construction of the motor control module

In Figure A.2, we present a visual schematic that shows the electrical components and the wiring connections. Additionally, Figure A.3 provides the circuit diagram, with a detailed view of pin interconnections. The assembly instructions of the motor control module are described in the following procedure:

1. Connect the AC connectors positive and negative pins to the inputs of the switch.

2. Link the output pins of the switch to the AC inputs of the XP Power Supply.

3. Establish a common ground connection as indicated by the black wire in the diagram. This step is crucial for the proper operation of the electrical circuit. Additionally, ensure that the aluminum enclosure and the optical table are also connected to the common ground.

4. Connect the power from the Microstep Driver to the 12V output of the XP Power Supply, represented by the red wire.

5. Set the micro step via the DIP switch of the Microstep Driver, see Figure 3.

The table below shows the ON/OFF configuration of the DIP switch, where the step angle setting for the motors is optimized at 0.225 degrees.

This configuration corresponds to 1600 pulses/revolution and an operational current of 2.5 A. Besides, for the linear rail track, each revolution corresponds to a linear movement of 4 mm.

$$1600 \ steps = 1rev/s = 4 \ mm \tag{A.1}$$

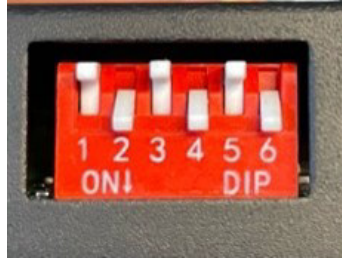FIGURE A.1: Configuration of the DIP switch of the Microstep Driver

SW1	SW2	SW3	SW4	SW5	SW6
OFF	ON	OFF	ON	OFF	0N

TABLE A.1: DIP switch configuration

Thus for 400 steps the travel distance correspond to 1 mm

$$400 \ steps = 1 \ mm \tag{A.2}$$

As previously mentioned, both translation stages are moving to the right. Notably, the right stage travels at a speed and distance 35 times greater than the left stage. The lowest stage does not influence the determination of the taper length. This linear movement of the faster stages is represented by the following equation:

$$\Delta D \ [mm] = 36 \cdot x \cdot D \tag{A.3}$$

Where D represents the travel distance (1 mm per 400 steps), x denotes the number of steps, and AD represents the cumulative distance in millimeters.

6. Make the interconnections of the pins with the same label. Note that the COM2 and N02 pins of the relay control the on and off functions of the plasma module.
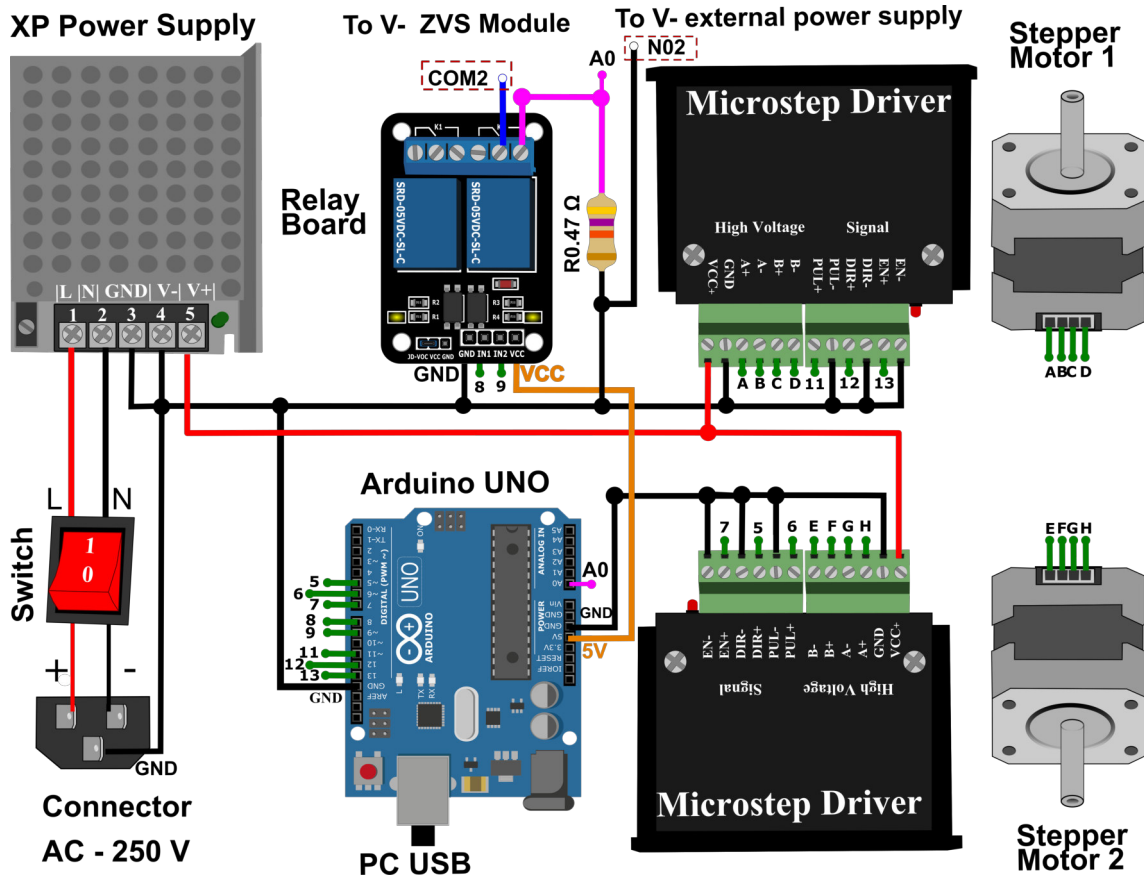
FIGURE A.2: Motor control wiring diagram using Arduino Uno
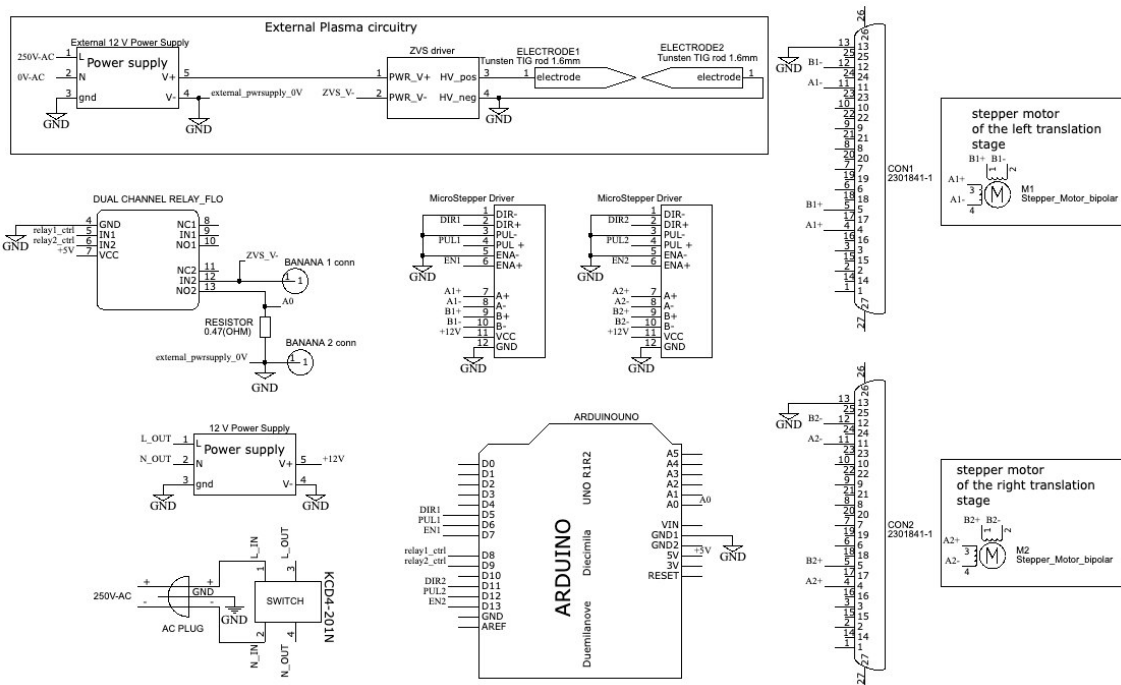
FIGURE A.3: Circuit diagram of motor control and Plasma modules

A.2   Assembly of the motor circuit in the aluminum enclosure

For enclosure, the circuit in the aluminum enclosure is necessary to add and make the holes for the follow elements:

Switch
2 Banana connectors
2 D-sub 15 female connectors
3 pin connector AC 250 V 10 A
Hole for the cable USB B (Arduino PC Connection)
While users have the flexibility to position the components according to their preference, we recommend the following procedure for optimal connector placement.

1.- Position the box horizontally and identify the faces indicated in Figure A.4.
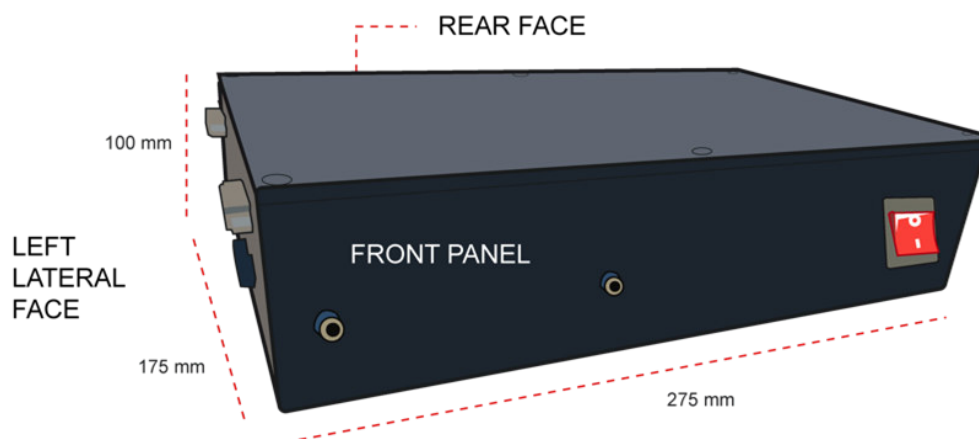
FIGURE A.4: Aluminum enclosure illustration

2.- Located the front panel face and make the hole for the ignition switch, with the measures specified in Figure A.5.
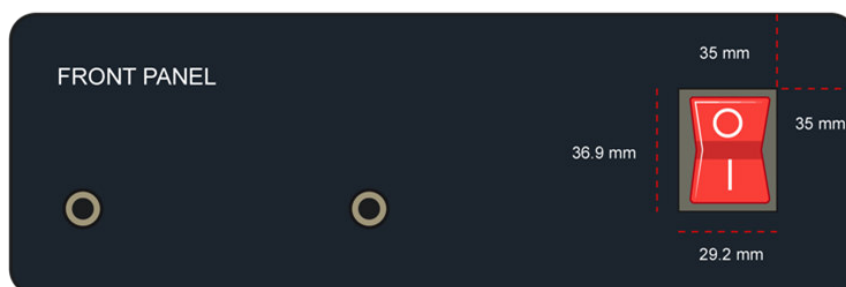
FIGURE A.5: Front Panel face with the dimensions of the hole for the 1) switch

3.- In the lateral left face, make the openings for the installation of two banana
connectors and two D-sub 25 connectors where the dimensions and position of the
holes are specified in Figure A.6.
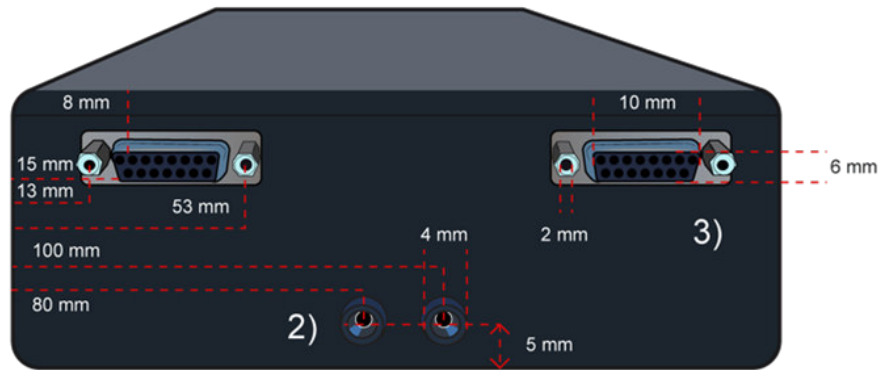
FIGURE A.6: Left Lateral Face with the dimensions of the holes for the 2)
Banana and 3) D-sub 15 connectors

4.- Lastly, create openings for the AC connector and the USB-B Arduino port on
the rear face of the enclosure. (see Figure A.7)

FIGURE A.7: Rear Face with the dimensions of the holes for the 4) AC
connector and 3) USB B (Arduino)

5.- The components of the motor control module must be appropriately positioned
within the aluminum enclosure, following the connections of the adapters mounted
in the enclosure, as depicted in Figure A.8.
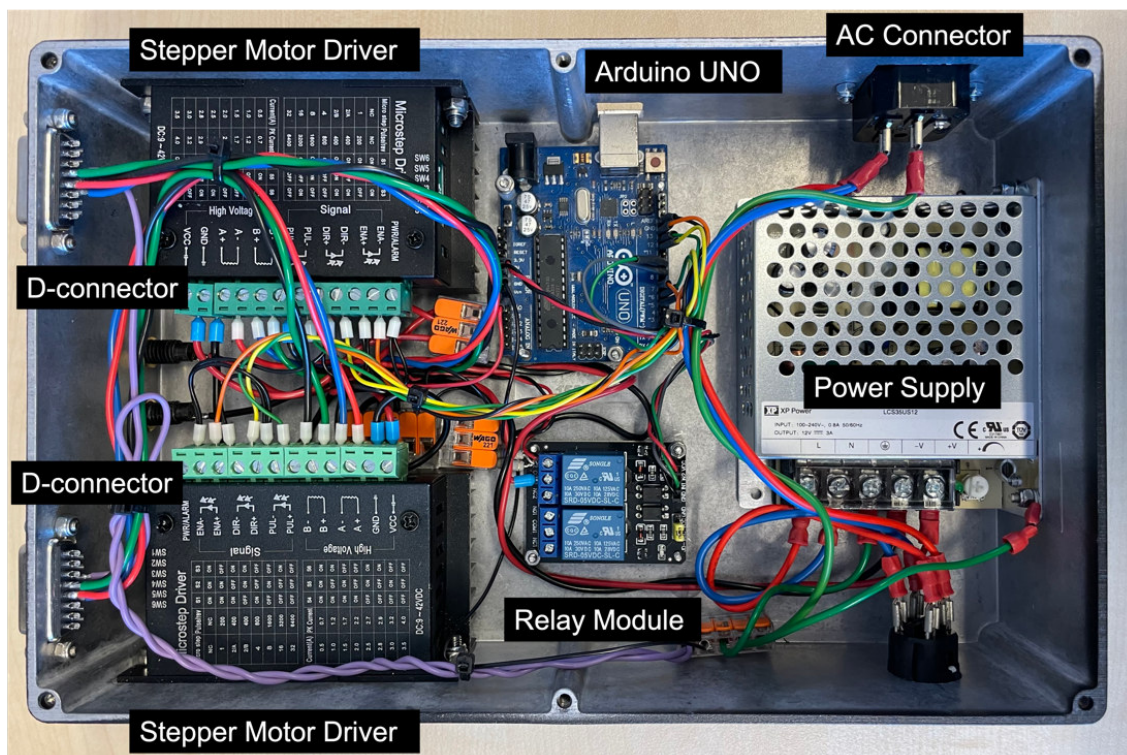
FIGURE A.8: Internal view of the Motors control module

A.3 Construction of plasma ZVS Module

The plastic enclosure is necessary for the hardware of the plasma. Make a hole for the banana female plug corresponding to the 7 V external power supply. The external hardware wiring connections are depicted in Figure A.2, while Figure A.3 shows the circuit diagram of this module. The mounting instructions are describing in the following procedure:

1.- Begin by establishing the connection between the motor control module and the plasma generator by setting the following configuration:

- Connect the positive terminal of the external 7 V power source (+) directly to the input voltage terminal on the ZVS board.

- Take the negative terminal of the external 7 V power source (-) and connect it to N02 on the motor circuit.

- Finally, connect Pin COM2 of the motor circuit to the negative input terminal of the ZVS board.

2.- Connect the blue wires from the coil to the power output of the ZVS controlled module. The orange-tipped paired wires must be connected to the central connector on the board, which corresponds to negative (-), while the other two yellow-tipped wires should be connected to the positive (+) ends of the connector.

3.- Solder the two red ends of the Tesla coil red wires to the tungsten electrodes, where one is the high voltage positive electrode, and the other is ground.

Note that the ground wire must be connected to the ground of the AC mains that power the rig, and the other red wire located in the middle of the coil is not connected (NC).
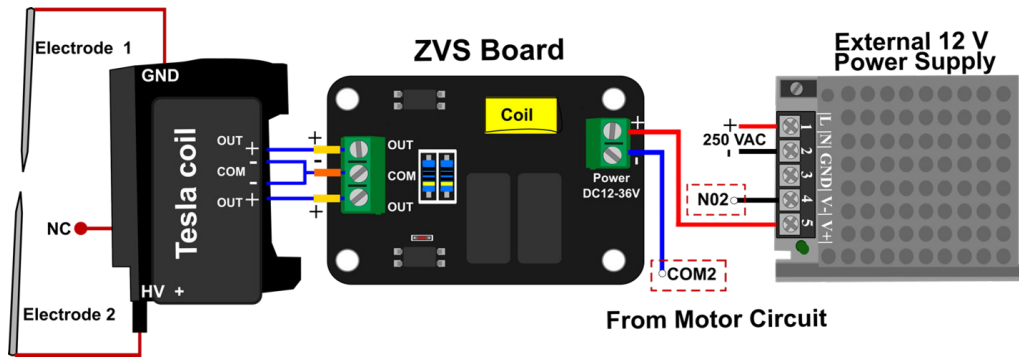

FIGURE A.9: Plasma generator wiring diagram

A.4 Assembly of the plasma circuit in the plastic enclosure

To mount the plasma generator in the plastic box, the elements must be positioned and secured at the bottom of the box. To install the connectors, the following steps must be performed:

1.- Loca the smallest lateral faces, see figure A.9.
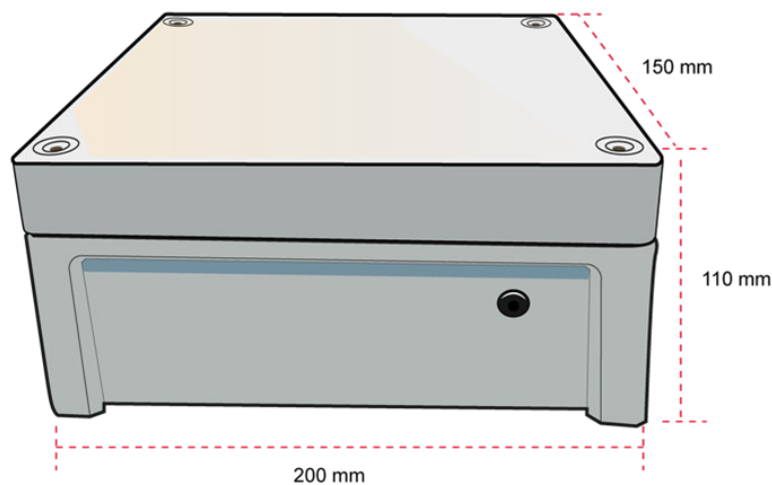
FIGURE A.10: Plastic enclosure

2.- In the left face, make two holes for the two cables corresponding to high voltage and ground of the Tesla coil, the dimensions of the holes are shown in Figure A.10.
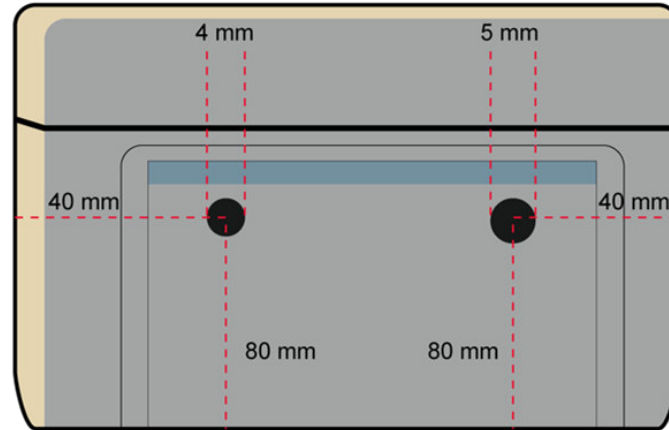

FIGURE A.11: Left Lateral Face with the dimensions of the holes for the HV and GND cables

3.- Make the hole for the DC power adapter of the external power supply in the right face, with the dimensions described in Figure A.11.
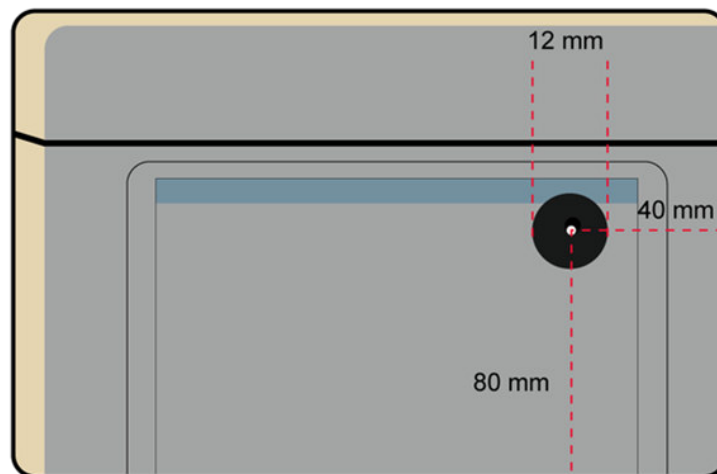

FIGURE A.12: Right Lateral Face with the dimensions of the hole for the DC power adapter

4.- The plasma module is conveniently situated within the plastic enclosure. The High Voltage and Ground cables are connected to the tungsten electrodes, and the female DC power adapter serves as the interface for the external 12 V Power Supply. (see Figure A.12).
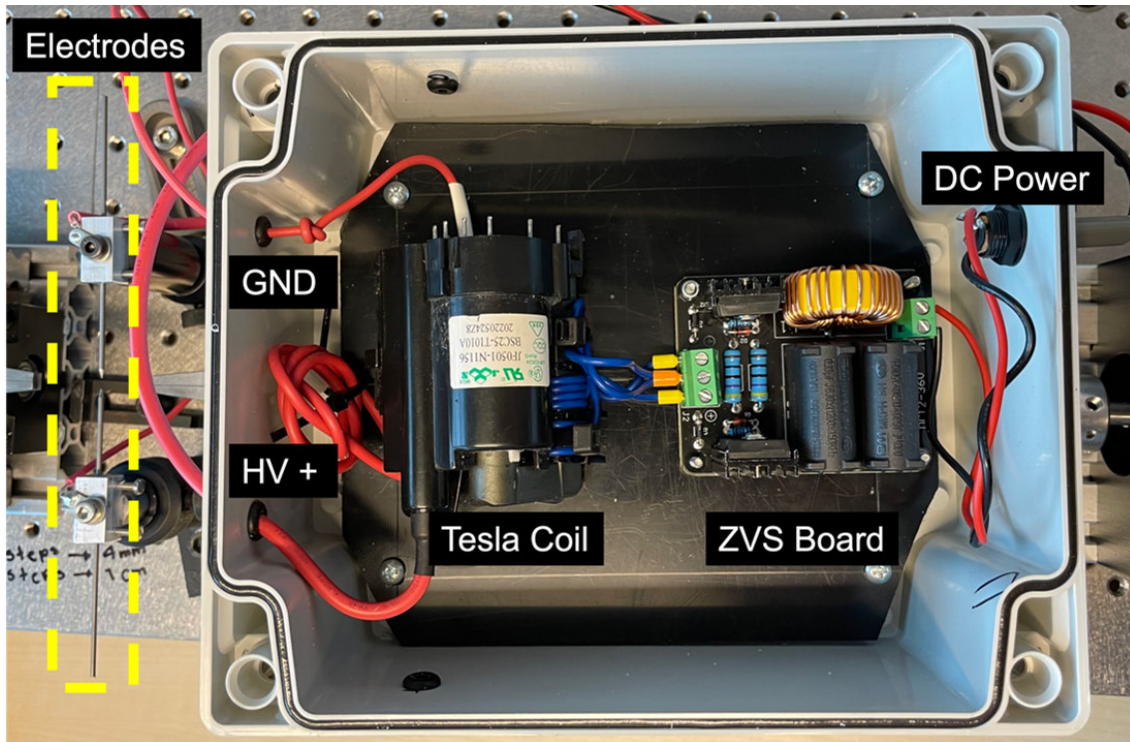
FIGURE A.13: Internal view of the plasma module

A.5 Assembly of the mechanical setup

To construct the mechanical setup, you will require a workspace of 0.3 square meters, which equates to 1000 x 300 x 60 millimeters (length x width x height) on a leveled surface. We recommend using an optical table to mount the experiment, as this will minimize motor-induced vibrations and enhance precision in distance measurements.

For improved clarity regarding the assembly process, please follow these steps:

1.- Place the linear translations stages in a front-to-front orientation, maintaining a 100 mm gap between them.

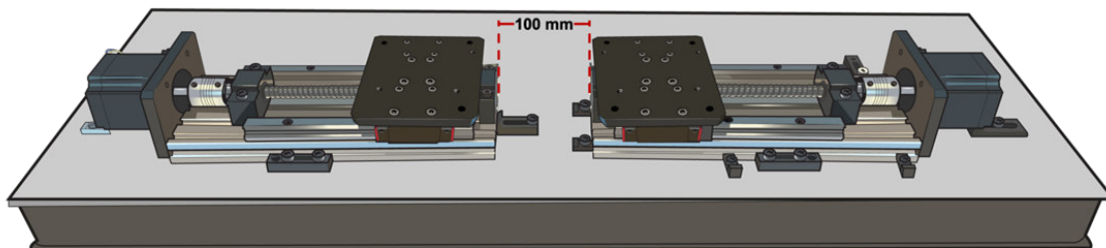

FIGURE A.14: Illustration of linear guide module placement

2.- Position the linear translation stages with precision, ensuring symmetry on the worktable and perfect alignment with each other. Use the edges of the table as your

reference point.

3.- Fix the elements using clamp packs in case of optical table.

4.- Collocate the aluminum base and the v-groove on the plates of the platforms with correct screws according to the diameter of the holes describing in the machined material figures or in the following Figure 17.
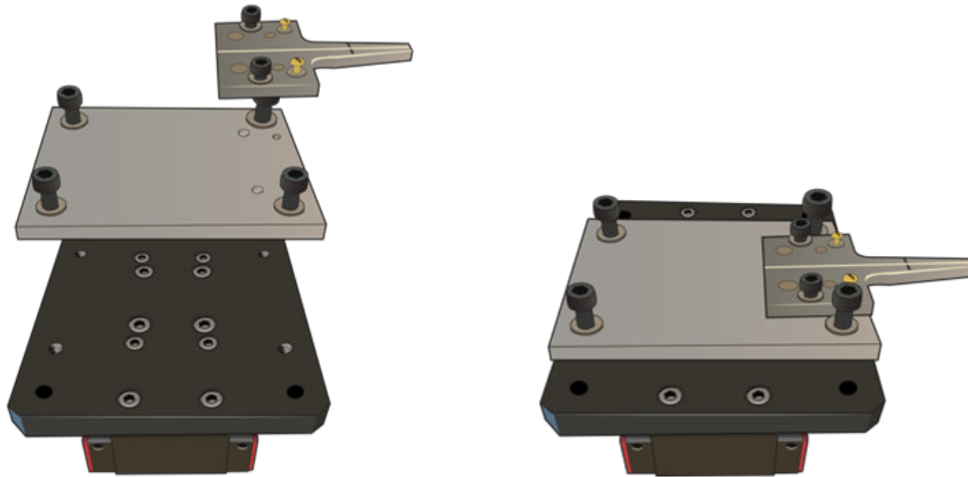

FIGURE A.15: Illustration of base and v-groove assembly

5.- Introduce the tungsten electrodes into their machined holder, securing them in place with the corresponding screws, and mounting the assembly onto an optical post. The HV+ holder should have an isolated post with at least 20 mm thickness with respect to the optical table to avoid arcing. The ground post must be connected to the common ground of the electrical circuit and directly to the optical table.
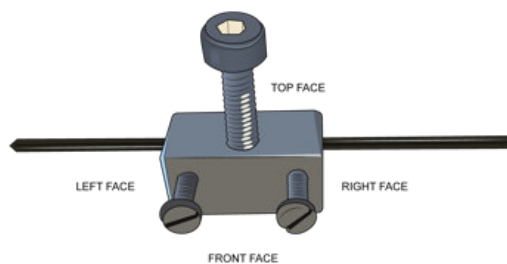

FIGURE A.16: Tungsten electrode placed in machined holder

6.- Place the tungsten electrodes between the translation stages. Ensure that the electrodes are set at the same height in relation to the top of the V-groove. It is advisable to use optical posts for precise control during this step.

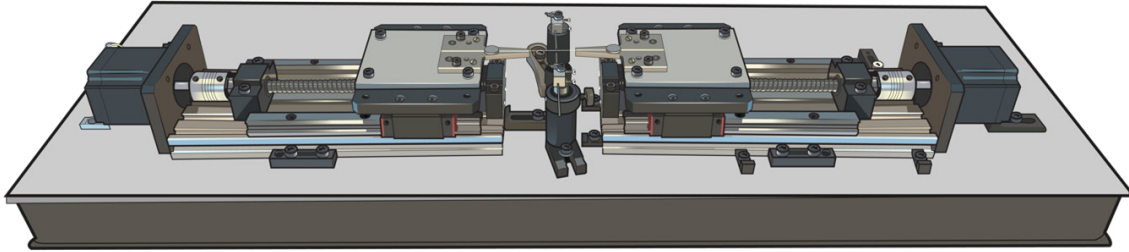7.- Fix the electrodes with 6 mm distance between them.

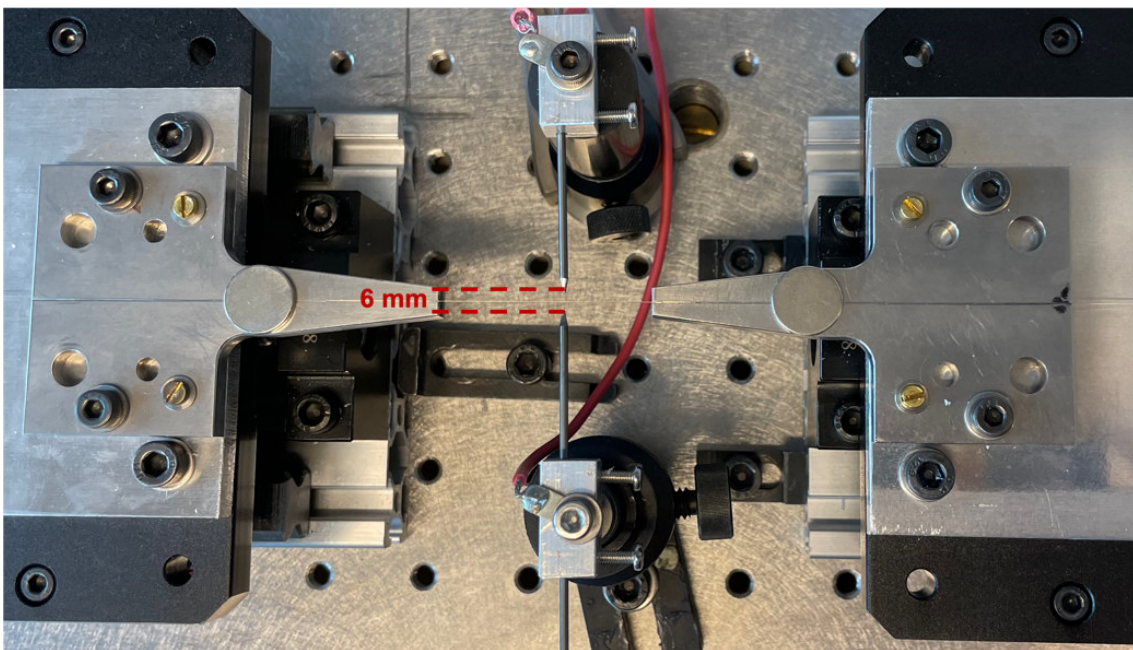FIGURE A.17: Illustration of electrodes placement

FIGURE A.18: Photograph showing the placement of the electrodes between the V-grooves.

8.- To guarantee that the space between the electrodes aligns perfectly with the V-grooves, employ optical fibre for the alignment process.

9.- Finally, establish the electrical connections by connecting the motor cables to the motor control module and the electrodes to the Plasma ZVS Module.